



HAL
open science

Study of Toxicity of Nanoparticles in Biological Media

Sadequa Sultana

► **To cite this version:**

Sadequa Sultana. Study of Toxicity of Nanoparticles in Biological Media. Bioengineering. Université Sorbonne Paris Cité, 2015. English. NNT : 2015USPCD018 . tel-01516920

HAL Id: tel-01516920

<https://theses.hal.science/tel-01516920>

Submitted on 2 May 2017

HAL is a multi-disciplinary open access archive for the deposit and dissemination of scientific research documents, whether they are published or not. The documents may come from teaching and research institutions in France or abroad, or from public or private research centers.

L'archive ouverte pluridisciplinaire **HAL**, est destinée au dépôt et à la diffusion de documents scientifiques de niveau recherche, publiés ou non, émanant des établissements d'enseignement et de recherche français ou étrangers, des laboratoires publics ou privés.

Université Paris 13

N° attribué par la bibliothèque

--	--	--	--	--	--	--	--	--	--

THÈSE

Pour obtenir le grade de

DOCTEUR DE L'UNIVERSITÉ PARIS 13

Discipline: Physique mention Génie Biologique et Médical

École Doctorale Galilée

Présentée et soutenue publiquement par

Sadequa SULTANA

Le 20 Mars 2015

Study of Toxicity of Nanoparticles in Biological Media

Directeurs de thèse: Prof. Marc LAMY de la CHAPELLE et Dr. Milena SALERNO

JURY

Dr. Claire MANGENEY	Université Paris 7	Rapporteur
Prof. Dominique BARCHIESI	Université de Technologie de Troyes	Rapporteur
Prof. Simion ASTILEAN	Babes - Bolyai University	Président
Dr. Nadia DJAKER	Université Paris 13	Encadrant
Dr. Milena SALERNO	Université Paris 13	Co-directrice de thèse
Prof. Marc LAMY de la CHAPELLE	Université Paris 13	Directeur de thèse
Dr. Hanna HLAWATY	Université Paris 13	Examineur invité

Acknowledgement

The completion of this thesis would never have been possible without the support of a great number of people who have cordially given their help and supported me intellectually as well as personally throughout the last three years of my PhD thesis.

Firstly, I would like to thank the Region Ile-de-France in the framework of DIM C'Nano IdF and 'Nanosciences in Ile-de-France' for the financial support without which this work would not have taken place and thanks to Veronique Migonney for allowing me to work at her laboratory CSPBAT.

I would like to thank Professor Dominique Barchiesi and Dr. Claire Mangeney for agreeing to be referees and for their time to review my manuscript. I thank Professor Simion Astilean for chairing my dissertation defense and providing us with time to come to France from Romania to attend my defense.

I am sincerely and heartily grateful to my supervisors Professor Marc Lamy de la Chapelle, Dr. Nadia Djaker, Dr. Hanna Hlawaty and Dr. Milena Salerno for selecting me to be a part of this challenging and exciting project, and for providing me with enormous amount of time, encouragement, technical insight, independence and support in the research. Writing of this thesis would not have been possible without their constant guidance. They are not only very good advisors but also nice colleagues. It was a great pleasure working for and with them.

I am very grateful to my encadrant Dr. Nadia Djaker who supervised me all along my thesis work. I thank her for spending time and having patience to introduce me with the PhD project 'NanoTox' and teaching me every detail starting from handling nanoparticle samples until hands on experimentation of optical set-up. Having no previous experience in optics, I could manage very well with the assembly, alignments and manipulation related to our newly fabricated fluorescence correlation spectroscopy just because of the theoretical and experimental knowledge provided by her. Moreover, I thank her for giving me the chance and opportunity to present my thesis work at national and international conferences held all over France which helped me to keep pace with the external scientific world and made me more motivated at my work.

My sincere thanks to my thesis director Professor Marc Lamy de la Chapelle for his intellectual and knowledgeable advices related to my work. My thesis work was inter-disciplinary and with his keen wisdom in every sector of science he helped me realize my work plan at each step. He was always available for me what made the thesis writing and correction very fast and efficient, and I thank him also for this.

I must thank my another encadrant Dr. Hanna Hlawaty individually for all the supports she provided me during my thesis- both in addressing scientific issues and in solving personal problems. Her innovative ideas related to the *in vitro* toxicity assessments led us to find some exciting results at the biological part. She was never hesitating to discuss my problems whatever it was and gave me inspirations every time I needed it the most. For her patience of listening to me and encouragements to develop positive attitude in my time of distress, I never lost my hope to get good results in my work. My honest gratitude and thanks to her for being not only a supervisor but also a friend of need.

My thesis co-director Dr. Milena Salerno deserves very special thanks because she gave me insights into the hands on expertise in cell culture lab in manipulating cells with hygiene and care. The knowledgeable discussion with her related to the biological assessments clarified the explanation and presentation of my thesis work with better interpretations. I also thank her for being at my side and for giving me freedom while working at her lab.

My thesis work was in collaboration with several other labs, INSERM is one of those labs where I performed the biological *in vitro* toxicity assessments using human endothelial cells. I would like to thank the team members of INSERM, especially Oualid Haddad, Loïc Maillard, and Nicolas Marinval for giving me direct and indirect supports related to the cell culture facilities, and Prof. Nathalie Charnaux who is the director of this platform of INSERM.

Special thanks to another collaborator Professor Simion Astilean's group in NanoBiophotonics Center, University Babeş-Bolyai, Romania for providing gold nanoparticle samples (fabricated by Dr. Sanda Boca-Farcau) that I used in *in vitro* assessments and also for inviting me for one month internship at his group. I also like to thank Dr. Virginie Monnier's group in INL-Lyon for core-shell gold-silica nanoparticles that I used in spectroscopic study.

I thank Nicolas, a doctoral student during my arrival at CSPBAT laboratory, who taught me all the little details of the administrative part at the beginning of my thesis work and thanks to

Maximilien for helping me to manage all the administrative papers for école doctorale during the preparation of my thesis defense. Their generous guidance saved time and facilitated the life. Besides, I thank for being lucky to have intellectual discussions and enormous friendly supports from Inga, Raymond, Zohra, Néné, Xu, Yo, Catherine, Diego and Frédéric Gueinquenaud. I passed three wonderful years with their companies and benefited in both professional and personal lives. Especially the co-operations from Inga and Maximilien to come forward in solving several problems and helping me in personal life are never forgettable because those helps made my professional life going smoothly without any obstacle as a foreign student.

I also thank Nathalie Lidgi-Guigui, Philippe Savarin, Edith Hantz, Nadia Bouchemal and Mohamed Triba for the intellectual remarks during the group scientific presentations and encouragements throughout my thesis work. Their discussion always helped me to think in depth of my experiments.

Last but not the least, I thank my family especially my husband Dr. Hasan-al Mehedi and my parents who supported me throughout this thesis by providing continuous support and guidance in all events.

Table of contents

Introduction	1
Chapter 1. State-of-the art.....	4
1. In-vitro toxicity assessments of nanostructures in biological media	5
1.1 Nanoparticles and nanostructured materials.....	5
1.2 Gold nanoparticles (GNPs) and their biomedical applications	6
1.3 Toxicity of nanoparticles	9
1.4 Detection techniques involved in nanotoxicity studies	17
1.4.1 Quantitative assays	17
1.4.2 Mechanism analysis	17
2. Fluorescence Correlation Spectroscopy (FCS): Theory and state-of-the-art.....	20
2.1 Fluorescence.....	21
2.1.1 Principle of fluorescence	21
2.1.2 Properties of fluorophores	23
2.1.2.1 Quantum yield	23
2.1.2.2 Fluorescence lifetimes.....	23
2.1.2.3 Extinction coefficient	23
2.1.2.4 Photo bleaching and quenching.....	24
2.2 Principle of FCS and theoretical elaboration of correlation functions.....	24
2.2.1 Introduction and theory of Fluorescence Correlation Spectroscopy (FCS) ...	24
2.2.2 Autocorrelation and cross-correlation function: their evolution.....	27
2.2.3 Photophysical aspects of FCS measurements	30
2.2.3.1 Fluorophore concentration	30
2.2.3.2 Molecular weight.....	31
2.2.3.3 Laser excitation power and triplet state.....	33
2.3 Application of FCS.....	33
2.3.1 FCS in biological media.....	34
2.3.2 Metal Enhanced Fluorescence (MEF)	34
2.3.3 MEF applications	36
2.3.4 Characterization of nanoparticles	37
Chapter 2. FCS: set-up and characterization.....	39
3. FCS: Set-up and characterization of the system	40
3.1 Set-up and working principle of FCS.....	41
3.1.1 Description of optical assembly	41

3.1.2 Source of excitation.....	43
3.1.2.1 Installation and alignment of laser	43
3.1.2.2 Installation of power variable attenuators	43
3.1.3 Spectral filters	45
3.1.3.1 Band-pass filter (Excitation filter)	45
3.1.3.2 Dichroic mirror.....	45
3.1.3.3 Emission filter	46
3.1.4 Spatial filters	46
3.1.4.1 Microscope objective	46
3.1.4.2 Beam expander (Telescope)	47
3.1.4.3 Confocal system (Pin hole)	47
3.1.5 Photo detectors and correlator	49
3.2 FCS set-up characterization	50
3.2.1 Measuring the resolution of the FCS set-up by Point spread function (PSF)	50
3.2.2 Characterization of the correlation function.....	53
3.2.3 Photo physical phenomenon during FCS: triplet state evolution.....	57
Chapter 3. Cytotoxicity of gold nanoparticles	60
4. Study of cytotoxicity of gold nanoparticles	61
4.1 K562 cells.....	62
4.2 Materials and Methods	63
4.2.1 Cell culture	63
4.2.2 Cytotoxicity of gold nanoparticles in K562 cells.....	63
4.3 Results and discussion.....	64
4.4 Journal article attached: GNPs toxicity on HUVEC cells.....	66
Chapter 4. FCS Experiments	79
5. Fluorescent nanoparticle characterization by FCS.....	80
5.1 FCS characterization of fluorescent Streptavidin conjugated gold nanoparticles.....	81
5.1.1 Methods and materials	82
5.1.1.1 Reagents	82
5.1.1.2 Synthesis and characterization of gold nanoparticles	82
5.1.1.3 Biotinylation of gold nanoparticles and conjugation of streptavidin-Alexa Fluor 633	83
5.1.2 Results and discussion.....	84
5.1.2.1 Nanoparticles characterization before fluorophore conjugation	84
5.1.2.2 FCS Characterization of binding of fluorescent Streptavidin to Biotinylated GNSs.....	85
5.2 Characterization of fluorescent core-shell gold-silica nanoparticles by FCS	87
5.2.1 Methods and materials	89
5.2.1.1 Reagents	89

5.2.1.2 Synthesis of core-shell gold-silica nanoparticles	89
5.2.1.3 Synthesis of CS1 GNPs.....	90
5.2.1.4 Synthesis of CS2 GNPs.....	90
5.2.1.5 Characterization of fluorescent gold nanoparticles by FCS.....	91
5.2.2 Results and discussion.....	91
5.2.2.1 Nanoparticles characterization before fluorophores conjugation.....	91
5.2.2.2 FCS characterization of Alexa fluor conjugated core-shell gold-silica nanoparticles.....	93
6. Fluorescence diffusion dynamics in the context of GNPs nanotoxicity.....	98
6.1 Mitochondrial fluorophores diffusion and membrane potential in the context of cytotoxicity.....	98
6.2 Study of the mitochondrial diffusion by FCS	100
6.3 Preliminary results in nanotoxicity	102
Conclusion.....	107
Bibliography	110

Introduction

With the advancements in nanoparticle manufacturing and applications, the risk on human and environmental exposure is increasing. It is therefore necessary to study their potential toxic impact on living organisms. While global production of nanomaterials is continually growing, little is known of their effects on health and the environment. With the advent of nanotechnology and the research, production of nanoparticles (NPs) will increase exponentially in the coming years. A global research effort on the regulation of the use of nanoparticles is currently underway, which also addresses concerns about the toxicity of these nanoparticles on the environment, health and safety. The danger is always present in nanoparticles due to the permanent exhibition of the living world to products containing NPs (pesticides, cosmetics, anti-cancer treatment, etc.). It is unclear what happens once the nanoparticles are in the body and for the moment the danger of nanoparticles is not sorted out in detail. Given the emergence of nano-therapeutics and diagnosis as key tools in medicine today, it has become crucial to define precisely the interactions of NPs of therapeutic interests (especially gold nanoparticle, GNPs) with biological systems and characterize the resulting cellular response.

The present thesis based on the platform of “Nanotox” project integrates a collective expertise of several research laboratories who have come together to fulfil the different directions of this multidisciplinary project combining physics, chemistry, and biology and involving several research areas (optics, spectroscopy, chemical surface, cell biology, biotechnology and medicine). To realize such a project, we need to work on physical, chemical and biological issues simultaneously by combining the skills and experience of the project partners in each research area.

This thesis program was funded by a grant from DIM C’Nano Il-de-France. In this project, nanotoxicity in biological systems takes a new direction in research field by developing techniques to detect nanoparticles at very low concentrations and provide the answers needed on their toxicity scale. This project is at the boundary between basic and applied research directly related to the clinical diagnosis of toxicity of nanoparticles and thus beneficial to the public health. In this context, the project “Nanotox” gives real importance to the interaction

between the GNPs and living systems, and allows aiming towards a new direction in the use of these NPs as a function of their nature, size and surface chemistry.

The main objective of the project “Nanotox” was to study toxicity of GNPs in biological media based on their size, shape and surface chemistry (chemical function), which has been developed from the scratch in the framework of this PhD thesis work in the laboratory CSPBAT, University Paris 13. This research work was conducted as part of close collaboration between the laboratories Nanobiophotonics Center, Babes-Bolyai University, Cluj-Napoca, Romania and INSERM U 1148, University Paris 13. Studies have been aimed to conduct *in vitro* studies, both by biological drug screening experiments to study the direct interactions and toxic effect of GNPs in the cellular environment and by spectroscopic studies.

According to the plan and organisation of the work of this thesis work, the beginning was to fabricate and detailed characterization of GNPs (done by our collaborator in Nanobiophotonics Center, Babes-Bolyai University, Cluj-Napoca, Romania), then diagnose the cytotoxicity of the nanoparticles *in vitro* in cellular environment. Cytotoxicity study is performed in detail on human endothelial cell HUVEC starting from viability assay and changes in cell proliferation rate until effects on cell organelles. This part was done by me in the INSERM cell culture platform. To compare the cell proliferation behaviour in presence of the same GNP samples and to compare with the healthy cell HUVEC, a cancer cell K562 was chosen too. By incubating cell-GNPs, the cell proliferation was determined in CSPBAT lab and compared successfully with the healthy cells HUVEC. Further interaction studies have not been performed and kept for the future studies. At the last stage, spectroscopic studies on the cells and nanoparticles were performed in our laboratory CSPBAT.

In this manuscript, I have presented my PhD thesis work along with the result discussion by dividing in four chapters. The Chapter 1 deals with the literature review of the toxicity studies and the state-of-the art of the spectroscopy which is Fluorescence Correlation Spectroscopy or FCS built in the frame work of NanoTox project during this PhD thesis. Further description of this spectroscopy i.e. detailed description of set-up, working principle and system characterization are elaborated in the Chapter 2. Another experimental chapter is the Chapter 3 where I mentioned about the details of the materials and methods of cytotoxicity studies on human cells *in vitro* in presence of six gold nanoparticle samples. This chapter includes

cytotoxicity studies on both healthy HUVEC and cancer K562 cells where HUVEC cell-GNPs interaction is attached as an article already published in the peer-reviewed journal.

The last chapter (chapter 4) describes the experimental details of studies performed by FCS set-up. In parallel to the characterization of the FCS, we decided to perform the characterization of gold nanoparticles which are fabricated in the interest of biomedical applications. Though the objective of this thesis is to study nanoparticle interaction with cellular environment, but as a first step it was important to be able to study the nanoparticle samples themselves by the FCS set-up. Then in the next step the study inside the biological environment would be validated by the comparison of the diffusion properties of the nanoparticles themselves. Thus in the first part of Chapter 4, I described the characterization of two types of GNPs that are fluorescently labelled. The first sample is 20 nm GNPs fabricated in Nanobiophotonics Center, Babes-Bolyai University, Cluj-Napoca, Romania. But these GNPs are further functionalized with fluorophores Alexa 633 by me with the aid of biotin-Streptavidin chemistry. The details of the GNPs fabrication and fluorophores conjugation along with the characterization by FCS is described at the first part of this chapter. Then detailed characterization of another GNP sample of biomedical interest was characterized and described at the later part of the chapter. These second types of GNPs are Alexa Fluor647 doped gold-silica core-shell nanoparticles (CS GNPs) that were fabricated by our collaborator at the Institut des Nanotechnologies de Lyon-INL in Université de Lyon.

The second part of chapter 4 comprises of the utilization of FCS set-up in the study of GNPs in the biological environment focusing mostly on the fluorescence diffusion dynamics in the context of GNPs nanotoxicity. Here we first targeted to see the GNP effect on the most important cellular organelle, mitochondrion that is known as the power house of the cell. As a first step of this study, it was important to characterize the diffusion characteristics of mitochondrion itself using FCS. For performing this, mitochondria were labeled with suitable dye MitoTracker and diffusion behavior of this dye inside mitochondria and on its membrane was revealed by FCS studies. Further studies of mitochondria of the cells incubated with GNPs need to be performed to make a constructive conclusion of this study, though this could not be performed by me due to the limitation of the time frame work of the thesis program. But we have kept it as the perspectives and soon going to be done by new PhD student.

Chapter 1

State-of-the-art

1. In-vitro toxicity assessments of nanostructures in biological media

Summary

- 1.1 Nanoparticles and nanostructured materials
 - 1.2 Gold nanoparticles (GNPs) and their biomedical applications
 - 1.3 Toxicity of nanoparticles
 - 1.4 Detection techniques involved in nanotoxicity studies
 - 1.4.1 Quantitative assays
 - 1.4.2 Mechanism analysis
-

1.1 Nanoparticles and nanostructured materials

Nanoparticles are defined as materials that have at least one dimension between 1-100 nm ($1 \text{ nm} = 10^{-9} \text{ m}$) (ISO definition) and typically exhibit physicochemical properties that is not shared by coarser particles of the same chemical composition¹⁻³. Quantum dots (QDs; such as- CdSe, CdTe), inorganic (carbon nanotube, SiO₂) and metal nanoparticles (gold, silver, iron-oxides) and nano wires, magnetic nanoparticles (ferrites, cobult), organic (polymers-PLA) or lipid nanoparticles (liposomes) and nanostructured thin films (diamond films) are the most promising nanoparticles that are fabricated nowadays for various applications (scheme in the *Figure 1*).

A nanoparticle is the most fundamental component in the fabrication of a nanostructure, and is far smaller than the world of everyday objects, but bigger than an atom or a simple molecule that are governed by quantum mechanics⁴. Nanoparticles are intriguing to scientists because the properties of a metal, such as- gold or silver, in nano form can differ substantially from a larger particle of the same chemical nature and this opens a range of new applications for these particles.

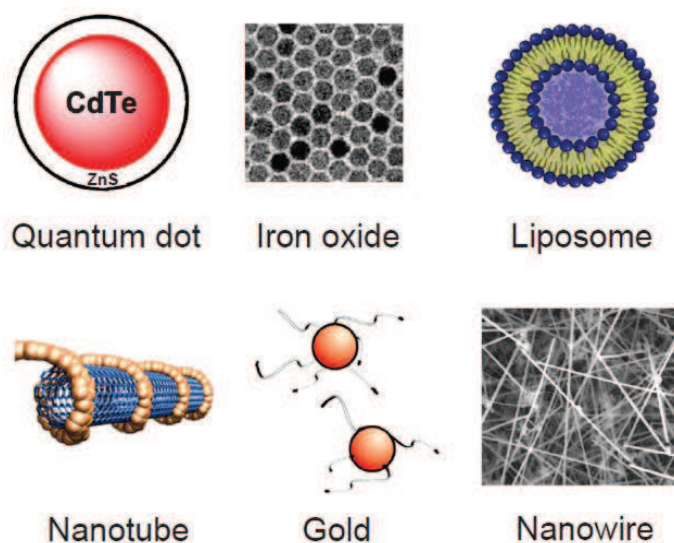


Figure 1. Different nanoparticles and nano-structures of bio-medical interest.

Nano-structured materials are those which have at least one dimension in nanoscale, for example thickness of the material and they may have crystalline structure at the nano range too. Here, we draw example of nano diamond films, which are basically nanoparticles but have nanometer thickness coated on silica wafers. Among all the nanoparticles invented up to now, nanoparticles of biomedical interests are widely engineered by research groups due to their extra-ordinary potential. Nanoparticles have a very large surface-to-volume ratio, which plays a significant role in interaction at the biological interface. Metal nanoparticles, especially gold nanoparticles, are one of those most interesting nanoparticles, which is the core of this thesis work. In this thesis, these particles have been used to study potential toxic effects *in vitro* to determine their less toxic form applicable to biomedicine.

1.2 Gold nanoparticles (GNPs) and their biomedical applications

The era of GNPs begins with the invention of electron microscope followed by the first optimized GNPs fabrication and structural characterization using electron microscope⁵. Then there was no looking back in the development and applications of these nanoparticles. **Figure 2** represents the schematic datation of the evolution of GNPs and its potential application based on time.

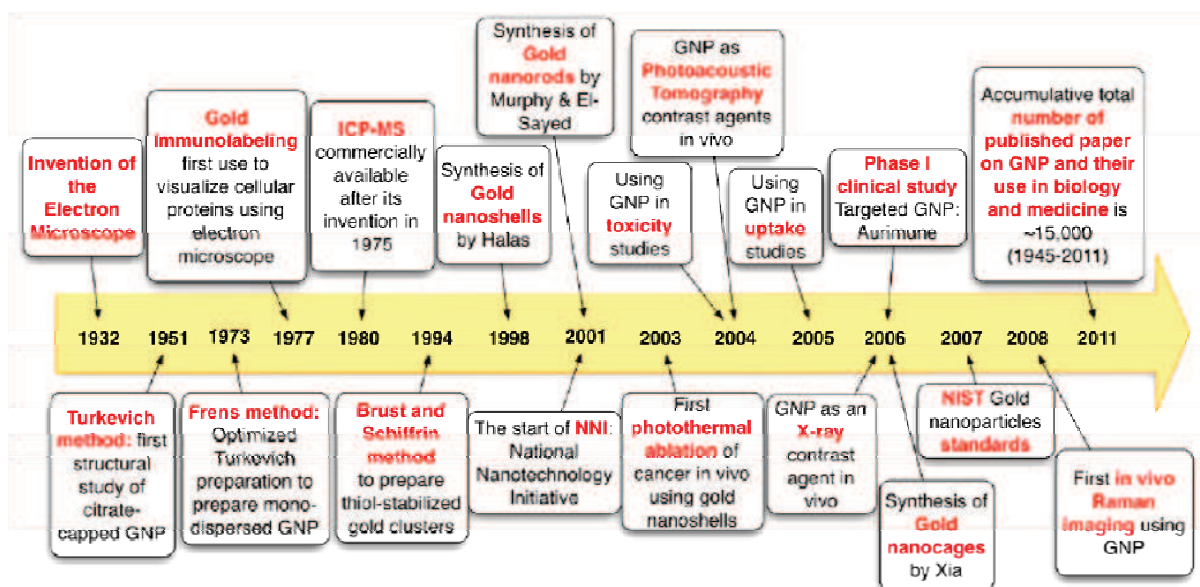


Figure 2. The golden timeline. Evolution of gold nanoparticle fabrication, understanding properties and biomedical applications⁵.

Nanoparticles are typically smaller than several hundred nanometers in size, comparable to large biological molecules such as enzymes, receptors, and antibodies. With the size of about one hundred to ten thousand times smaller than human cells, these nanoparticles can offer unprecedented interactions with biomolecules both on the surface of and inside the cells, which may revolutionize GNP dependent diagnosis, targeted drug delivery and treatment⁶. Moreover, one of the unique optical properties of GNPs is a phenomenon known as Surface Plasmon Resonance (SPR). According to Azzazy and Mansour, when an electromagnetic radiation of a certain wavelength much larger than the diameter of GNPs hit the particles; it induces coherent, resonant oscillations of the metal electrons across the nanoparticles SPR occurred. This SPR will result in a strong optical absorbance and scattering properties of the GNPs⁷.

This unique optical properties lead to their use as localized photothermal agents mediating tumor cell necrosis from hyperthermia after irradiation with laser light^{8, 9}. Besides the application in photothermal therapy, gold nanoparticles (GNPs) are of great interest for several other applications in biomedicine, especially in imaging as contrast agent¹⁰, sensing¹¹ and targeted drug delivery¹² because of their unique physical and chemical properties, and their high biocompatibility. **Figure 3** shows the major domains of biomedical applications of different shapes of GNPs¹³.

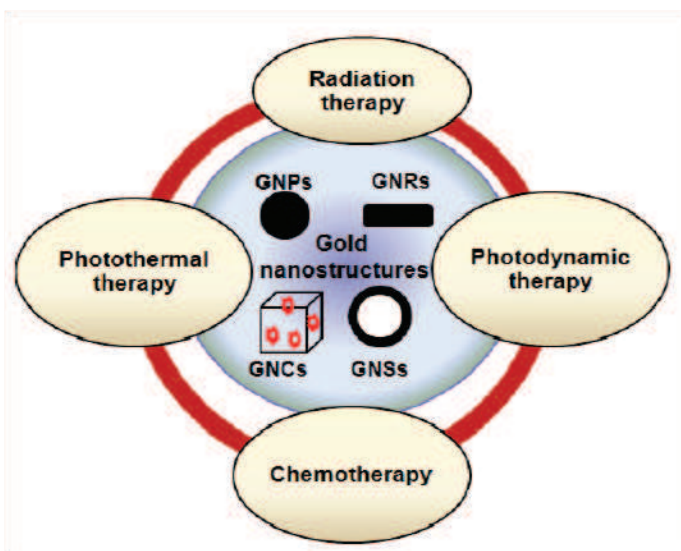


Figure 3. The possibility of combinational therapy for effective therapeutics in cancer treatment. Gold nanostructures are at the center of attention since they can be used as radiation sensitizers, anticancer drug enhancers, heat generators, and also effective drug carriers¹³.

Huang *et al.* provided an *in vitro* demonstration of gold nanorods as novel contrast agents for both molecular imaging and photothermal cancer therapy. Nanorods are synthesized and conjugated to anti-epidermal growth factor receptor (anti-EGFR) monoclonal antibodies and incubated in cell cultures with a nonmalignant epithelial cell line (HaCat) and two malignant oral epithelial cell lines (HOC 313 clone 8 and HSC 3). The anti-EGFR antibody-conjugated nanorods bind specifically to the surface of the malignant type cells with a much higher affinity due to the over expressed EGFR on the cytoplasmic membrane of the malignant cells. As a result of the strongly scattered red light from gold nanorods in dark field, observed using a laboratory microscope, the malignant cells are clearly visualized and diagnosed from the nonmalignant cells, the individual nonmalignant cells are hardly identifiable due to the nonspecific interactions between the nanoparticles and the cells (in **Figure 4**).

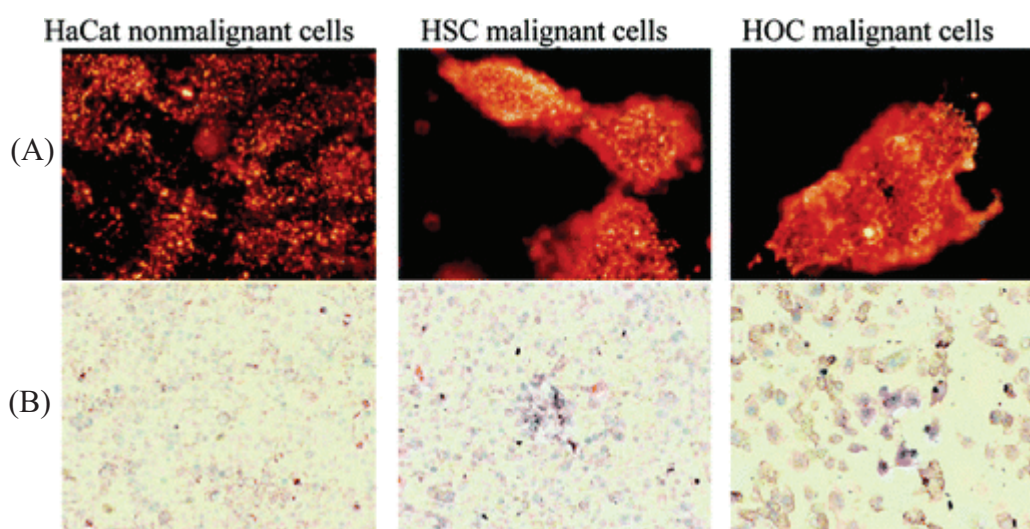


Figure 4. (B) Light scattering images of anti-EGFR/Au nanorods after incubation with cells for 30 min at room temperature. Anti-EGFR/Au nanorod conjugates bind specifically to the

*two types of malignant cells (right two columns) and give them a distinguishable imaging difference from the nonmalignant cells. (B) Selective photothermal therapy of cancer cells with anti-EGFR/Au nanorods incubated with all three cells. At 80 mW (10 W/cm²), the HSC and HOC malignant cells are obviously injured while the HaCat normal cells are not affected*⁸.

It is found that, after exposure to continuous red laser at 800 nm, malignant cells require about half the laser energy to be photothermally destroyed than the nonmalignant cells. Thus, both efficient cancer cell diagnostics and selective photothermal therapy are realized at the same time.

Among different morphologies of GNPs, gold nanospheres (GNSs) are widely used for biomedical applications^{8, 14}. In recent years, gold nano flowers (GNFs) (also termed as urchin like, branched particles or stars) have also become potential candidates as photothermal therapeutics^{15, 16} and cellular imaging agents¹⁷⁻¹⁹; thanks to their tips which are responsible for their very high surface-to-volume ratio²⁰. For all these applications, a better understanding of the interaction and uptake of GNPs into cells is of great importance and currently under intense investigation²¹⁻²³.

1.3 Toxicity of nanoparticles

In order to reap most out of GNPs towards biomedical benefits, safe application is a pre-requisite. This is why; researchers are devoted in safety assessments of GNPs in parallel of the developments and engineering of GNPs, in order to get rid of their toxic effects as much as possible. Here comes the question of nanoparticles toxicity study or toxicology.

Toxicology is the study of potentially harmful effects of substances on living organisms, and nanotoxicology is the study of the adverse effects of engineered nanomaterials on living organisms and the ecosystems, including the prevention and amelioration of such adverse effects²⁴. Nanotoxicology focuses upon gaining a thorough understanding of the relationship between the toxicity of NPs depending on their dose levels and physicochemical properties such as size, shape, reactivity and material composition. In toxicology, a very precise and most important field of study is cytotoxicity study.

Cytotoxicity is, however, a term whose biomedical implication depends on the context. It is essential to carefully distinguish between agents causing universal cytotoxic behavior and agents causing toxicity to specific cells. Nanoparticles are in the size range of 1-100 nm. At this scale, the much larger particle surface-to-volume ratio plays a significant role in

interaction at the biological interface. Due to the 'non-bulk' properties of nanoparticles, including their atypical surface structure and surface reactivity, processes such as dissolution, redox reactions or the generation of reactive oxygen species may be enhanced. Such properties may elicit biological responses that would not be produced by larger particles of the same chemical composition.

Two decades of nanotoxicology research has shown that the interactions between nanomaterials and biological media are remarkably complex. Thus in the past decade, the number of published papers in the field of nanotoxicology has grown by nearly 600% and most of these papers report *in vitro* studies (**Figure 5**)⁶.

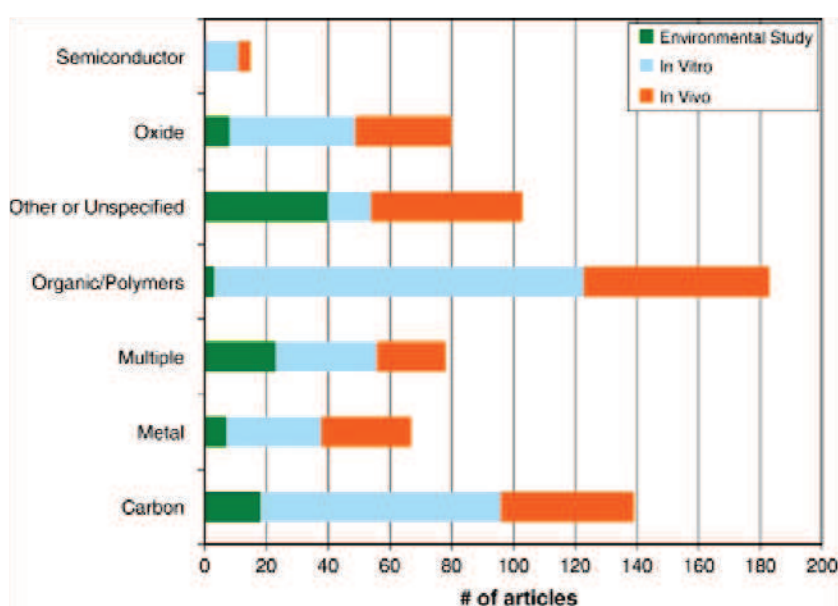


Figure 5. Number of articles relating to material and type of study⁶.

Several groups have examined the cellular uptake and cellular toxicity (cytotoxicity) of metal nanoparticles especially gold nanoparticles from different point of view and varying different parameters. In order to make a correlation between results from different groups' analysis, we should know the parameters for nanoparticles' cytotoxicity assays which are:

1. The concentration of nanoparticles in the solution
2. The size of the particles
3. The number of dosage of particles
4. The duration of each dose
5. The surface chemistry of the nanoparticles
6. The cell line
7. The cell proliferation

8. The mortality fraction

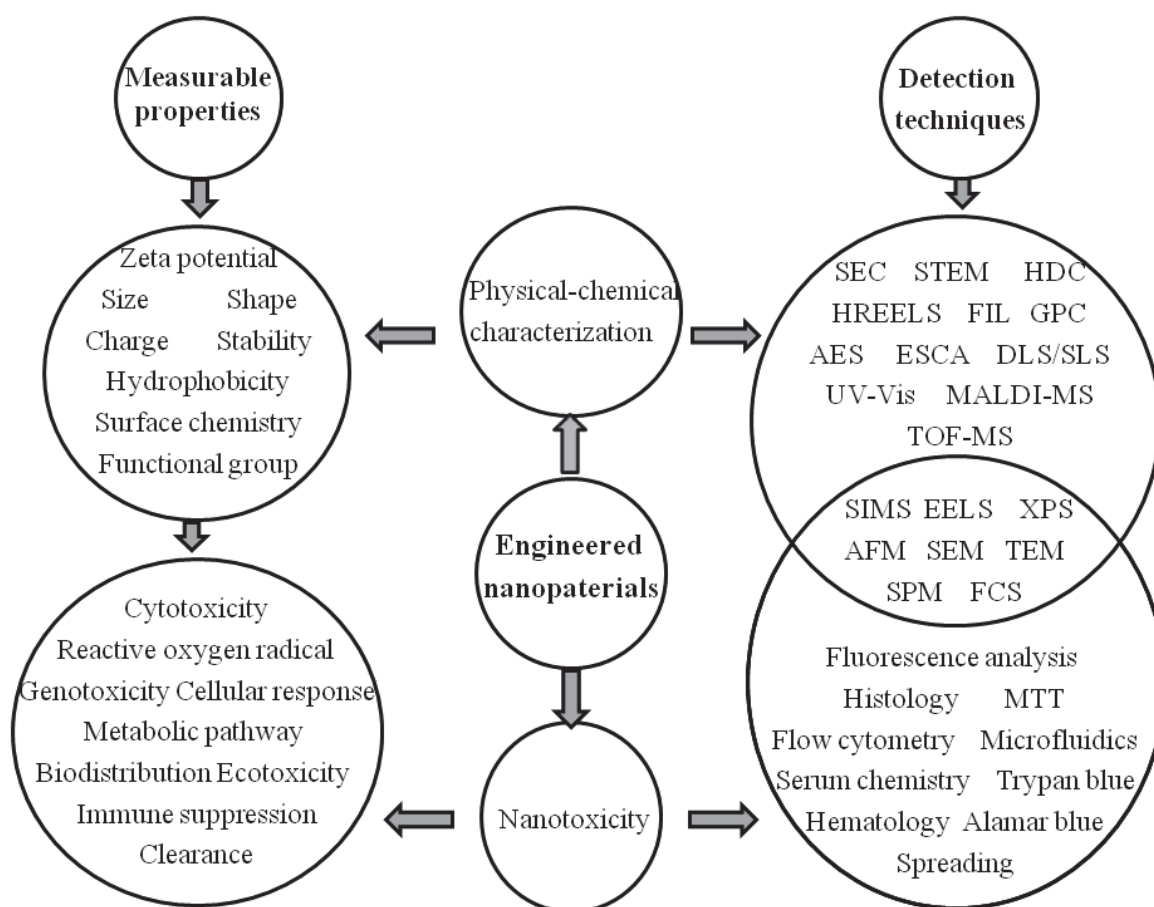


Figure 6. Major techniques and parameters employed for the characterization of engineered nanomaterials and for assessing nanotoxicity (reproduced from ²⁵).

In **Figure 6**, a scheme has been presented summarizing all the parameters/properties and detection techniques for the two different aspects of engineered nanoparticles- (1) physico-chemical characterization and (2) nanotoxicity. The most common form that biocompatibility studies take is the assessment of toxicity of gold nanoparticles *in vitro*- meaning in cell culture, adopting assays similar to those used in drug development screening and cell viability assay, is the very premier one among all. Viability assay demonstrates the overall dose-dependent toxicity of nanoparticles on cultured cells, looking for cell survival and percentage of proliferation compared to control after nanoparticle exposure.

Several groups have identified the size of GNPs as the first variable in their interaction with cells ²⁶⁻²⁸. Chithrani *et al.* reported the effect of GNP size on the cellular uptake with sizes varying between 14 and 100 nm ²⁹. It was shown that the maximum uptake by a cell occurred for 50 nm nanoparticles. GNPs inside cells were trapped in vesicles in the cytoplasm and did

not enter in the nucleus^{26, 29}. Pan *et al.* suggested that the uptake of GNPs is mediated by nonspecific adsorption of proteins onto the gold surface, which induces internalization into cells via the endocytosis mechanism^{27, 28}.

Many reported works showed that GNP size can affect cell adhesion and proliferation: Cui *et al.* showed that small GNSs (2 nm), which are more stable against aggregation, caused less HeLa cytotoxicity than larger GNSs (25 nm) which are liable to form aggregates³⁰. On the contrary, Arvizo *et al.* studied the effect of GNP size on inhibition of endothelial and fibroblast cell proliferation. It was demonstrated that 20 nm GNSs showed a maximal inhibition of cell proliferation up to 100% whereas 10 nm showed up to 60% and 5 nm up to 25% of inhibition³¹. In the same way, Pernodet *et al.* reported that 14 nm GNSs had a significant uptake into dermal fibroblasts³². It was suggested that the presence of GNPs is responsible for abnormal actin filaments and extracellular matrix constructs in dermal fibroblasts, which decrease cell proliferation, adhesion, and motility. Jiang *et al.* proposed that GNPs can not only passively interact with cells, but also at a specific size actively alter the molecular processes that are essential for regulating the cell functions³³. GNPs of 40 to 50 nm are found to be the optimal size for particle uptake is probably due to the direct balance between multivalent cross linking of membrane receptors and the process of membrane wrapping involved in receptor-mediated endocytosis.

Nanoparticle size is not the only important parameter in the GNP-cell interaction. The cell membrane seems to be also very sensitive to the GNP's surface chemistry. By considering only the surface chemistry, Goodman *et al.* found that cationic particles are moderately toxic, whereas anionic particles are quite nontoxic^{26, 34}. Freese *et al.* have discussed different polymer coatings and concluded that the positive-charged coated GNPs were internalized to a greater extent than the negative- or neutral-charged GNPs, as would be expected due to interactions with the anionic cell membrane³⁵. Arnida *et al.* showed that GNPs appeared to be taken up by non-specific adsorptive endocytosis³⁶. PEGylation (PEG=poly ethylene glycol) or protein adsorption on the surface of GNPs drastically reduced this uptake. The most reported chemistry that greatly reduced toxicity was the addition of PEG on the surface of GNPs (PEG-GNPs)³⁷.

The surface chemistry parameter is frequently addressed with GNP shape since the number of surface molecules depends on the GNP shape. Hence, the combined effect of these parameters on GNP-cell interaction was widely discussed. Hutter *et al.* compared different

shapes of GNPs with the same surface chemistry and size range³⁸. They showed that GNSs were significantly more toxic to microglial cells than GNFs. CTAB-coated spheres were readily internalized; whereas, PEGylated spheres did not internalize into microglial cells up to 12 h of incubation. However, the internalization of GNFs occurred independently of the surface coating; GNFs were internalized by microglial cells within the same time period of other nanoparticles (12 h). Sironi *et al.* showed that the PEGylation of the GNFs hinders their internalization and increases their resistance to aggregation in the culture medium³⁹.

Cell line can be an important parameter too as same nanoparticle has been found to show cytotoxicity on different cell lines at different extents. Patra *et al.* did cell selective in vitro study and showed that GNPs (33 nm spheres of CTAB and citrate-capping) do not universally target all cell types. They reported that GNP-induced death response in human carcinoma lung cell line A549 after 36 hrs incubation. In contrast, the two other cell lines tested, BHK21 (baby hamster kidney) and HepG2 (human hepatocellular liver carcinoma), remained unaffected up to 72 hrs of GNP treatment⁴⁰. On the other side, some researchers have found Cancer cells are more resistant than normal cells to GNP exposure⁴¹.

Before shedding light on the cellular interaction with GNPs, it is very important to analyze different other parameters of GNPs besides size, shape and surface chemistry, such as GNP concentration and cell culture properties (cell line, incubation time) and make a combination of all. Recently, Soenen *et al.* proposed a detailed and a multiparametric approach to assess the cell and GNP interactions⁴². Their results highlighted the importance of the multiparametric study to cover all the possibilities of cell-GNP interactions and to screen multiple ways of interaction using standard toxicity assays. Considering GNP concentration, it was reported that GNSs at 10 nanomolar concentration showed more cytotoxicity than GNFs, which were relatively innocuous³⁸, whereas significant toxicity of GNFs was observed in epithelial cells under a picomolar (pM) concentration¹⁹.

Gold nanoparticles' physiological condition in the cell culture media is very important as it may influence the nanoparticle internalization inside cells and thus affect the toxic behavior upon cells. Cui *et al.* showed the effect of aggregated nanoparticles on HeLa cells (**Figure 7**), where small GNPs can be endocytosed by cells and form aggregates inside the cell, resulting in cytotoxicity. When the aggregates become too large to enter the cell and instead adhere onto the cell surface, the growth rate of HeLa cells increases. On the other hand, mono-dispersed particles were easily endocytosed causing cytotoxicity. Thus we can conclude that

aggregated nanoparticles may either remain non-toxic to cells or trigger cell proliferation rate which in the long run can be harmful causing tumorous tissue with uncontrolled cell division.

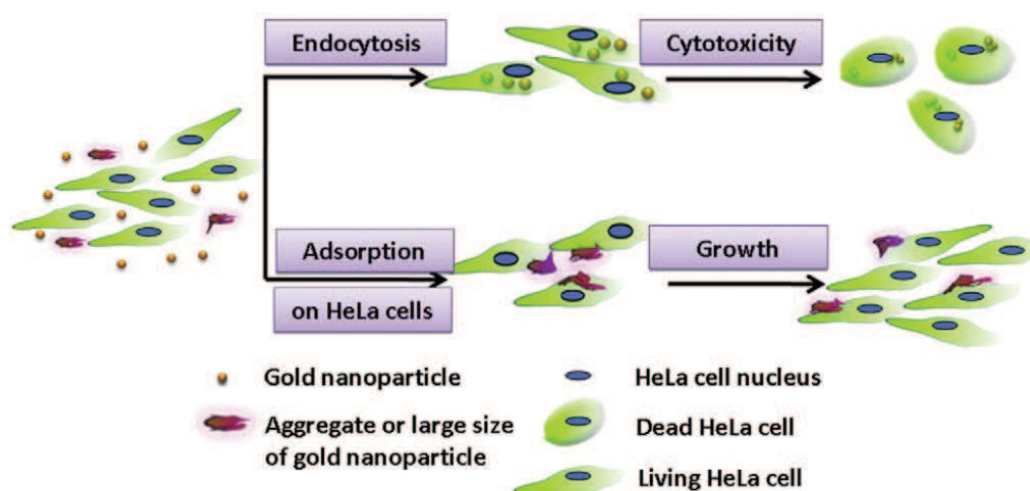


Figure 7. Schematic drawing representing the mechanism of cytotoxicity and growth of HeLa cells co-cultured with GNP-PVPs and their aggregates ⁴³.

A question still remains, what exactly happens inside cells due to the cell-nanoparticles interaction. **Figure 8** shows possible potential cell-nanoparticles interactions and interferences after internalization inside cells. According to Sanvicens and Marco, the damage due to nanoparticles on cells start from the very beginning of nanoparticle-cell interaction by the damage of plasma membrane upon internalization of toxic dose of nanoparticles. Following that, they can interact with the highly negatively charged DNA in the nucleus and may prevent transcription or DNA replication. Also, nanoparticles are able to target mitochondria directly, which can lead to mitochondrial disruption and, in turn, to ROS production. Oxidative stress owing to excess ROS generation induces over-expression of antioxidant enzymes in an attempt to control ROS levels. At high levels of oxidative stress, antioxidant defenses are overwhelmed, which leads to inflammatory and cytotoxic responses. Oxidative stress might induce collateral damage, such as lipid peroxidation, protein denaturation, nuclear and DNA damage and immune reactivity. Thus the fate of the cells is either inflammation or mitochondrial damage induced apoptosis ⁴⁴.

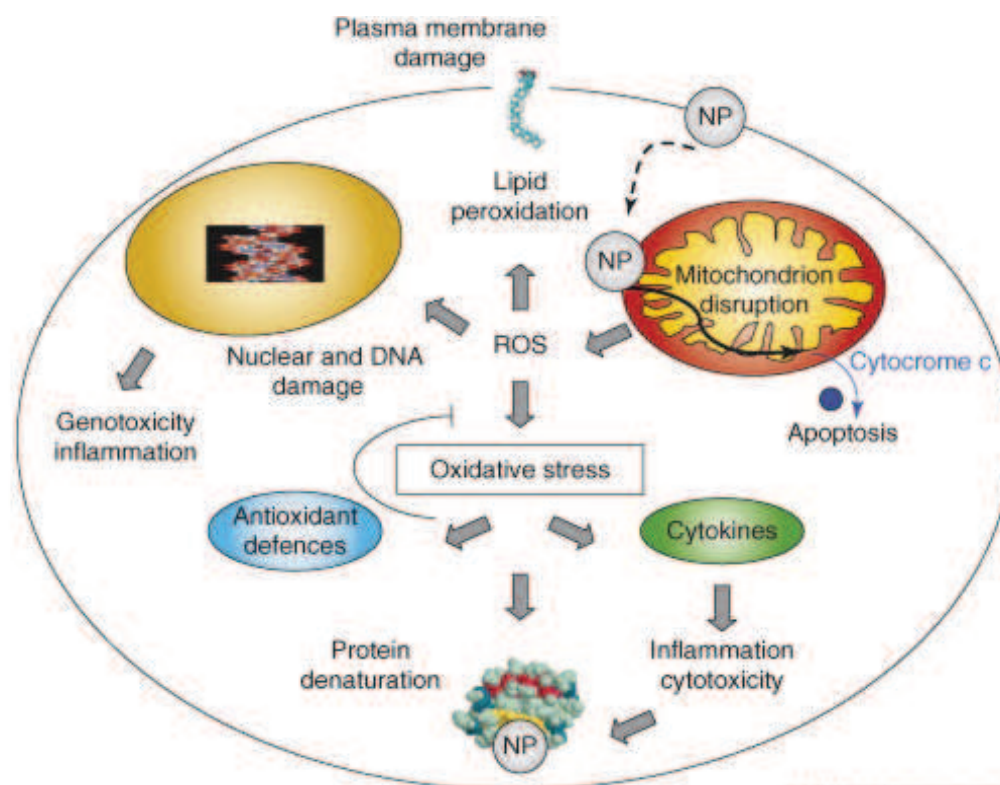


Figure 8. Schematic of potential cell-nanoparticles interactions and interferences after internalization inside cells (NP= nanoparticles, ROS= reactive oxygen species)^{44, 45}.

Different groups have explained nanoparticles toxicity induced apoptotic cell death with possible mechanism and signaling pathways. The most appreciated mechanism involves the engagements of apoptic protein families- Bcl-2, Bax and caspase. Choi *et al.* elaborates apoptotic cell death pathways induced to toxicants, such as-GNPs. They have stated that the apoptosis pathway is divided into two phases-extrinsic and intrinsic pathways. GNPs induced an increase in the mRNA expression of bax and bak, which are pro-apoptotic members of the Bcl-2 family and which are responsible for the induction of intrinsic mitochondria apoptosis⁴⁶. GNPs also induced the caspase-8 expression, which is associated with an extrinsic apoptotic pathway. GNPs provoked the expression of caspase-3, which is a common downstream effector of both extrinsic and intrinsic apoptosis pathways. Based on our caspase-8 expression data, GNPs also evoked an extrinsic apoptotic pathway in addition to an intrinsic pathway. Therefore, the apoptosis induced by GNPs is mediated by both intrinsic and extrinsic pathways as illustrated in **Figure 9**⁴⁷.

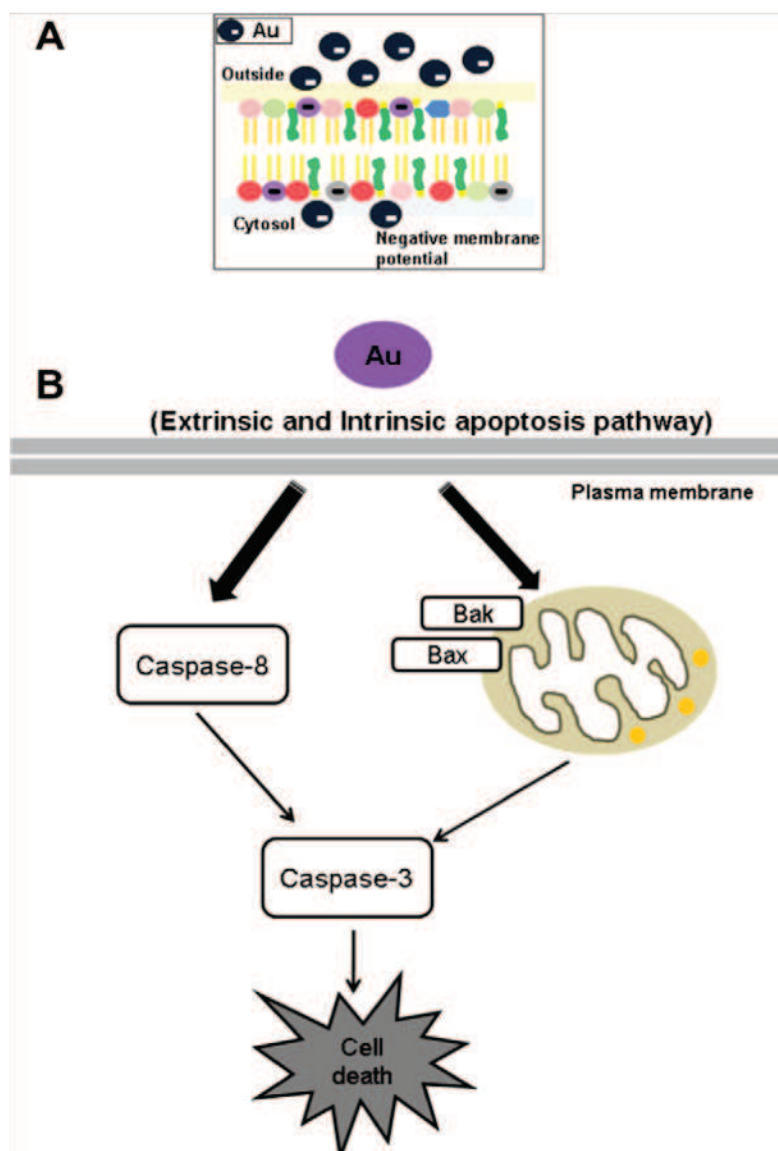


Figure 9. (A) Cell membrane and cellular uptake of AuNPs (gold nanoparticles). (B) Schemes of cell death induced by AuNPs. AuNPs provoke intrinsic apoptotic pathway and extrinsic apoptotic pathway through caspase-8 activation⁴⁷.

Many more variables require further testing, including shapes other than spheres, and different functional groups on the surfaces of the nanoparticles. It will be important to determine whether nanoparticles are themselves modified by the cellular environment, thus potentially altering the properties of the nanoparticles for biosensing, imaging, or delivery applications²⁶.

1.4 Detection techniques involved in nanotoxicity studies

1.4.1 Quantitative assays

The quantitative cytotoxicity assays are utilized to get result in a quantitative manner for example to count viable cells or dead cells due to NPs incubations (in *Figure 10*). For example, LDH (Lactate DeHydrogenase) Assay is a colorimetric assay measuring the release of lactate dehydrogenase (LDH) into the culture media as an indicator of cellular membrane disruption. But here we cannot have number of proliferated cells in the culture media. On the other hand, MTT Assay is another colorimetric assay that measures the enzymatic activity of cellular mitochondria. If cells properly metabolize the MTT dye, the cell culture will turn blue, allowing for simple absorbance measurements to be used to quantify cellular activity. This metabolic assay considered as the “gold standard” for cytotoxicity. It can measure the exact amount of viable cells. Trypan Blue Exclusion Method enables to accurately determine the cell viability by investigating plasma membrane disruption. If cells take up trypan blue, they are considered as non-viable. Cell viability is calculated as the number of viable cells divided by the total number of cells. ROS (reactive oxygen species) Assay monitors the oxidative stress by measuring the level of ROS. By using Atomic absorption spectroscopy, we can determine the amount of NPs internalized in the cell culture samples. But it gives no idea about the proliferating or dead cell number. RT-PCR and DNA micro-array is a real-time polymerase chain reaction amplification and DNA micro-array analysis to examine the expression levels of genes that are, for example, related to stress in the cell. It can determine the toxicity extent at the molecular level, such as toxic protein amount expressed during each exposure with NPs.

1.4.2 Mechanism analysis

When we need to study the mechanism of NPs internalization inside cells or any interaction mechanism, we need several other high throughput methods (in *Figure 10*). For example: Transmission electron microscopy (TEM). This microscopic technique is performed to qualitatively measure cellular uptake, gold nanoparticles can be visualized in microtome-cell slices after exposure by TEM, which takes advantage of the high electron density of gold nanoparticles. Sometimes the researchers consider this technique as a semi-quantitative method. Dark field optical microscopy can be performed on living cells to visualize the location of gold nanoparticles (within the diffraction limits of the instrument, typically ~200

nm) which takes advantage of the elastic light scattering properties of the gold nanoparticles from the plasmon bands. This one is also a semi-quantitative technique. Fluorescence microscopy can be used with living cells, if fluorescent dyes are conjugated to the nanoparticles and certain cell organelles of interest are labeled too. Thus we can observe both NPs aggregate internalization as well as any stress induced modifications on the cellular organelles. ICP-MS (Inductively coupled plasma mass spectrometry) is considered as a tool that has high specificity and low limits of detection. It can be applied to quantify then cellular uptake by digesting the cells with strong acid. But it is a destructive technique, and cannot differentiate between nanoparticles adsorbed to the surface of the cell and internalized into cells. Treatment of cells with heparin sulfate before analyzing the cells can be used to desorb surface adsorbed nanoparticles, assuming that heparin sulfate polymer has a higher binding affinity to the cellular surface to displace surface-bound gold nanoparticles. On the other hand, ICP-MS with I₂/KI etching is other type of ICP-MS analysis that is combined with I₂/KI etching was used to quantify the number of gold nanoparticles both “on” and “in” the cells. The idea is to selectively etch the gold nanoparticles on the surface of the cells using solutions of I₂ and KI.

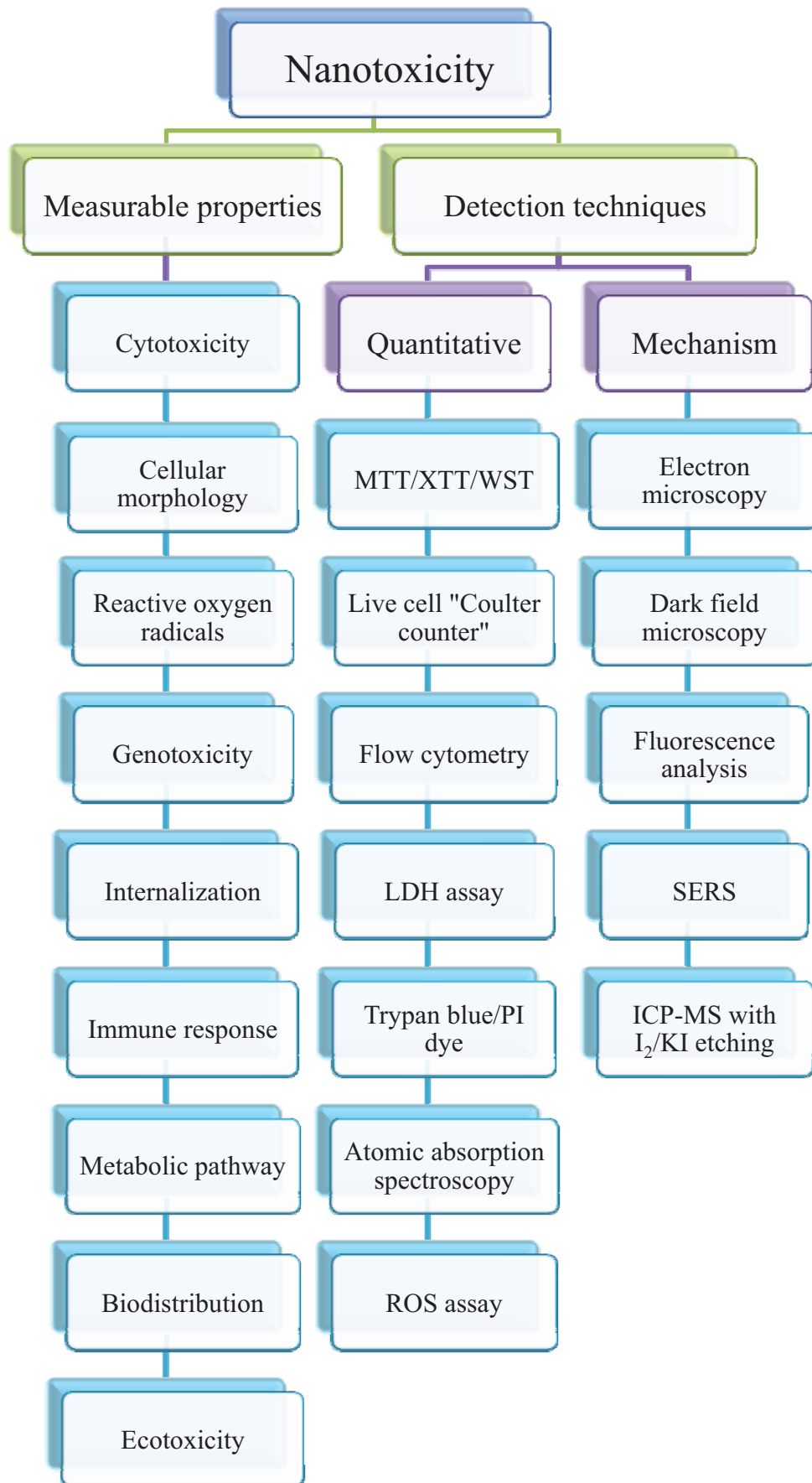


Figure 10. Diagram of parameters and detection techniques involved in nanotoxicity studies.

2. Fluorescence Correlation Spectroscopy (FCS): Theory and state-of-the-art

Summary

2.1 Fluorescence

2.1.1 Principle of fluorescence

2.1.2 Properties of fluorophores

2.1.2.1 Quantum yield

2.1.2.2 Fluorescence lifetimes

2.1.2.3 Extinction coefficient

2.1.2.4 Photo bleaching and quenching

2.2 Principle of FCS and theoretical elaboration of correlation functions

2.2.1 Introduction and theory of Fluorescence Correlation Spectroscopy (FCS)

2.2.2 Autocorrelation and cross-correlation function: their evolution

2.2.3 Photophysical aspects of FCS measurements: effects of physical parameters

2.2.3.1 Fluorophore concentration

2.2.3.2 Molecular weight

2.2.3.3 Laser excitation power and triplet state

2.3 Application of FCS

2.3.1 FCS in biological media

2.3.2 Metal Enhanced Fluorescence (MEF)

2.3.3 MEF applications

2.3.4 Characterization of nanoparticles

In this chapter, a detailed explanation of theoretical aspects and state-of-the-art of Fluorescence Correlation Spectroscopy (FCS) are described. Beyond being an important technique in the arsenal of modern biophysics, biochemistry, and cell biology; FCS represents a significant example of how the microscope can be used to extract better information within the resolution limit of classical optics. The diffusion times, or the interaction of macromolecules, the absolute concentration of fluorescently labelled particles, and the kinetics of chemical reactions are studied by FCS. So one can extract both qualitative (presence or absence of interaction) and quantitative (diffusion times, stoichiometry of interactions, concentration of interacting particles, and kinetics of this interaction) information about the macromolecules being studied⁴⁸.

Before entering into details about FCS theory, a theoretical description of fluorescence, its principles and properties are explained in section 2.1. Then principle and theoretical elaboration of FCS is described in section 2.2 in detail. In this section, the photo physical phenomena during FCS analysis are also explained for understanding of the next chapters with FCS study and results. At the end in section 2.3, applications of this technique are mentioned as state-of-the-art.

2.1 Fluorescence

2.1.1 Principle of fluorescence

Luminescence is the emission of light from any substance, and occurs from electronically excited states. Luminescence is formally divided into two categories—fluorescence and phosphorescence depending on the nature of the excited state. In excited singlet states, the electron in the excited orbital is paired (by opposite spin) to the second electron in the ground-state orbital. Consequently, return to the ground state is spin allowed and occurs rapidly by emission of a photon⁴⁹.

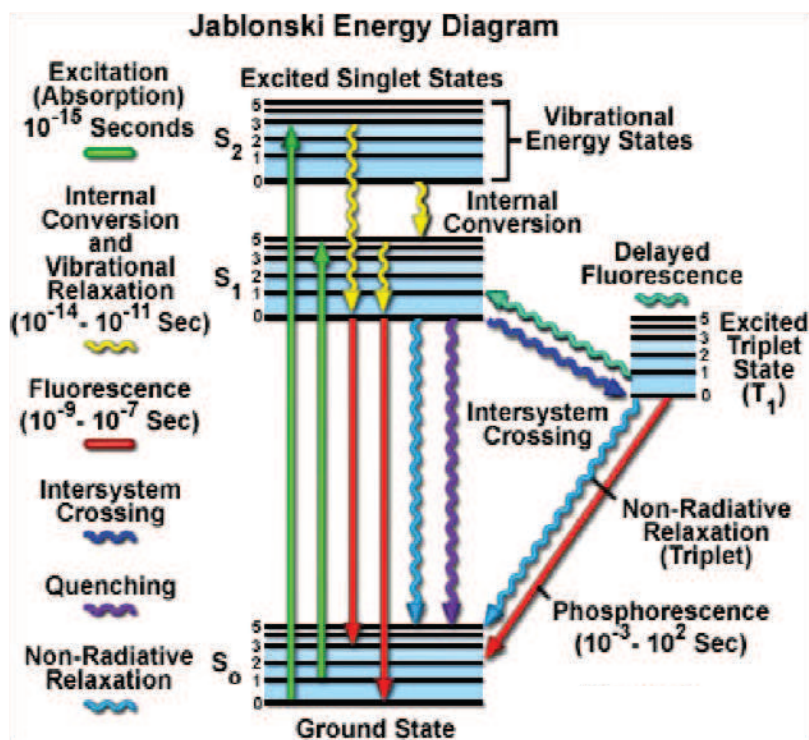


Figure 11. Jablonski diagram used to explain energy states and phenomenon of fluorescence (www.olympusmicro.com/primer/java/jablonski/jabintr0/).

In **Figure 11**, there is a Jablonski diagram showing the ground energy state (S_0), as well as the first (S_1) and second (S_2) excited singlet energy states. At each of these electronic energy levels the fluorophores can exist in a number of vibrational energy levels; depicted by 0, 1, 2, etc. The transitions between states are depicted as vertical lines to illustrate the instantaneous nature of light absorption. Following light absorption (illustrated by the green arrow), several processes usually occur. A fluorophore is usually excited to some higher vibrational level of either S_1 or S_2 . Return to the ground state typically occurs to a higher excited vibrational ground state level, and induces the emission of fluorescence (illustrated by the red arrow). Molecules in the S_1 state can also undergo a spin conversion to the first triplet state T_1 . Emission from T_1 is termed as phosphorescence, and is generally shifted to longer wavelengths (lower energy) relative to the fluorescence. The excited state energy can be dissipated non-radiatively as heat (illustrated by the cyan wavy arrow), the excited fluorophore can collide with another molecule to transfer energy in a second type of non-radiative process (for example, quenching, as indicated by the purple wavy arrow), or a phenomenon known as intersystem crossing to the lowest excited triplet state can occur (indicated by the blue wavy arrow). Conversion of S_1 to T_1 is called intersystem crossing.

Transition from T_1 to the singlet ground state is forbidden, and as a result the rate constants for triplet emission are several orders of magnitude smaller than those for fluorescence⁴⁹.

2.1.2 Properties of fluorophores

2.1.2.1 Quantum yield

The fluorescence quantum yield is the ratio of the number of photons emitted to the number absorbed⁴⁹. The effectiveness of the fluorescent light emission for a given molecule is determined by the fluorescence quantum yield Q .

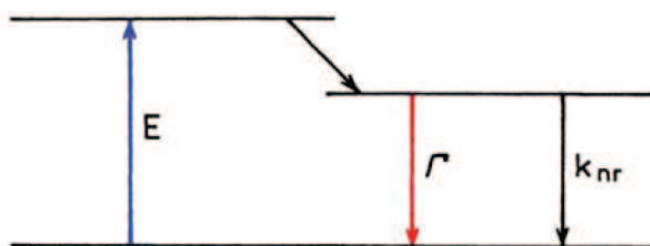


Figure 12. Jablonski diagram. E is the rate of excitation, Γ is the radiative decay rate and k_{nr} is the no-radiative decay rate.

The rate constants Γ and k_{nr} both depopulate the excited state. The fraction of fluorophores that decay through emission, and hence the quantum yield Q , is given by:

$$Q = \frac{\Gamma}{\Gamma + k_{nr}}$$

2.1.2.2 Fluorescence lifetimes

Fluorescent life times is the time available for the fluorophore to interact with or diffuse in its environment, and hence the information available from its emission. The lifetime of the fluorophore in the absence of nonradiative processes is called the intrinsic or natural lifetime, and is given by:

$$\tau_n = \frac{1}{\Gamma + k_{nr}}$$

In principle, the natural lifetime τ_n can be calculated from the absorption spectra, extinction coefficient, and emission spectra of the fluorophore⁴⁹.

2.1.2.3 Extinction coefficient

The molar extinction coefficient, or molar absorptivity (ϵ), is a measurement of how strongly a chemical species absorbs light at a given wavelength. The fluorescence intensity or brightness of a probe is determined by the product of molar extinction coefficient and quantum yield. This is why this value can be a useful criterion for the selection of dyes; as it is directly proportional to the value of fluorescence intensity.

Extinction coefficient is an intrinsic property of the species; which depends on the actual absorbance A of a sample, the path length ℓ , and the concentration c of the species. Thus is derived by the Beer–Lambert law, $A = \epsilon \cdot c \cdot \ell$.

2.1.2.4 Photo bleaching and quenching

Photobleaching is defined as the irreversible photochemical destruction of a dye molecule or a fluorophore. This phenomenon occurs when one fluorophore permanently loses the ability to produce fluorescence photons due to photo induced chemical damage. The probable reason of photobleaching is assumed to be linked to a transition from the excited singlet state to the excited triplet state. The excited triplet state is relatively long-lived and is chemically more reactive. Fluorophores exposed to too many cycles of excitation and emission therefore lose their ability to emit photons.

Fluorescence quenching refers to any process that decreases the fluorescence intensity of a fluorophore by a wide variety of processes. The principal cause of quenching is energy transfer between two adjacent molecules or a molecule and a metal by the process of fluorescence resonance energy transfer (FRET). Thus the quenching occurs when molecules in solution are in close proximity. The final molecule is then called the quencher. The molecules are not chemically altered in the process. A wide variety of molecules can act as collisional quenchers, as oxygen, halogens, amines, and electron-deficient molecules like acrylamide⁴⁹.

2.2 Principle of FCS and theoretical elaboration of correlation functions

2.2.1 Introduction and theory of Fluorescence Correlation Spectroscopy (FCS)

Diffusion is vital for non-directed transfer of molecules in a short distance in biological system especially in cellular environment (for example signalling between 2 neurons). The diffusion coefficient is the fundamental parameter in measuring diffusions of molecules in

solution. It helps in monitoring conformational changes in proteins/molecules upon binding to another and is directly related to the hydrodynamic radius and molecular weight of the molecules⁵⁰. Any change in the radius will alter the associated diffusion coefficient of the molecule. Such changes occur to most bio-molecules, in particular the proteins RNA and DNA, when they interact with other molecules (e.g. binding of ions or other bio-molecules), when they perform biological functions (e.g. enzymatic activity), or when they react to changes in environmental parameters such as pH, temperature or ionic composition (e.g. protein unfolding).

The advantages of FCS over other diffusion measuring techniques are- its ability to measure concentrations at the nanomolar level and its application of *in vivo* measurements. The core idea of the method is to analyze the fluctuations of the fluorescence signal resulting from the entering and leaving of individual fluorescing molecules into or out of a certain detection volume. This volume is basically given by the laser focus which has been generated by the microscope objective and the microscope detection properties. This volume is a region in solution where efficient fluorescence excitation and detection takes place (confocal volume).

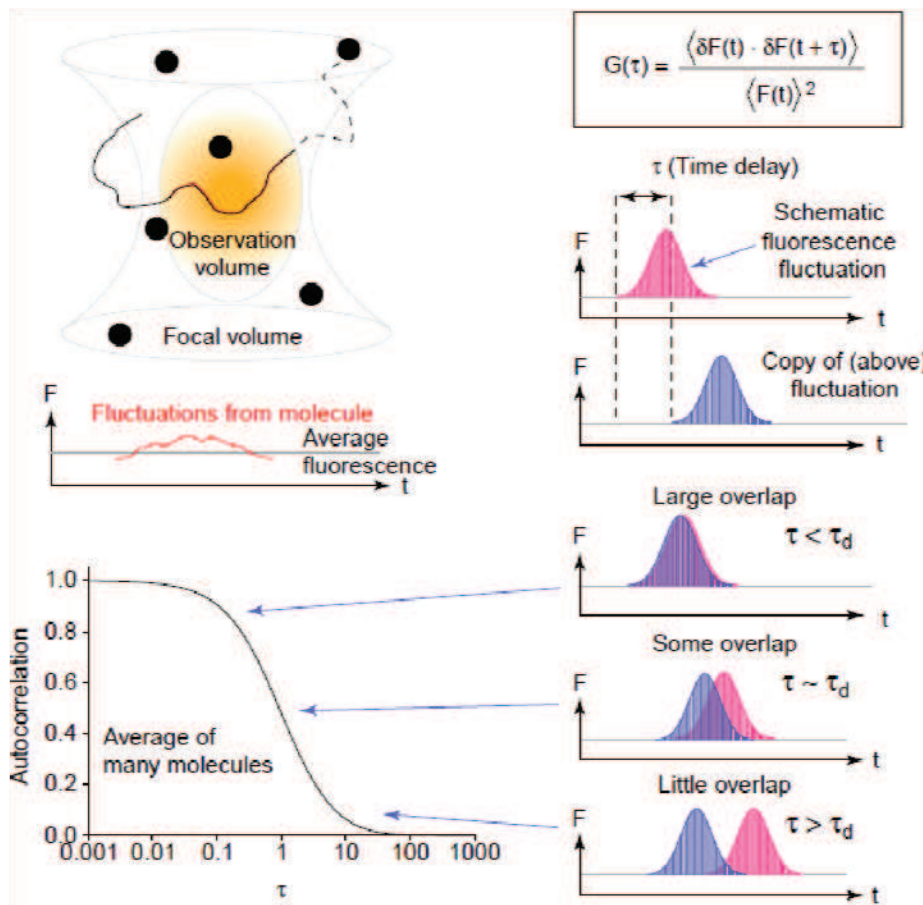


Figure 13. Schematic presentation of principles of fluorescence correlation spectroscopy⁵¹.

In *Figure 13*, a scheme of FCS is presented. Here, we can observe the general concepts of FCS. For FCS measurements the fluctuations in fluorescence intensity are recorded as a function of time (see schematized fluctuations below focal volume). The autocorrelation function (see equation, upper right in the scheme) describes the normalized variance of the fluorescence fluctuations and gives a measure of self-similarity after a time delay. The shape of the autocorrelation curve $G(\tau)$ provides the characteristic times for molecular residence in the confocal volume (τ_d). For the sake of simplicity a schematic fluorescence fluctuation from a single molecule is shown as a single burst and replicated after a time delay. In the case of a short time delay relative to the τ_d , the normalized integral of the overlapping region is close to 1, and the autocorrelation function has maximal amplitude. However, with longer time delays, the overlapping region gradually decreases until the autocorrelation function has fallen to zero. Various parameters can be extracted from an autocorrelation curve attributed to the diffusion of the particles in and out of the confocal volume.⁵¹

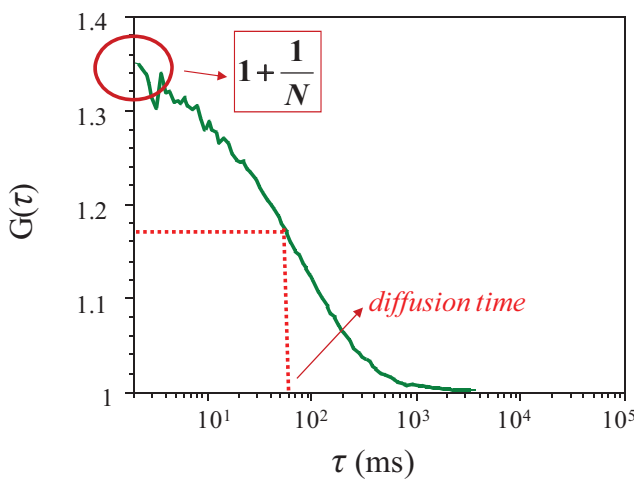
For the FCS measurements, concentration is a very critical parameter. If the concentration of interacting molecules are very small then only one of very few molecules are within the detection volume at any moment resulting in a strongly fluctuating fluorescence signal in response to the entering and leaving of one individual fluorescing molecule into or out of this volume. If the concentration of fluorescing molecules becomes too large (typically $> 10^{-8}$ M), then the contribution of the correlated photons from individual molecules, becomes very small compared with the contribution from uncorrelated photons from different molecules (explained with scheme in *section 2.2.3.1*). If the concentration is too low (typically $< 10^{-13}$ M), then the probability to find a molecule within the detection region becomes extremely low.

Since the FCS shows its best performance when number of observed fluorophores is as low as 10 or less. The confocal system created a revolution in FCS measurements; as the system reduces the number of observed molecules in the observation volume as well as increases the signal-to-noise ratio. Indeed the confocal system rejects any signal outside the desired volume and lowers the molecule number in the observation volume. Thus facilitates to increase the signal-to-noise ratio; enhancing its wider application with more sensitivity. On the other hand, the rate of diffusion of molecules in the observation volume is correlated with the fluctuation intensity. Thus the time dependent fluctuation gives an interpretation of diffusion coefficient with the help of autocorrelation function $G(\tau)$. Through $G(\tau)$ it is

possible to extract information of diffusion coefficient and number of molecules present in the observation volume. As a result, successful utilization of FCS is possible in the domains of various binding reactions, concentration of molecules, conformational or rotational changes in molecules 3D structure⁵².

2.2.2 Autocorrelation and cross-correlation function: their evolution

The output in the FCS is represented by the autocorrelation function $G(\tau)$. The physical meaning of the autocorrelation is that it is directly proportional to the probability to detect a photon at time τ if there was a photon detection event at time zero. In auto correlated signal, the two photons are originating from the same molecule and are then physically correlated. There is a temporal decay of the correlation $F(\tau)$ with increasing time τ and is proportional to the diffusion speed of the molecule or diffusion coefficient. The normalized autocorrelation function for the fluorescence fluctuations $\delta F(t)$ of the signal $F(t)$ is defined as:



$$G(\tau) = \frac{\langle F(t) \cdot F(t + \tau) \rangle}{\langle F(t) \rangle^2}$$

$$= \frac{\langle \delta F(t) \cdot \delta F(t + \tau) \rangle}{\langle F(t) \rangle^2} + 1$$

Here, $\delta F(t) = F(t) - \langle F(t) \rangle$

and $\langle F(t) \rangle = \frac{1}{T} \int_0^T F(t) \cdot dt$

We can express $F(t)$ as:

$$F(t) = kQ \int \omega(r)C(r, t) \cdot dr$$

Here, kQ = quantum yield and detector sensitivity

$\omega(r)$ = observation volume

$C(r,t)$ = fluorophore concentration over time (diffusion processes)

As the relative fluctuations are inversely proportional to the numbers of measured particles, it is important to minimize the average number of molecules in the focal volume (between 0.1

and 1000). This means, the corresponding concentrations range from subnanomolar ($\sim 10^{-10}$ M) to (sub)micromolar ($\sim 10^{-6}$ M) for a focal volume of about 1 femtoliter.

The expression of the autocorrelation function corresponding to fluorescent molecules freely diffusing in three dimensions is given by

$$G(\tau) = 1 + \frac{1}{\bar{C} V_{\text{eff}}} \frac{1}{1 + \frac{\tau}{\tau_D}} \frac{1}{\sqrt{1 + s^2 \frac{\tau}{\tau_D}}}$$

$$= 1 + \frac{1}{N} \frac{1}{1 + \frac{\tau}{\tau_D}} \frac{1}{\sqrt{1 + s^2 \frac{\tau}{\tau_D}}}$$

Here,

s = ratio of transversal to axial dimensions of the analysis volume

\bar{C} = spatial and temporal average of the concentration of molecules of the species of interest

V_{eff} = size of the confocal volume, that is to say the size of actual volume analysis of concentration fluctuations

Then $N = \bar{C} V_{\text{eff}}$, with N the average number of fluorescent molecules in the confocal volume.

In **Figure 14**, free diffusion of a molecule through the confocal volume is depicted. Here, 3 dimension 3D, 2 dimensional 2D and direct flow which can be termed as 1 dimensional diffusion 1D, are shown schematically. In parallel, the change in autocorrelation function for each type of diffusion is also demonstrated. We can observe that, during 2D and 3D diffusion the auto correlation function is slightly widened compared to 1D diffusion⁵³.

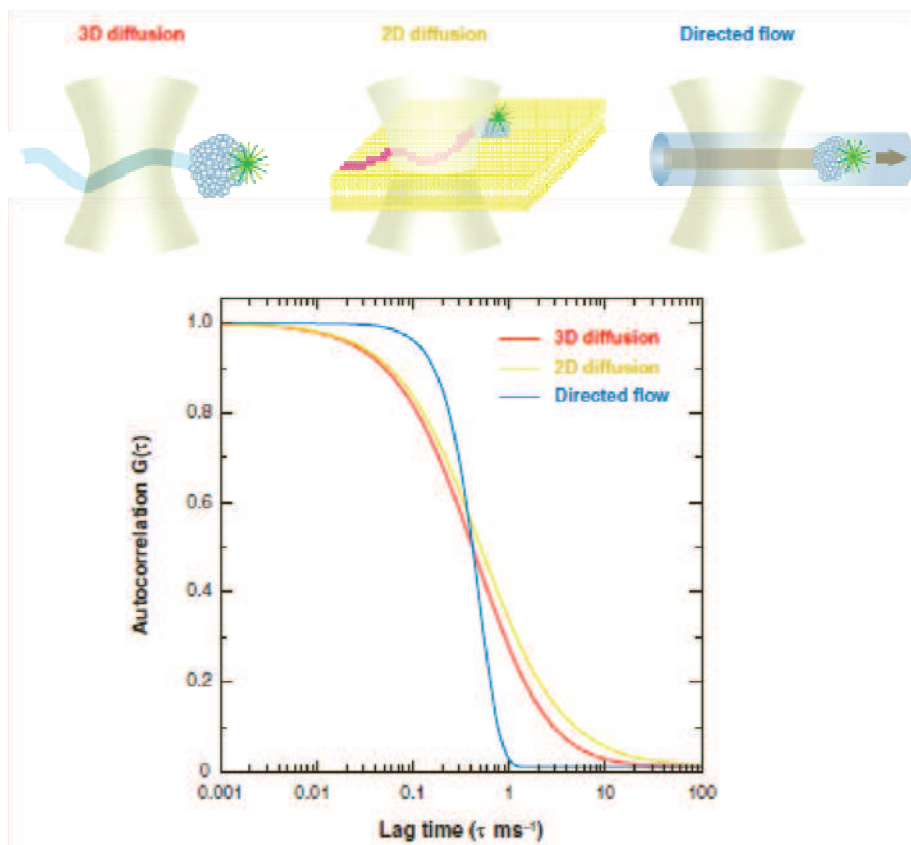


Figure 14. Model of autocorrelation curves for different kinds of particle motion: free diffusion in three dimensions (red), free diffusion in two dimensions and directed flow (blue)

In a solution in which molecules are free to diffuse, we can actually focus on a single sub-volume and let the random diffusion of molecules into and out of this volume replace scanning from sub-volume to sub-volume. In this case, the stochastic fluctuation occurs over time. The timescale of the fluctuations is defined by the characteristic diffusion time, τ_d that can be expressed in terms of the diffusion coefficient D ; such as

$$\tau_d = \frac{\omega^2}{4D}$$

Moreover the diffusion coefficient is related to the hydrodynamic radius of the (spherical) particle in solution by the Stokes-Einstein equation, so that the particle size can be estimated as:

$$D = \frac{kT}{6\pi\eta R}$$

Here,

R = hydrodynamic radius of the molecules

ω = radius of the observation volume in 2 dimensions (considered generally as a three-dimensional Gaussian intensity profile)

η = solvent viscosity

k = the Boltzmann constant

T = temperature

2.2.3 Photophysical aspects of FCS measurements: effects of physical parameters

2.2.3.1 Fluorophore concentration

Generally, the intensity of fluorescence varies linearly with the excitation intensity and the concentrations of fluorophores. In **Figure 15**, the concentration effect on FCS analysis is shown.

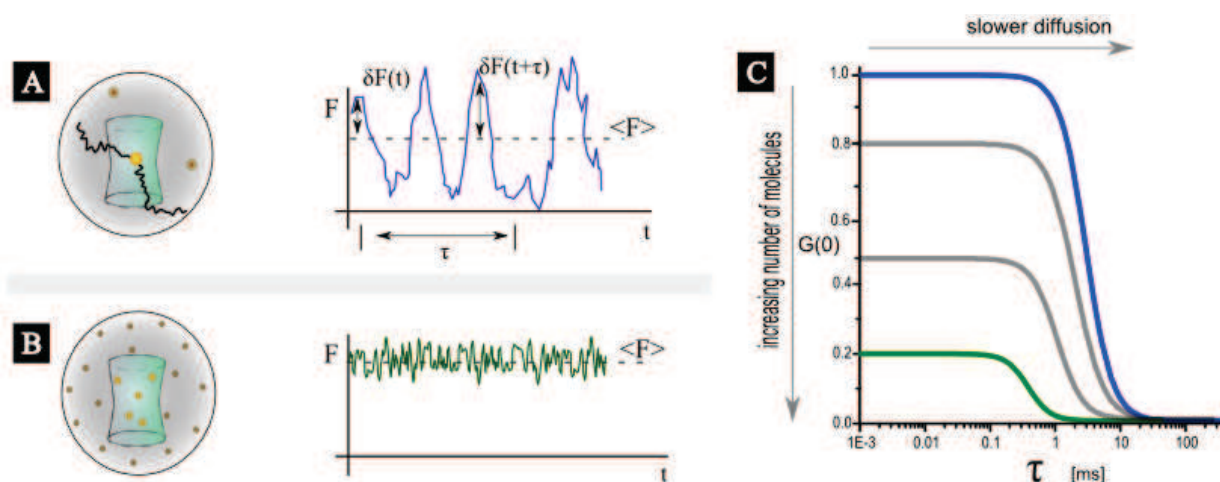


Figure 15. Schematic representation of concentration effect on autocorrelation curve. (A) Slowly diffusing fluorescent species at low concentrations give rise to large signal fluctuations around the mean fluorescence intensity value, (B) Fast diffusing molecules at high concentration produce small signal fluctuations, (C) The autocorrelation curves from (A) and (B). In case (B) the correlation curve will have a shorter diffusional correlation time and smaller $G(0)$ in comparison to case (A) [Picoquant: http://www.tcspsc.com/doku.php/general:fluorescence_correlation_spectroscopy-a_short_introduction].

Here, the comparative autocorrelation curve for two different concentrations of fluorescent molecules, having few and many molecules is demonstrated. We know the inverse amplitude of the curve equals the average particle number (N) within the focal volume. In the case when there are many molecules in the observation volume, there is a higher average fluorescence but a smaller relative fluctuation from each molecule. Therefore, the intensity fluctuations will overlap with each other and will not be as prominent as for the lower molecule number, making the result analysis difficult and erroneous. Thus, the effect of a single molecule is reduced or ‘washed out’ yielding smaller fluctuations and lower correlation amplitude. Conversely, a few molecules in the observation volume result in a low average fluorescence with larger fluorescence fluctuations detected from a single molecule and a higher correlation amplitude^{51, 54}. It means when the number of fluorescent molecules decrease, the relative fluctuation of fluorescence intensity against the average value increases. Here the concentration effect on cross correlation function is clear, where we can observe that $G(\tau)$ is decreasing with the increase in molecule number N , and N is directly proportional to the prepared solution concentration. This property is important during the result analysis by autocorrelation curve.

2.2.3.2 Molecular weight

Translational diffusion coefficient of a molecule is related to the molecular weight of the molecule. So it is possible to use FCS for determining molecular weights. Moreover, during characterization of molecules or particles, differences in molecular weight create distinct result, which is helpful in the result analysis. We already mentioned the relationship between diffusion time τ_d , diffusion coefficient D and hydrodynamic radius of the molecule R . The radius is related to the molecular weight, MW , of the molecule with a specific gravity \bar{v} by

$$V = MW\bar{v} = \frac{4}{3}\pi R^3$$

$$R = \left(\frac{3MW\bar{v}}{4\pi}\right)^{1/3}$$

Where V is the volume of the sample. These equations show that the radius and diffusion coefficient are dependent on the molecular weight⁴⁹.

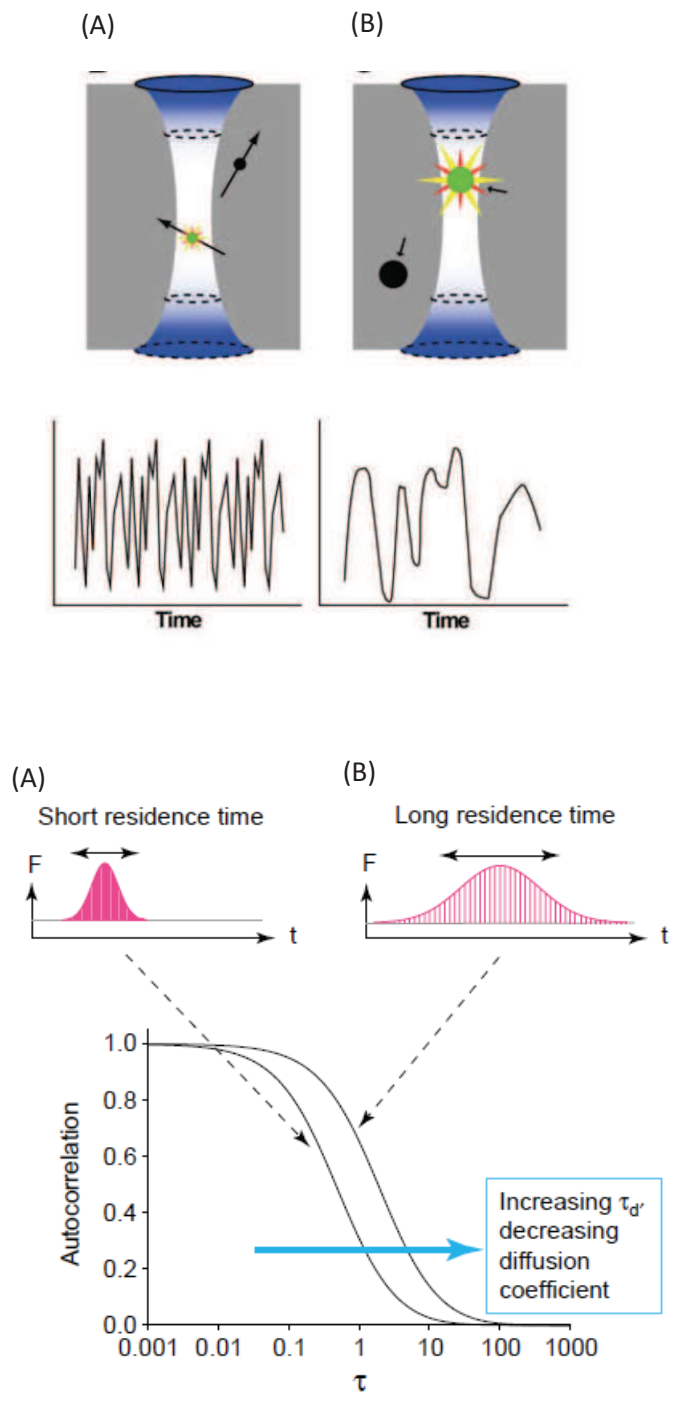


Figure 16. Effect of molecular weight on fluorescence fluctuation and the autocorrelation functions^{51, 54}.

Figure 16 shows that the molecular weight effect is explained schematically. Here, (A) represents low molecular weight fluorescent molecule while (B) represents fluorescent molecule having higher molecular weight than (A) but both of them are composed of same molecular origin. When fluorescent molecules enter and exit confocal volume, due to Brownian motion, fluorescence intensity fluctuates. Fluorescent molecules with greater weight shows wider fluctuation trace due to slower diffusion of the molecule through the confocal volume. As the half-value decay time gives an estimate of the mean diffusion time, longer τ_d thus are observed resulting in decreasing coefficients^{49, 54}.

2.2.3.3 Laser excitation power and triplet state

In fact, diffusion is just one of the several mechanisms that can cause intensity fluctuations. During FCS, due to the illumination of fluorescent molecules, an additional phenomenon called intersystem crossing occurs. In this case, the de-excitation of the molecule from the first excited singlet state (S_1) is not direct to the ground state (S_0) but is done through the triplet state (T) as shown in the Jablonski diagram for intersystem crossing in **Figure 17**.

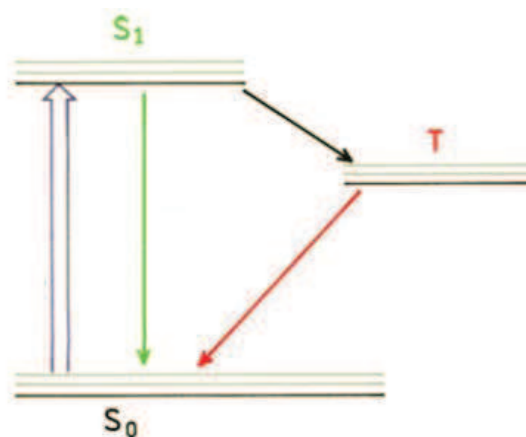


Figure 17. Jablonski diagram with intersystem crossing from the singlet (S_1) to the triplet (T) state⁴⁹.

The higher the illumination intensities, the more the fraction of fluorescent molecules participate in this intersystem crossing. The fluorophores in the triplet state are not observed, resulting in an apparent decrease in the number of fluorophores in the effective volume. If the fluorophores do not return to S_0 within the diffusion time, then only the amplitude of the correlation function will be changed. If the triplet fluorophores can return to S_0 within the diffusion time, then this is a mechanism that can cause fluctuations or blinking of the

fluorophores^{55, 56} as it is also observed in single-molecule experiments. Here, the relationship is defined as:

$$\text{Illumination intensities} \propto \text{Fraction of triplet (nT)} \propto 1/\text{Time in triplet } (\tau_T)$$

2.3 Application of FCS

FCS has various applications among which the nanomaterials characterization, with the aid of fluorophores, is occupying a great sector. The major sector of application is in biology.

2.3.1 FCS in biological media

The first insights into the dynamics of cellular interiors was proposed by Magde, Elson, and Webb in the early 1970s by demonstrating FCS applications through the kinetics of chemical reactions in the absence of external perturbations, and specifically to study the binding of ethidium bromide to DNA^{52, 57}. Thus their work engendered a revolution in quantitative fluorescence microscopy which now provides unparalleled insights into the cellular dynamics.

Further progress in cell dynamics study using FCS as a tool was carried out by different other research groups assigning remarkable contributions. Sironi *et al.*³⁹ demonstrated intracellular dynamic behavior of star-shaped gold nanoparticle with the aid of two-photon FCS. Dynamics of fluorescent 40 nm diamond nanoparticles in HeLa cells has been studied with two-photon fluorescence correlation spectroscopy (FCS) in order to determine their dispersion in the cell cytoplasm. These particles are engineered to improve cellular dispersibility by encapsulating within a lipid layer so that they are not trapped in the endosomes after cellular uptake. Thus the diffusion of the particles in the cytoplasm was improved by more than one order of magnitude and single particle was tracked by FCS in living cells⁵⁸.

We have to keep in mind that in case of low fluorophore concentrations or fluorophores with low quantum yield, enhancement of the fluorescence signal to noise ratio (SNR) is a prerequisite before FCS characterization of the molecules. Here, the use of metal particles can serve as fluorescence enhancement. On the other hand, when we would like to characterize metal nanoparticles, in many cases we can attach fluorescent molecules on the surface to be able to detect and characterize them by FCS. In both cases, the phenomenon of metal

enhanced fluorescence (MEF) can be observed. This is why, before discussing FCS applications, it is important to shed light on MEF effects.

2.3.2 Metal Enhanced Fluorescence (MEF)

A fluorophore in the excited state has the properties of an oscillating dipole. The excited fluorophore, when attached on a metal surface, can induce oscillations of the electrons in the metal. The electric field created by the metal can interact with the excited fluorophore and alter its emission. The interactions of fluorophores with metallic surfaces can have a number of useful effects, including increased quantum yields, increased collection efficiency, increased distances for resonance energy transfer, decreased fluorophore lifetimes and decreased interference from unwanted background emission⁴⁹.

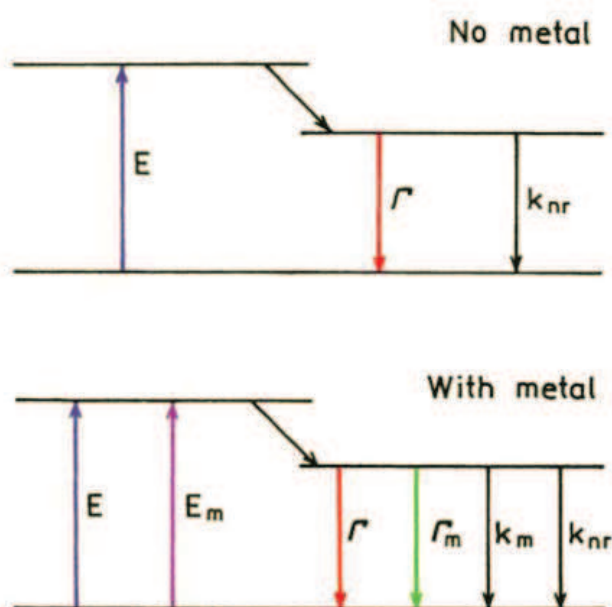


Figure 18. Jablonski diagram demonstrating MEF effects- without (top) and with (bottom) the effects of near metal surfaces. E is the rate of excitation Γ is the radiative decay and k_{nr} is the non-radiative decay without metal. E_m is the additional excitation, Γ_m is the additional radiative decay and k_m is the additional non-radiative decay in the presence of metal⁵⁹.

Figure 18 depicts a clear idea of MEF effects and its explanation. We know that in the absence of metals the quantum yield Q_0 and lifetimes τ_0 are given by-

$$Q_0 = \frac{\Gamma}{\Gamma + k_{nr}}$$

$$\tau_0 = \frac{1}{\Gamma + k_{nr}}$$

Now we consider the effect of a metal on the fluorophore properties. If the metal results in an increased rate of excitation ($E + E_m$) this will result in increased brightness without changing the quantum yield or lifetime. Metal enhanced excitation can also result in selective excitation of fluorophores near the metal. Another possible effect is an increase in the radiative decay rate. In this case, the quantum yield Q_m and lifetime τ_m of the fluorophore near the metal surface are given by-

$$Q_m = \frac{\Gamma + \Gamma_m}{\Gamma + \Gamma_m + k_{nr}}$$

$$\tau_m = \frac{1}{\Gamma + \Gamma_m + k_{nr}}$$

These equations give elaborate predictions for a fluorophore near a metal surface. As the value of Γ_m increases the quantum yield increases while the lifetime decreases⁴⁹. The coupling between the free electrons responsible for surface plasmon resonance and nearby fluorophores, can increase the local electrical field and enhance the excitation and emission rates and decrease the lifetimes of excited states⁶⁰.

Based on the principles of MEF, many research groups have done several spectroscopic studies applying and/or incorporating the phenomenon of MEF. Some are summarized below:

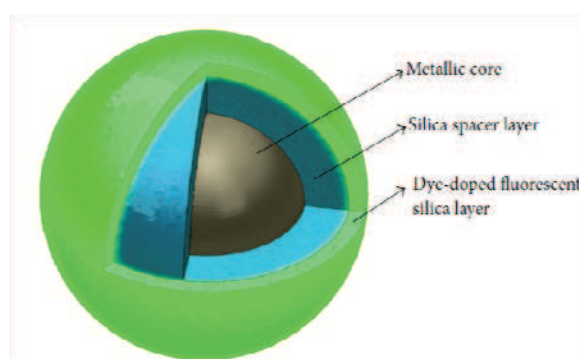
2.3.3 MEF applications

The metal-enhanced fluorescence (MEF) is the background of the plasmonic nano -antennas and represents a powerful technology to increase the detection sensitivity of various biological assays. Brouard et al. performed direct molecular detection of target nucleic acids at femtomolar concentration by combining the molecular recognition capabilities of a cationic conjugated polymer transducer with fluorescent core-shell NPs. Aggregated NPs maximize the proximity of polymer donor and acceptor NPs, each hybridization event is signalled by the large number of excited reporter fluorophores located in the vicinity of metal core-shell aggregates⁶¹. Yu He *et al.* incorporated surface plasmon enhancement effect by combining 50 nm silver thin films with a TIRF microscope, which provided brighter and more contrasted fluorescent live cell membrane images with reduced photobleaching due to shorter fluorophore lifetime⁶². On the other hand, Aouani *et al.* developed optical

nanoantenna which relates to its amplification of the local excitation intensity and quantified the electromagnetic amplification on aperture antennas by taking advantage of the intrinsic non linear property of the fluorescence process⁶³. And this quantification is possible due to MEF effects created by the nano-antenna.

Core-shell metal-silica nanoparticles (scheme in **Figure 19**) are a bright example where MEF is incorporated in engineering of fluorescent nanoparticles. Metallic cores exhibiting plasmonic properties in the UV and visible regions of the electromagnetic spectrum were used to increase substantially the brightness and stability of organic fluorophores encapsulated in/up the silica shells⁶⁴.

Figure 19. Schematic representation of the MEF-capable multilayer core-shell nanoparticle⁶⁴.



These metal-silica core-shell nanoparticles combine the properties of more conventional dye-doped silica NPs (i.e., high optical detectability, large spectral coverage, excellent chemical and physical stability, low toxicity, high solubility in water, and easy conjugation to target biomolecules) together with the enhanced luminescence intensity, excitation cross-section, and photostability resulting from the plasmonic interactions occurring in these nanostructures⁶⁴.

2.3.4 Characterization of nanoparticles

Conjugation of fluorescent molecules on GNP and their effective characterization is a vital part of the sensitive biosensor fabrication. The detection of very low concentration (at nanomolar range) of fluorescent molecules either conjugated or free in the buffer system is a challenge as most of the characterization tools for example UV-Visible spectroscopy are incapable of reaching such high sensitivity³⁹. Fluorescence provides measurement opportunities of micro and macromolecules due to their conjugation upon them and these measurements can be beyond just imaging. Fluorescence Correlation Spectroscopy (FCS) is a powerful technique to resolve this challenge because of not only its single molecule sensitivity but also of the ability to determine molecular interaction and diffusion at very

small sample size. Like any other interactions studied by FCS, aggregation of fluorescently labelled particles (NPs) can be measured by this technique.

Sharma *et al.* used FCS to study the diffusion dynamics and the hydrodynamic radius of gold nanorods of different aspect ratios. They determined diffusion coefficients of the the particles and found that the hydrodynamic radii of gold nanorods were increased by few orders of magnitude in FCS compared to TEM analysis. This might be due to the possible contributions from CTAB capping in the system. Thus they could analyze the contribution of surface capping agent on nanoparticle surface by FCS⁵³.

Dominguez-Medina *et al.* demonstrated in situ the adsorption of bovine serum albumin (BSA) on citrate-stabilized gold nanospheres based on an increase in the nanoparticle hydrodynamic radius but have not observed the same on PEG coated nanospheres⁵⁴. They have also notice that there is no aggregation either of GNPs or of the protein itself. This result is important from the toxicological view point as proteins in the biological media can aggregate GNPs which may complicate cellular uptake and clearance; also may cause cell death. On the other hand protein aggregation due to NPs is associated with several diseases⁵⁷. Ray *et al.* demonstrated fluorescent oligo nucleotide conjugation on 50 nm silver nanoparticles by FCS contributions and distinguished between the spatial diffusion of bound and unbound fluorescent oligonucleotides⁶⁵.

FCS has been used successfully to determine hydrodynamic radii of magnetic nanocrystals (NC) of 11 nm core and size-selective separation of aggregates larger than 60 nm was achieved with the aid of applying a magnetic field of 0.24 T⁵². Tang *et al.* used 14 nm silver nanoparticle (SNPs) to covalently bind alpha fetal protein (AFP) antibody to enlarge molecule weight difference on biomolecules. Then they performed the antigen-antibody reaction by adding Alexa Fluor 647 labeled AFP antigen in the immunoassay. Thus the conjugated SNPs showed significant increase in the diffusion times of biomolecules and antigen-antibody immune reaction was successfully monitored by FCS⁶⁶.

Chapter 2

FCS: set-up and characterization

3. Fluorescence Correlation Spectroscopy (FCS): Set-up and characterization of the system

Summary

3.1 Set-up and working principle of FCS

3.1.1 Description of optical assembly

3.1.2 Source of excitation

3.1.2.1 Installation and alignment of laser

3.1.2.2 Installation of power variable attenuator for lasers

3.1.3 Spectral filters

3.1.3.1 Band-pass filter (Excitation filter)

3.1.3.2 Dichroic mirror

3.1.3.3 Emission filter

3.1.4 Spatial filters

3.1.4.1 Microscope objective

3.1.4.2 Beam expander (Telescope)

3.1.4.3 Confocal system (Pin hole)

3.1.5 Photo detectors and correlator

3.2 FCS set-up characterization

3.2.1 Measuring the resolution of the FCS set-up by Point spread function (PSF)

3.2.2 Characterization of the correlation function by measuring probe concentrations

3.2.3 Photo physical phenomenon during FCS: triplet state evolution

This chapter concerns the assembly of the FCS, which we have developed in the frame-work of the project “NanoTox” at the Laboratory CSPBAT, in University Paris 13. This spectroscopic set-up is the first one built in our laboratory, which aims to address both physical and biological questions. In the previous chapter, theory and applications of FCS have already been cited. Now in this chapter, along with the set-up and optical assembly of the FCS system (section 3.1), we are going to present its detailed characterization in the spectral and spatial domain (section 3.2). This optical assembly and detailed characterization constitute a very important part of my thesis work.

The main aim of using FCS is to study single molecules. To achieve such objective we have to overcome two issues; first we have to work with very low concentration solution. In this case, the probability of finding a molecule in detection volume can be smaller than unity. This can be achieved either by diluting solution or by minimizing detection volume. Second, the molecule of interest has to be observable. This is done by adding a fluorescent dye to the molecule. The organic dyes have π electron systems which enable them to have a relatively large absorption cross section and a high fluorescence quantum yield and are thus easily detectable using laser induced fluorescence. Different spatial filters have been used to improve the single molecule detection capability of the FCS system. Details of the spectral and spatial filters and all other components with which the set-up is built up are described below.

3.1 Set-up and working principle of FCS

3.1.1 Description of optical assembly

The FCS system is an assembled apparatus designed and built during the thesis (scheme of the optical assembly in *Figure 20*). This system has been set-up from composite optics combined with confocal system. The whole system is connected to an inverted microscope (Nikon). The confocal fluorescence spectroscopy consists of an excitation system (laser), a telescope, a dichroic mirror, a sample holder with the objective, a Piezo Nanopositioning Stage (Physik Instrumente PI GmbH, Walbronn, Germany), some lenses, a confocal hole, a splitter cube, some emission filters, photodetectors and a computer with software processing of the fluorescence signal on LabVIEW. The optical set-up is installed on an optical table equipped

with a vibration control system (S-2000 Stabilizer Vibration Isolators and Optical Table, Newport Corporation, USA).

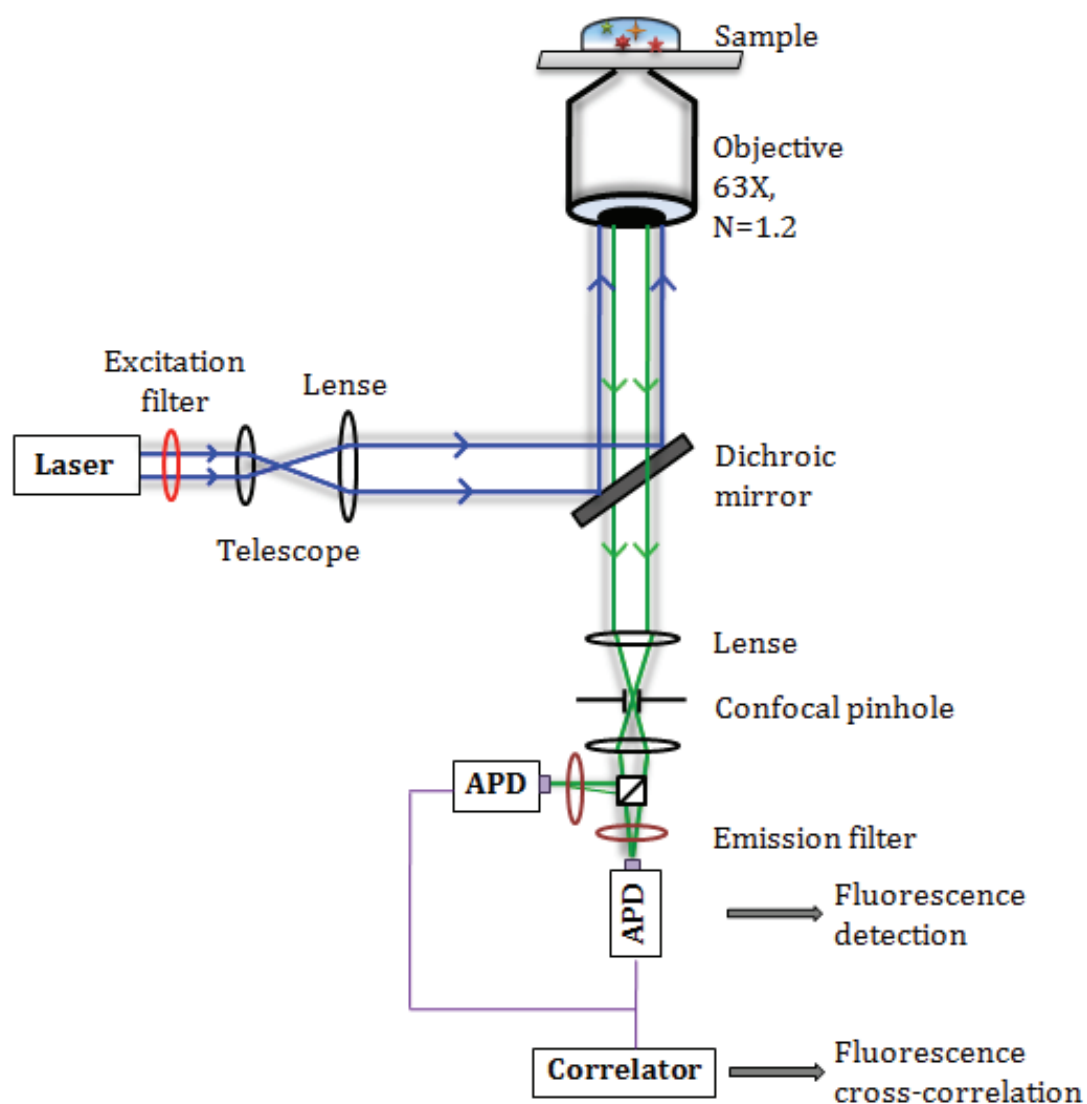


Figure 20. Schematic presentation of the experimental set-up of FCS

The sample can be translated in the three directions in space with the piezoelectric stage that is controlled by computer program accompanied by software that is developed using LabView (National Instruments, Texas, USA).

All the major optical components and instruments are described below in detail.

3.1.2 Source of excitation

The excitation system is formed by a monochromatic light source (laser) and an optical attenuator for varying the beam. In our set-up, we have installed three laser wavelengths: 488 nm (Cobolt MLDTM lasers), 532 nm (The Optoelectronics Company, UK) and 633 nm (HeNe Laser, ThorLabs SAS, France). Laser beams were accompanied with their respective excitation and emission filters, and dichroic mirrors. The laser power attenuator, which is the combination of a half-wave plate and a polarizer, are also mounted and aligned to the laser beam.

3.1.2.1 Installation and alignment of lasers

The three lasers are installed in the same manner. Before attaching the laser, two diaphragms are installed in the output remaining as parallel as possible to the laser line. These two diaphragms are points belonging to the line they define.

The larger the distance between the two diaphragms is (a few meters), the more the deflection of the laser beam is remarkable. Thus if the beam moves away a few millimeter from the center of the first diaphragm, it moves away from a few centimeters from the center of the second diaphragm placed over a meter of the first diaphragm. The purpose is to align the laser beam at the center of the two diaphragms to obtain a parallel laser beam. For this, the alignment needs two steps: i) translating the laser so that the beam passes through the center of the first diaphragm and ii) rotating the laser to focus on the second diaphragm while remaining centered on the first diaphragm. Finally, after getting a fine line passing through the two diaphragms, the mechanical mounting of the laser is fixed carefully.

3.1.2.2 Installation of power variable attenuator for lasers

The laser power attenuator is the combination of a half-wave plate and a polarizer. They must be installed in the optical line of the laser to allow variation of the laser intensity during practical measurements. In addition, since the three lasers do not have the same power and to lower the power of the laser beam, some optical density (opaque filter) filters need also to be raised until obtaining the desired excitation power. This optimized laser power is required in order to produce a signal that is satisfactory and non-destructive to fluorophores and photodetectors as photodetectors are sensitive to the overload of high laser intensity.

The polarizer is an optical filter that selects a specific polarization direction in a light wave passing through it, according to the polarizer direction. Indeed, light is an electromagnetic wave. The direction and magnitude of the electric field corresponds to its polarization as the wave propagates along a plane of polarization. We have a goniometer, equipped with the half-wave plate that can be rotated to select a polarization angle.

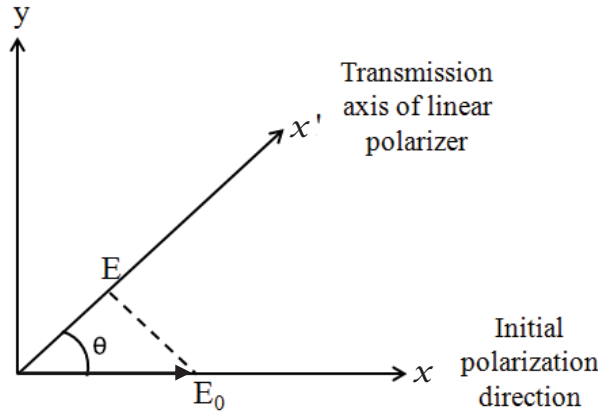


Figure 21. Transmission through linear polarizer.

In **Figure 21**, a scheme of a source of linearly polarized light is presented with the electric field vector E_0 oscillating along the x-axis, defined as the direction of polarization. If we suppose a polarizer is placed in front of the light source, with its transmission axis along the x' -axis making an angle θ with the polarization direction of the incident light, only the component of the electric field vector that is along the transmission axis can pass through the polarizer. Therefore we only consider the projection of E_0 along the transmission axis. As light passes through the polarizer, the amplitude of the electric field vector is given by $E = E_0 \cos \theta$. The intensity I of the light is shown to be proportional to $|E|^2$. Hence, the intensity of the light after it passes through the polarizer is proportional to $E_0^2 \cos^2 \theta$. Equivalently, the transmitted intensity I is related to the incident intensity I_0 by the following equation, which is called the transmission function of the linear polarizer (according to Malus' law).

$$I = I_0 \cos^2 \theta$$

The polarized light is absorbed by the laser power meter (NOVA, OPHIR Photonics, USA) at the outlet of the polarizer and the value of the beam power is digitally displayed on the combined Photodiode Power Sensors (OPHIR Photonics, USA). Lasers used in our set-up have a known linear polarization, for the red and green laser the polarization is horizontal

(horizontal polarization plane relative to the axis of incidence) in contrast to the blue laser which has a vertical linear polarization.

3.1.3 Spectral filters

3.1.3.1 Band-pass filter (Excitation filter)

In front of the laser beam outlet, a narrow band pass filter is used as a filtering system which is mounted in order to pass the selected range of laser wavelength for the experimental set-up and thus it block the unwanted light at wavelengths away from the actual laser line, including spontaneous emission often observed in solid-state lasers or the plasma lines of gas lasers. The excitation filter removes the undersized laser lines in order to not disturb the excitation and selects the main wavelength. It is placed just outside the laser or outside the platform.

3.1.3.2 Dichroic mirror

The dichroic mirror is a mirror which reflects light in a certain range of wavelengths and transmits the wavelengths not belonging to this range. In this assembly, it allows to select the emitted light from that of the excitation light. Dichroic mirror are coated with an antireflective coating in order to maximize the transmission of the emission signal and eliminate coherent interference artifacts. Upon excitation, the sample emits light of longer wavelengths. The mirror is aligned just in front of the emitted light from the sample and in 45° angle for the excitation beam. Thus this filtering system reflects the laser light and transmits the fluorescence photons at higher wavelengths. The characteristic features of the dichroic mirrors for the wavelengths of 633 and 488 nm are shown in **Figure 22**.

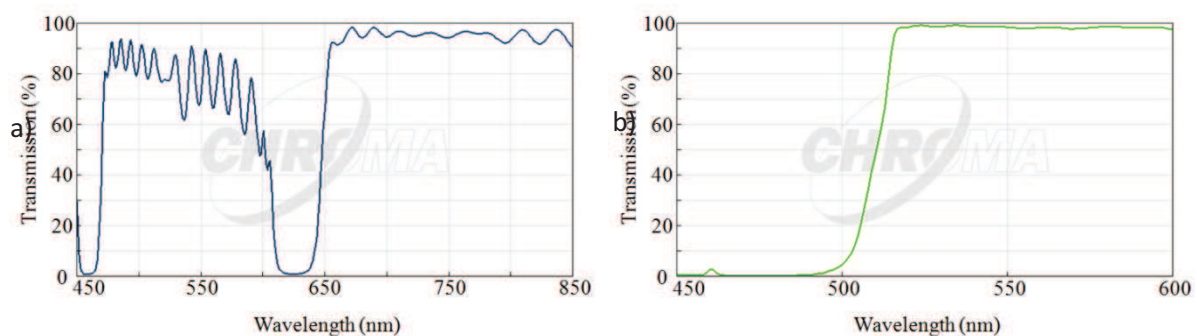


Figure 22. Characteristic features of dichroic mirrors: Transmission spectrum plotted for the wavelength range of a) 450-850 nm for red laser (z633rdc), and b) 450-600 nm for blue laser (T510lpxrxt). (<http://www.chroma.com>)

3.1.3.3 Emission filter

Emission filters are placed just after the pinhole and in front of the APD detectors in order to rectify the emission coming from the sample and to protect the detectors from photon overload. In **Figure 23**, the characteristic features of the emission filters for the wavelength of 633 and 488 nm are shown.

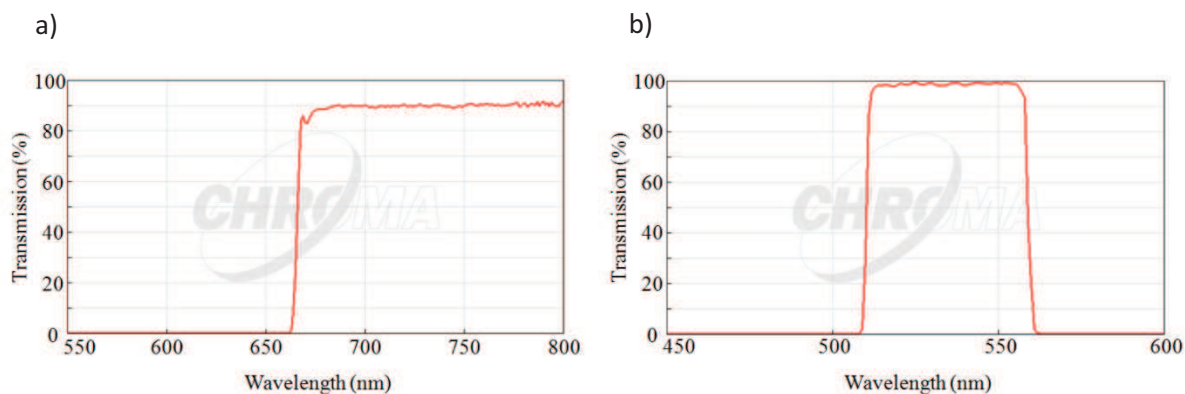


Figure 23. Characteristic features of emission filters: Transmission spectrum plotted for the wavelength range of a) 550-800 nm for red laser (HQ665lp), and b) 450-600 nm for blue laser (ET535/50m). (<http://www.chroma.com>)

3.1.4 Spatial filters

3.1.4.1 Microscope objective

For the best excitation and collection of fluorescence, we use a 63X high numerical aperture (N.A. = 1.2) water immersion objective. We can define N.A. as:

$$N.A. = n \sin \alpha$$

with n , the refractive index of the medium between the objective front lens and the sample and α , the maximum angle of focalization or one-half angular aperture of the objective

The numerical aperture of a microscope objective is a measure of its ability to collect light and to resolve fine sample details at a fixed object distance. Thus our high numerical aperture objective can create image with high resolution. These type of objectives are designed to focus and collect light in a high refractive index environment greater than air, such as water or oil, to avoid optical aberration. Moreover, for experiments with aqueous samples, water-immersion objectives have a clear advantage of focusing the excitation light and collecting the emission efficiently.

3.1.4.2 Beam expander (Telescope)

The laser beam should be expanded to overfill the rear pupil of the microscope objective and as a consequence to define the smallest confocal volume. For expanding the laser excitation beam at the entrance of the microscope objective, we used a telescope system (*Keplerian beam expander*) (scheme in **Figure 24**). It consists of two convergent lenses: the first lens (A) with a focal length of f_A , the second lens (B) with greater focal length of f_B . Both lenses must be arranged to match the image focus of the first lens with the object focus of the second lens.

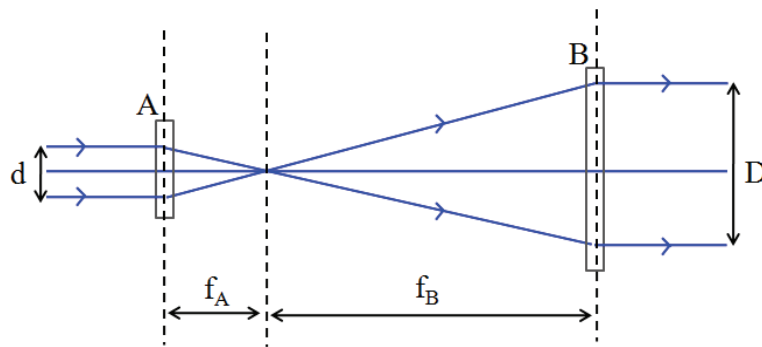


Figure 24. Expansion of the laser beam using a telescope

If diameters of the laser beam before and after expansion are d and D , then expansion ratio or magnification of the beam expander is defined as:

$$m = -\frac{f_B}{f_A} = \frac{D}{d}$$

In our set-up, the laser beam diameter is magnified 4 times in order to illuminate our objective pupil perfectly.

3.1.4.3 Confocal system (Pin hole)

Confocal optics and improved electronics helped to increase signal and to reduce noise. Optics are designed to reduce the collection of out-of-focus light and to limit the image detection to the desired focal plane of in-focus light (in the sample plane), which increases contrast and effective resolution. This is achieved by first, minimizing the detection volume with a laser beam focused at the limit of resolution with a high numerical aperture (NA) objective. Second, out-of focus light is eliminated by introducing a pinhole or a field aperture

in the conjugate image plane and before the detector. Fluorescence signals from the out-of-focus planes are excluded by the field aperture and are therefore not recorded by the detector⁴⁸. The conjugation of the objective with the pinhole creates a spatial filter, which efficiently cuts the sampling volume to a diffraction limited size.

Another aspect is the intensity of the excitation laser light that should be low enough since the dye emission depends linearly with the excitation (typically a few tens of microwatts). At higher intensities the detection volume appears to increase as the emission of the dye molecules in the centre of the confocal volume saturates and, therefore, the relative contribution of the molecules at the periphery increases. This effect must be taken into account and calibrated when performing experiments with dyes of different saturation limit⁶⁷. The best signal to background ratio were obtained with pinholes of the size of the image of the laser beam waist in the plane of the pinhole. In our set-up, the pinhole is 50 μm in diameter.

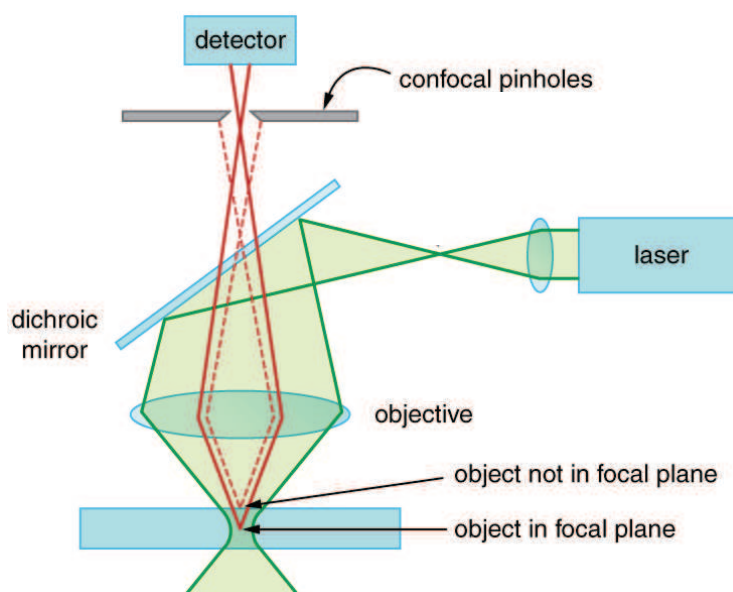


Figure 25. A schematic representation of the optical path in a confocal fluorescence microscope.

In **Figure 25**, the working principle of the confocal system composed of a pinhole is represented. Here the excitation beam (green) is directed to the microscope objective by a dichroic mirror and focused onto the sample. The fluorescence signals (solid red) emitted by the sample are collected by the same objective and imaged through a pinhole onto a detector. The off-focal plane signal (dashed red) is rejected by the pinhole.

3.1.5 Photodetectors and correlator

Photodetectors

The photodetectors are instruments that convert light into measurable electrical signal. Here, the photodetectors used are Avalanche Photo Diodes (APD). When a photon is absorbed, the APD can generate thousands of electrons by avalanche effect to produce a detectable electrical signal. In FCS, it is absolutely essential to use detectors with high quantum efficiency (QE) that can be served as APD. In our set-up, we have used APD with QE ~70% at 700 nm (SPCM-AQRH, Excelitas technologies, Canada). This APD is a Module that can work in single photon counting regime over a wide range of wavelengths (400-1000 nm). The QE or Photon Detection Efficiency (PDE) of the APD is shown in **Figure 26**.

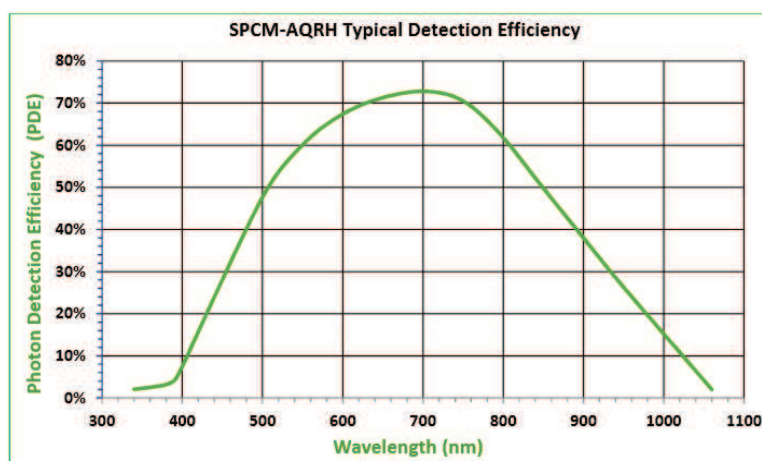


Figure 26. Typical Photon Detection Efficiency (PDE) vs. Wavelength (<http://www.excelitas.com>).

The photodetectors are fixed and have mechanical mounts which can be used to adjust their position in x, y and z axes. Thus the photodetector is aligned on the optical axis of the emission fluorescence to get the maximum of emitted photons from the sample.

We have used two APD detectors to make cross-correlation of the fluorescence signal. Why two detectors are used in FCS? All of the photon counting devices (photomultipliers as well as APD) have a problem of ‘afterpulsing’ or ‘dead time’ of few nano seconds during counting photons. In such devices, a strong peak, characteristic of afterpulsing, distorts the autocorrelation function below 100 ns and up to 1 ms. A simple solution to reduce the afterpulsing noise consists in splitting the collected light between two photo detectors by a 50/50 beam splitter (Chroma) and cross-correlating their outputs. In that case, the dead time is compensated due to the cross-correlation of the signal and the resulting correlation function is

formally similar to the autocorrelation function that is free from the afterpulsing noise⁶⁷. Thus continuously measuring the intensity of fluorescence with two detectors implies that no information was lost.

Correlator

The APD are connected to a multi-channel correlator ALV-7004/USB Multiple Tau Digital Correlator (ALV-Laser GmbH, Langen, Germany) which is connected with the computer to read the output by LabView (National Instruments, Texas, USA). This correlator carries out directly the calculation of the correlation function including the recording of the intensity trace versus time.

The correlator has the capability to measure the temporal correlations with high accuracy for periods ranging from less than a microsecond to several minutes. It can convert the optical signal to electrical signal by forming correlation function and this correlation function is presented as a function of the logarithm of the lag time. This displays the correlation function at all time scales in a single measurement. The piezoelectric stage and thus the stage holder are controlled by computer using the same Labview software connected with the correlator. Thus a combined activity of sample positioning and correlation acquisition is possible in parallel.

3.2 FCS set-up characterization

3.2.1 Determination of the resolution of the FCS set-up by Point Spread Function (PSF)

The first parameter that has to be determined to characterize an optical system is its excitation volume. It means determining precisely the axial and lateral dimensions of this volume. To perform this, PSF measurements are done by using fluorescent polystyrene latex beads (Life technologies, France).

The ideal PSF is the three-dimensional diffraction pattern of the light emitted from an infinitely small point source and transmitted to the image plane through a high numerical aperture (NA) objective. It is considered to be the fundamental unit of an image in theoretical models of image formation. When light is emitted from such a point object, a fraction is collected by the objective and focused at a corresponding point in the image plane. However, the objective lens does not focus the emitted light to an infinitely small point in the image plane. Rather, light waves converge and interfere at the focal point to produce a diffraction

pattern of concentric rings of light surrounding a central, bright slit when viewed in the x-y plane. The radius of the slit is determined by the NA, thus the resolving power of an objective lens can be evaluated by measuring the size of the Airy disk (named after George Biddell Airy).

Measuring the PSF consists, in confocal fluorescence microscopy, to record the image of a fluorescent bead of diameter smaller than the radial and axial elongation of the confocal volume (ω_x , ω_y and ω_z). The obtained image is the fluorescence intensity profile of the beads in the directions of x, y and z; that is characteristic to the axial resolutions.

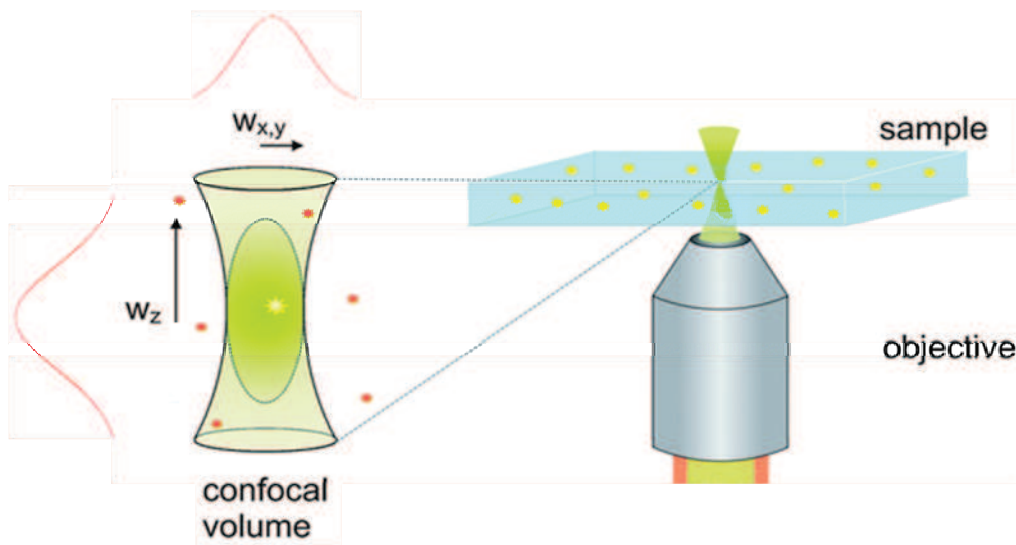


Figure 27. Schematic presentation of confocal volume on a sample composed of lateral and axial axes, along with the Gaussian laser beam pattern. (<http://cam.facilities.northwestern.edu/588-2/fluorescence-correlation-spectroscopy>).

Theoretically, the axial resolutions are the radial and axial elongation of the confocal volume as $\omega_r = \omega_x = \omega_y$ and ω_z (in **Figure 27**). The resolution depends on the wavelength (λ) of the laser used, the numerical aperture (N.A.) of the objective of the microscope, the refractive index (n) of the medium and the use or not use of the confocal pin hole:

With the confocal pin hole

$$\omega_x = \omega_y = \frac{0.46 \times \lambda}{\text{N.A.}}$$

$$\omega_z = \frac{1.4 \times \lambda \times n}{\text{N.A.}^2}$$

Without the confocal pin hole

$$\omega_x = \omega_y = \frac{0.66 \times \lambda}{\text{N.A.}}$$

$$\omega_z = \frac{2 \times \lambda \times n}{\text{N.A.}^2}$$

The excitation volume or confocal volume is calculated using the formula of the volume of an ellipse whose radius is ω_x and the height in z-axis is ω_z . These values become smaller when

we use a confocal pinhole. Moreover, the resolution is better if the refractive index of the lens in the objective is higher than the medium of the sample. Since the resolution of an optical system is its ability to distinguish fine details, it is important to determine it in order to characterize the microscope performances.

In order to make such measurements, 170 nm fluorescent beads were smeared and dried on glass lamellas. As the PSF measurement requires the finding of a single bead and not an agglomerate of spheres, a droplet of a much diluted beads solution was deposited on the glass slide. Upon placing the slides in the sample holder on the piezo-electric stage, the slide is moved in the x, y or z direction to observe the peak intensity indicating single fluorescent bead.

The intensity profiles along the x, y and z directions are recorded (in **Figure 28 A**) and processed by IGOR Pro software to plot the theoretical average curve profiles (curve fitting), which are Gaussian curves (in **Figure 28 B**). The resolution was determined on the theoretical curve at the height of $1/e^2=0.135$.

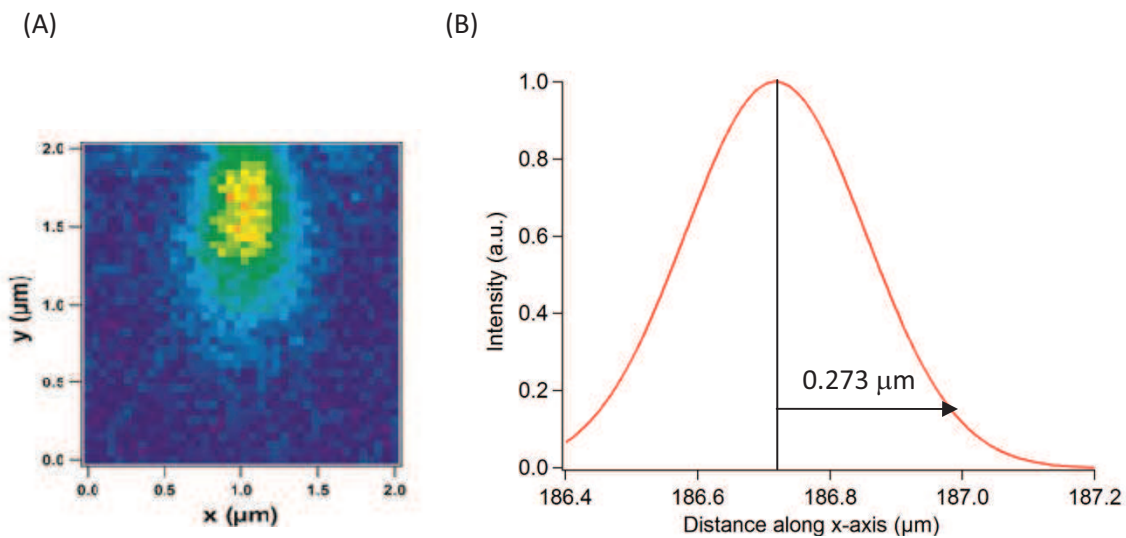


Figure 28. (A) Image of a fluorescent latex bead of 170 nm of diameter (30X30 pixels). (B) Normalized curve showing width of beam waist along x-axis which is 0.273 μm.

In the case of the red laser (633 nm), the experimental values were averaged from thirty measurements with and without the confocal hole. Moreover, from the experimental cross-correlation curves of Alexa 647 molecule, the diffusion time τ_D is determined. So, another experimental value of resolution can also be calculated using τ_D and corresponding to the diffusion D of Alexa 647. The theoretical and experimental values are presented below in

Table 1:

Table 1. Values of the lateral and axial resolutions, and confocal volume for 633 nm laser

Laser 633 nm	With pin hole		Without pin hole	
	Theoretical	From PSF	Theoretical	From PSF
$\omega_x=\omega_y$ (μm)	0.243	0.273	0.348	0.385
ω_z (μm)	0.819	0.700	1.169	1.163
V_{exc} (fL)	0.304	0.341	0.889	1.083

First, the experimental measurements are mostly superior to the theoretical values of the axial resolutions (ω_z) with or without confocal hole. Indeed, during practical measurements, optical aberrations or little imperfection in photo detector alignment can cause these differences in experimental values from the theoretical ones. We have also calculated the value of ω_x using the formula $\tau = \frac{\omega^2}{4D}$ from the Alexa 647 molecule diffusion time determined by FCS measurements and hence, we got $\omega_x = 0.273 \mu\text{m}$. Then confocal volume, V_{exc} was determined using the values of ω_x and ω_z

Finally, the relationship between the excitation volume with and without confocal pin hole show a gain of 31% experimentally against 34% theoretically. The confocal aperture of 50 microns in diameter thus improves the resolution of the confocal microscope using the red laser.

3.2.2 Characterization of the correlation function by measuring probe concentrations

The characterization of the correlation function has been done by measuring the concentrations of several solutions of the same fluorescent molecules having different molecular concentrations. The principal idea of this study is to observe the proportionality between the correlation curves and the various concentrations. The concentration of the fluorescent molecules is first measured by UV-Visible spectroscopy. Our starting concentration for the FCS measurements is then the concentration from where UV-Vis spectroscopy starts to lose sensitivity. Thus the two techniques, UV-Visible and fluorescence correlation spectroscopy (FCS), were compared in respect of concentration measurements and the sensitivity of the two techniques are demonstrated.

For the red laser (633 nm), Alexa 647 fluorophore is used. It has absorbance maxima at 647 nm. The characterization of the correlation function for the blue laser (488 nm) is done using Rhodamine B which has absorbance maxima at 554 nm.

In FCS, each measurement is the average of 5 sets of measurements over 10 seconds and these measurements are carried out at least 6 times for each concentration in order to confirm the stability of the solution over time and to calculate an average of the concentrations. The data are then processed by Igor Pro software and fitted with the correlation function $G(\tau)$. The fit curve provides information on the values of the molecule number, N , the diffusion time, τ , count rate per molecule, CRM, number of molecules in the triplet state, nT and the time in triplet state, tT .

For the experimental part, different Alexa 647 solutions were prepared at concentrations of 250 nM, 100 nM, 50 nM, 25 nM and 10 nM. Characterization of these Alexa 647 solutions by UV-Visible spectroscopy showed maximum absorbance λ_{\max} at 647 nm as shown in **Figure 29**.

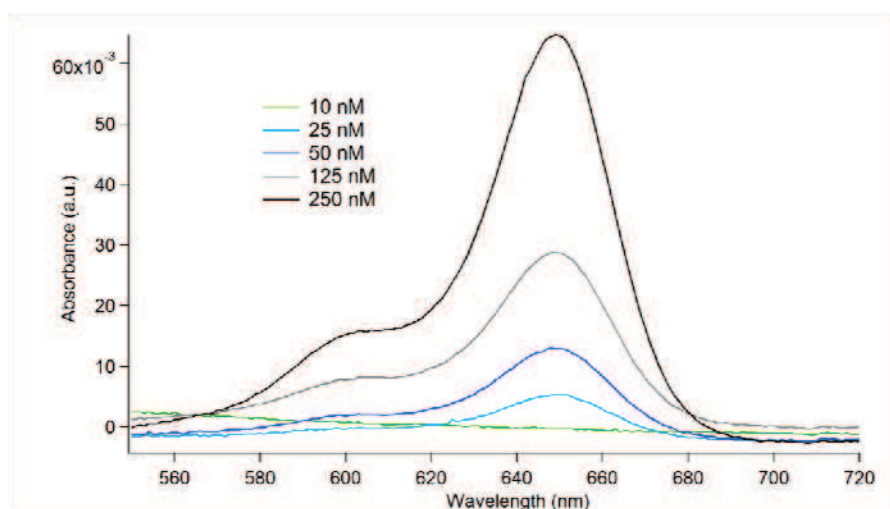


Figure 29. Absorption spectra of the solutions of different concentrations of Alexa 647 obtained by ultraviolet-visible spectroscopy.

It is noticeable from the graph that solutions of less than 20 nM concentrations have no absorption peak at 647 nm. This means that this technique is not sensitive enough to characterize Alexa 647 solution below 20 nM concentration. This is why 10 nM solution showed no absorption maxima.

In order to characterize Alexa 647 by FCS using the red laser, it is important to use solution at molecular concentration low enough (starting from nano molar) because high fluorophores concentration destroys the FCS amplitude. As UV-Visible spectroscopy started to lose sensitivity at 10 nM solution, in FCS we used 10 nM as starting concentration in order to

verify and compare sensitivity of both of the system. The other concentrations used in FCS are: 7.5 nM, 5 nM, 2.5 nM, 1 nM and 0.5 nM.

The cross-correlation results are shown in **Figure 30**.

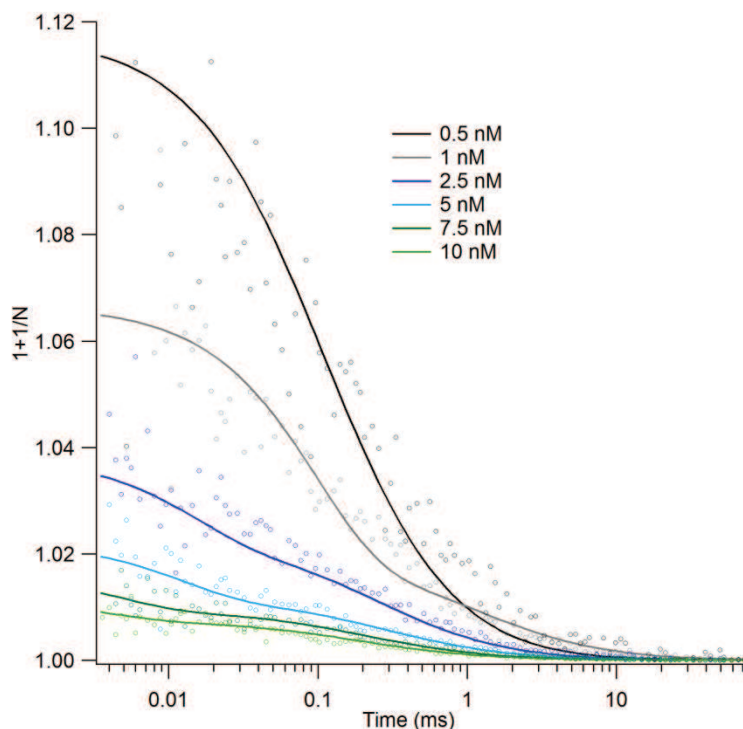


Figure 30. Correlation curves of solutions of different concentrations of Alexa 647 obtained by red laser in FCS.

Figure 30 shows the correlation function of Alexa 647 solutions where it is clear that at nano molar concentration, FCS is very sensitive. It gives even better correlation curve with prominent amplitude below 10 nM concentration. However, the diffusion time τ_d of Alexa solutions is the same as it is an inherent property for all concentrations of the alexa molecule diffusing through the focal volume. With the decreasing concentration, $G(\tau)$ value gets larger, since it is inversely proportional to the molecular number (N). The characterization of blue laser in FCS is performed in the same way using Rhodamine B (**Figure 31**). The FCS is a sensitive technique to the low concentrations solutions with a detection limit of 0.5 nM.

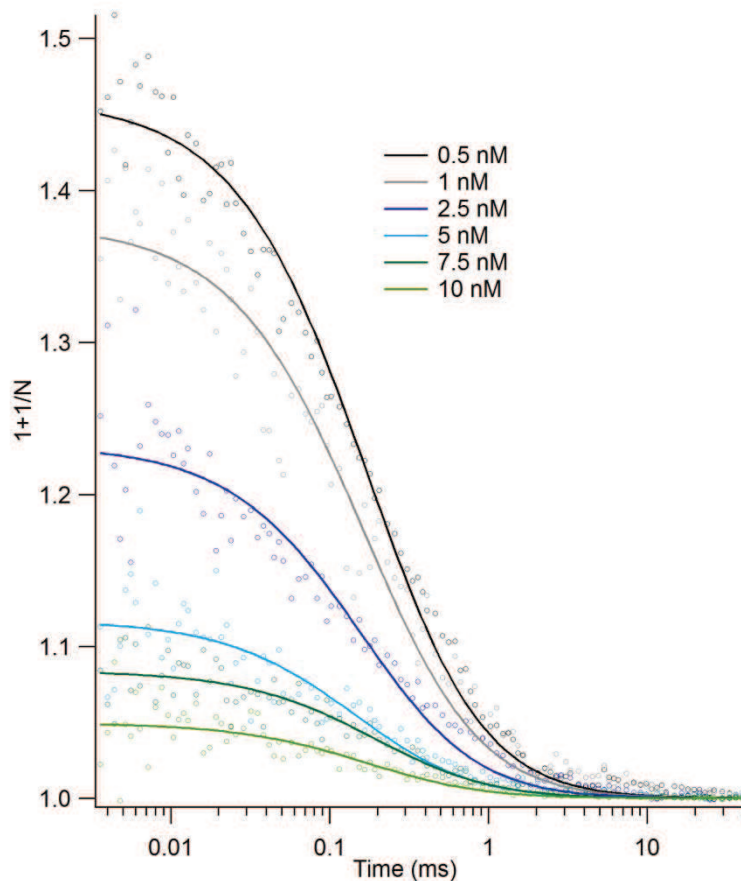


Figure 31. Correlation curves of solutions of different concentrations of Rhodamine B obtained by blue laser in FCS

Table 2. Detected number of molecules (N) and diffusion time (τ) for Alexa 647 and Rhodamine B

Concentration	Alexa 647		Rhodamine B	
	N	τ_D (ms)	N	τ_D (ms)
0.5	8.5 ± 0.9	0.21 ± 0.04	1.2 ± 0.01	0.26 ± 0.01
1	17.3 ± 0.7	0.20 ± 0.01	2.7 ± 0.03	0.25 ± 0.01
2.5	44.6 ± 0.7	0.20 ± 0.02	4.3 ± 0.07	0.24 ± 0.01
5	85.5 ± 1.3	0.20 ± 0.02	8.5 ± 0.2	0.22 ± 0.02
7.5	105.8 ± 2.3	0.19 ± 0.07	12.0 ± 0.2	0.24 ± 0.02
10	134.6 ± 2.7	0.19 ± 0.07	20.0 ± 0.7	0.26 ± 0.03

The values of N determined by FCS are proportional to the theoretical concentrations of the solutions as shown in **Figure 32**.

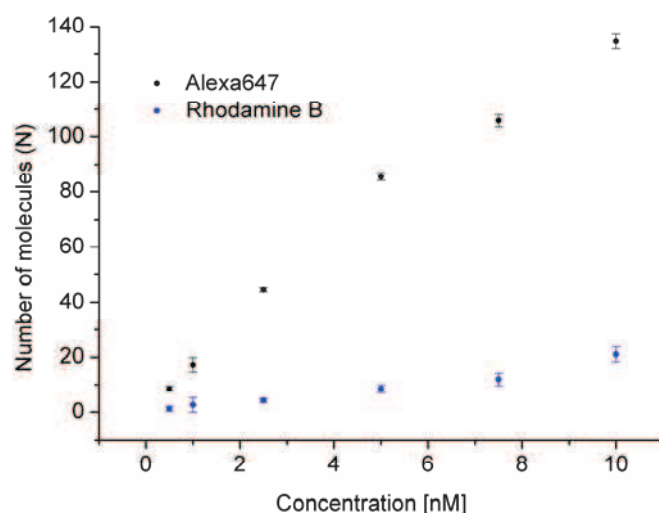


Figure 32. FCS measurement derived fluorophore number N is proportional to the corresponding theoretical concentrations of the molecules Alexa 647 and Rhodamine B

However, the proportionality between the values of N measured by the FCS and theoretical concentrations of Alexa 647 and Rhodamine B prepared proves that FCS using red and blue lasers along with the FCS assembly work successfully.

3.2.3 Photophysical phenomenon during FCS: triplet state evolution

Generally, the fluorescence intensity is assumed to vary linearly with excitation intensity and the concentrations of fluorophores in their singlet ground and excited states are constant over time. However, for higher excitation intensities the rate of excitation is in the same order of magnitude as the rate of excitation of the excited singlet state, but the saturation of the fluorescence and other photo-induced phenomena may occur. Thus the intensity of the excitation laser light should be low, so that the dye emission is in the linear range of its dependence on the excitation (typically a few tens of microwatts). In FCS measurements, the transition to non-fluorescent states creates fluctuations in addition to those due to the diffusion of molecules in the confocal volume. Because of the increased illumination intensities in FCS, incidences of intersystem crossing from the first excited singlet state to the triplet state is enhanced and frequently observed⁶⁸.

The characteristic time of these transitions to or from these photo-induced transient states is generally much smaller than the characteristic diffusion time. At higher intensities the detection volume appears to increase as the emission of the dye molecules in the centre of the

confocal volume saturates and, therefore, the relative contribution of the molecules at the periphery increases.

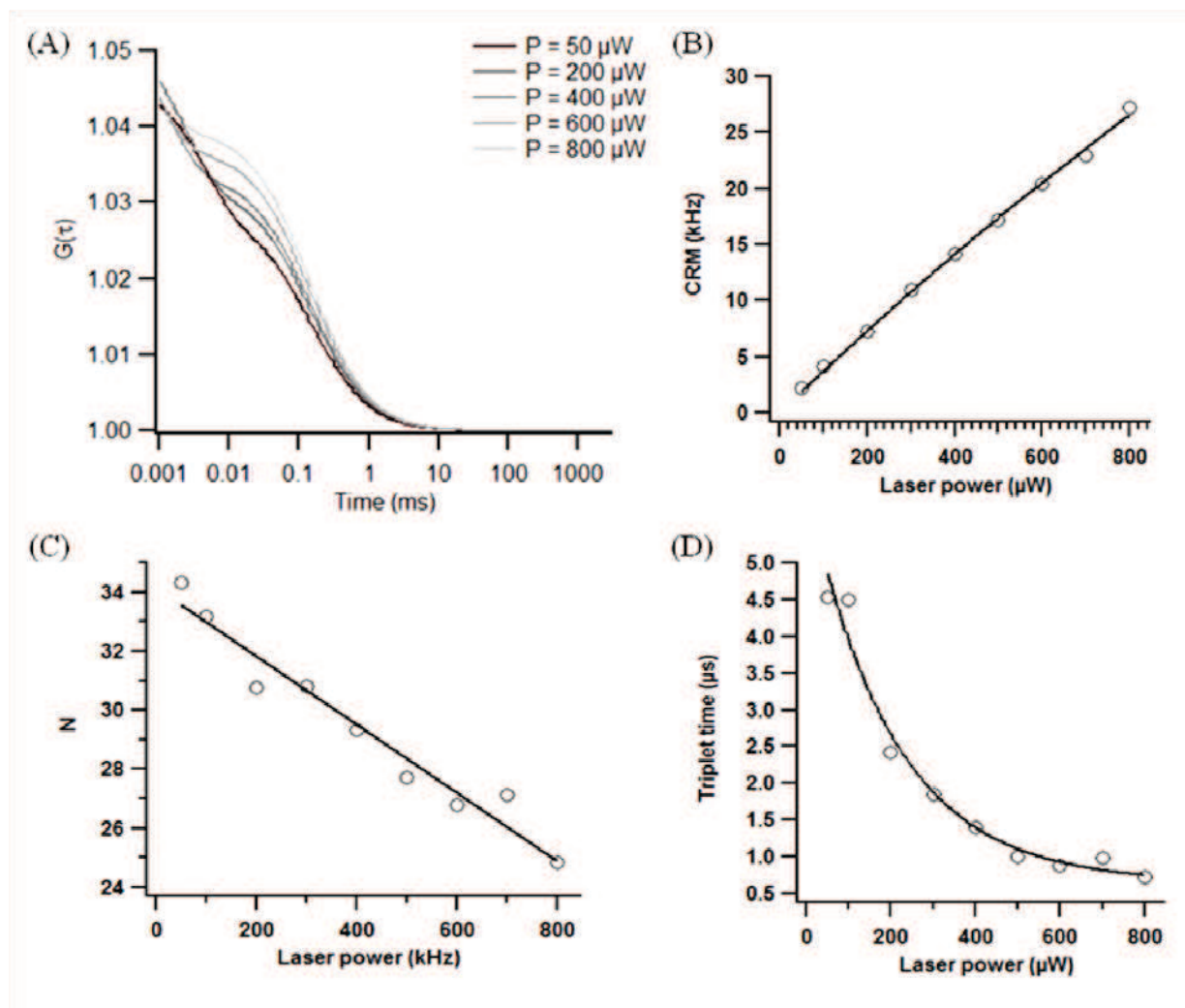


Figure 33. (A) Cross-correlation function of 10 nM Alexa 647 at different laser excitation power and impact of triplet state on it. (B) Counting rate per molecule (CRM), (C) number of fluorescent molecules (N) and (D) triplet time evolution depending on the excitation power.

The experimental cross-correlation functions of 10 nM Alexa 647 are plotted in **Figure 33 A** for different excitation powers. These cross-correlation functions have shoulder at the short time range when the excitation power is increasing. This additional shoulder on the curve corresponds to conversions of the fluorescent molecules towards the non-fluorescent triplet state. In very high laser intensity, as after 500 microwatt laser power, the detector loses its linearity; thus number of fluorophores N in focal volume is underestimated (in **Figure 33 C**). This is why the fraction of molecules in the focal volume is inversely proportional to the excitation power. Hence, the number of fluorescent molecules (N) detected in the observation volume is decreased with the increasing excitation power (**Figure 33 C**), though count rate

per molecule (CRM) is proportional to the excitation intensities (**Figure 33 B**). Interestingly, the diffusion time of triplet starts to decrease and until 800 μW the triplet time decrease exhibits an exponential decay (**Figure 33 D**).

If the reaction is faster than the diffusion time and if there is no change of the diffusion coefficient due to the reaction ⁶⁹, the overall correlation function can be written as

$$G(\tau) = G_D(\tau) \cdot G_T(\tau)$$

Here, $G_D(\tau)$ is the term due to translational diffusion and $G_T(\tau)$ is the term due to the transition to the triplet state. In this case, the correlation function is given by ⁷⁰:

$$G_T(\tau) = G_D(\tau) \left[1 + \frac{\bar{T}}{1 - \bar{T}} \exp(-\tau/\tau_T) \right]$$

Here, \bar{T} is the mean fraction of the fluorescent molecules within the sample volume element being in the triplet states and τ_T is the relaxation time for the singlet–triplet relaxation. This equation accounts for the decrease in the average number of singlet molecules in the observed volume by increasing the amplitude of $\tau = 0$.

In this chapter, we have realised the explanation of the optical set-up and detailed characterization of the FCS system. The results proved that FCS set-up built in our platform gives good performance with a very good optical resolution. The fluorescent molecules used for the characterizations are popular for biological applications. Thus characterizations of the system utilizing these fluorophores can correlate its behaviour during *the in-vivo* biological and medical applications.

Chapter 3

Cytotoxicity of gold nanoparticles

4. Study of cytotoxicity of gold nanoparticles

Summary

4.1 K562 cells

4.2 Materials and Methods

4.2.1 Cell culture

4.2.2 Cytotoxicity of gold nanoparticles in K562 cells

4.3 Result and discussion

4.4 Journal article attached: GNPs toxicity on HUVEC cells

This chapter describes the study of cytotoxicity assessment and cell-GNPs interaction with HUVEC and K562 human cells. In the first part of this study, we have employed a multiparametric approach to evaluate the cytotoxicity of GNPs on human adherent endothelial HUVEC cells. Our study includes two shapes of GNPs: gold nanoflowers (GNFs) and gold nanospheres (GNSs). We report the effect of 15 nm and 50 nm GNSs and 50 nm GNFs with different surface chemistries (citrate, ascorbate and PEG) on HUVEC cells. We have used six different gold nanoparticle samples: 15 nm gold sphere as prepared (a-15-GNS), 15 nm gold sphere PEG coated (PEG-15-GNS), 50 nm gold sphere as prepared (a-50-GNS), 50 nm gold sphere PEG coated (PEG-50-GNS), 50 nm gold flowers as prepared (a-GNF) and 50 nm gold flowers PEG coated (PEG-GNF). Despite the wide acceptance of 50 nm PEG-GNPs as a suitable biocompatible particles for biomedical application^{37, 38}, no study has been reported comparing the toxicity of GNSs and GNFs of same size in the same experimental conditions. For this reason we decided to study the cytotoxicity of different gold nanoparticles on HUVEC cells, using a detailed approach analyzing the following points: cell viability, cell morphology and proliferation rate. The results of cytotoxicity assessments on HUVEC cell were reported in a publish paper. The manuscript in its original form is included at the end of this chapter, where all the significant results and discussion of HUVEC-GNPs interaction study is elaborated.

For better understanding of nanotoxicity on cells, we decide to compare cytotoxicity studies in HUVEC cells with the cytotoxicity in K562 cells. K562, are a leukemia cancer cell. Thus, we have studied the proliferation of K562 cells in the presence of six different GNP. Other interaction studies like cell viability or effect on the function of K562 cell organelles have not been studied yet. Still this proliferation study on both types of cells gave us the opportunity to compare the preliminary effect on both two different cell lines, which is very important to forward with the further interaction studies of cell-GNPs.

4.1 K562 cells

The K562 cell line is a highly undifferentiated erythroleukemia originally derived from a patient with chronic myelogenous leukemia⁷¹. In this study were used K562 leukemia cells and the P-glycoprotein (P-gp) over expressing K562/ADR cells. P-gp* with molecular mass of 170,000 Da, is responsible for the active efflux of molecules outside the cells.

In the context of chemotherapy, cellular retention strongly influences drug's cytotoxicity, and the level of intracellular drug content is a function of the amount of drug transported into the cell (influx) and the amount of drug expelled from it (efflux) by P-gp. This functional principle concerning drug cytotoxicity can be applies to the behavior of GNPs in cytotoxicity studies. If GNPs are a substrate of P-gp we can expect to see a difference of the toxicity between K562 and K562/ADR cells. The kinetics of the accumulation of GNPs should be different in this two cellular models and cytotoxicity should decrease in K65/ADR cells if GNPs is transported by P-gp. Thus we compared the viability profiles between K562 and K562/ADR were studied when both type of cells were incubated with six different GNPs.

*[*P-gp: The P-gp is a membrane glycoprotein of 170 kDa, consituted of 1280 amino acids. It includes 12 transmembrane domaines with two ATP binding domains on the site of cytoplasm⁷². The P-gp possesses three sites of glycosylation on the site of the first extracellular loop near the N-terminal⁷³. In humans, P-gp is encoded by the MDR1 gene, located on chromosome 7, and in mice by the MDR1 gene (a/b). P-gp is present in several human organs such as liver, kidneys, intestines, adrenal glands and also at the level of blood-tissue barriers like the placenta, capillaries of the testes and brain capillaries. It is localized to the apical membrane of cells (hepatocytes, epithelial cells of the intestinal mucous, endothelial cells of the BHE)⁷⁴.*

1/ P-gp plays important role in the protection of tissues against the toxic agents, in fact it allows the excretion of toxic substances by billiary secretion and glomerulour filtration.

2/ It also plays role in the secretion of steroid hormones⁷⁵

3/ But P-gp also has a pathological role in being responsible for multiple resistance to anti-tumor drugs. Acute treatment (or extended) of human cell lines with anti-tumor drug, in vitro, produces an induction of P-gp. This was explained by the fact that the MDR1 promoter responds directly to cytotoxic agents.

The spectrum of susbtrates of P-gp is very wide without any apparent relation with the structure or the function. Among the substrates of the P-gp, some are: i) the classic anti-tumor drug such as anthracyclines, vinca-alcaloids, taxanes ; ii) the antibiotics like erythromycines and tetracyclines ; iii) endogenous substrates like

steroids, cytokines and bilirubions. Furthermore, inhibitors of P-gp like verapamil, are also substrates of this transporter ⁷⁵.]

4.2 Materials and Methods

4.2.1 Cell culture

The K562 cell line is a highly undifferentiated erythroleukemia originally derived from a patient with chronic myelogenous leukemia (Lozzio and Lozzio 1975). K562 leukemia cells and the P-glycoprotein overexpressing K562/ADR cells, were cultured in RPMI 1640 medium with GlutaMAXTMI (GIBCO) medium supplemented with 10% fetal calf serum (GIBCO) at 37°C in a humidified incubator with 5% CO₂. The over-expressing P-gp cell line, K562/ADR, was cultured with 400 nM Doxorubicin, until 4 weeks before experiments. K562 cultures were initiated at a density of 10⁵ cells/mL grew exponentially to about 10⁶ cells/mL in 3 days. In order to have enough cells in the exponential phase for assay, cultures were initiated at 5 x 10⁵ cells/mL and allowed to grow for 24 h until use. All cultured cells were counted with a Coulter counter before use.

4.2.2 Cytotoxicity of gold nanoparticles in K562 cells

Stocks of GNPs were diluted using cell culture medium containing fetal bovine serum to have different treatment concentrations. 10 000 cells/well were seeded in a 96-well tissue culture plate and cultured in RPMI 1640 GlutaMAXTM-I (GIBCO) medium supplemented with 10 % fetal calf serum and mixed with appropriate volume of each GNP samples of desired concentration to a final volume of 200 µL/well. The cells and GNPs were incubated for 24 h at 37°C in a humidified incubator with 5% CO₂ and then the cell viability assay was done. Control cells were used without GNP treatment. At the end of period of incubation, the cytotoxicity of GNPs was assessed by counting the number of cells using a Coulter counter which is a device for counting individual cells.

Each experiment was performed in triplicates for each concentration of every sample and repeated 3 times on different passage number on different days in the same conditions of incubation. The average of all of the experiments has been shown as cell-growth percentage in comparison with the control experiment (cells without GNPs). GNPs untreated cells were considered as 100 % growth.

A Coulter counter has microchannels through which fluids containing particles or cells are drawn and then each cell causes a brief change to the electrical resistance of the liquid. This

change in electrical impedance is proportional to the volume of the particle traversing through. The counter detects these changes in electrical resistance. Thus based on the size range of live and dead cells, the coulter counter counts total number of live cells passed through the microchannel and displays the result of total live cell among total cells passed through ⁷⁶.

4.3 Results and discussion

The GNPs concentration used were ranged between 1 pM and 10 pM. After 24 h of incubation, cell growth was estimated using the Coulter counter. *Figure 34* shows the result of cellular growth plotted against concentrations of both a-GNPs (as-prepared GNPs) and PEG-GNPs (PEG coated GNPs). K562/S and K562/ADR cells show slightly different response due to the GNPs incubation. The cytotoxicity of 15-GNS on K562/S cells occur at 10 pM concentration and the growth is 80% while on K562/ADR 70% was observed at 1 pM concentration (*Figure 34 a & b*). In the case of 50-GNS, no growth cell decrease was observed on K562/S cells but the decreasing of growing started at 0.5 pM in case of K562/ADR cells and it remained constantly at 80% until 10 pM (*Figure 34 c & d*). Lower cytotoxicity was observed for 50-GNS than 15-GNS and whenever any cell concentration changing occurred, a-GNPs had little lower value of growing than PEG-GNPs. The dependence of this toxicity on concentration is related to the surface chemistry of GNPs as GNPs with PEGylated surface (surface charge close to zero) can induce lower cellular internalization efficiency for both sizes. On the other hand, smaller NPs have higher possibility to interact with the cell organelles due to an increase of their surface to volume ratio ⁴⁷.

The toxic concentration range for GNPs was found to be widely below that one's observed for GNSs and a-GNPs effect is more evident than the PEG-GNPs (*Figure 34 c & d*). Due to a-GNPs incubation, cellular growth became almost 85% at 0.001 pM or 1 fM and it decreased exponentially until 1 pM where the value is 50% (*Figure 34 e*). In case of PEG-GNPs these values were at least 25% to 30% higher than a-GNPs. On K562/ADR cells, the decrease on cell growing starts from 0.5 pM (80%) and at 1 pM the cell growth was 40% for a-GNPs and 50% for PEG-GNPs (*Figure 34 f*). This cell growth cell is two orders of magnitude lower than the one observed for GNSs having the same size.

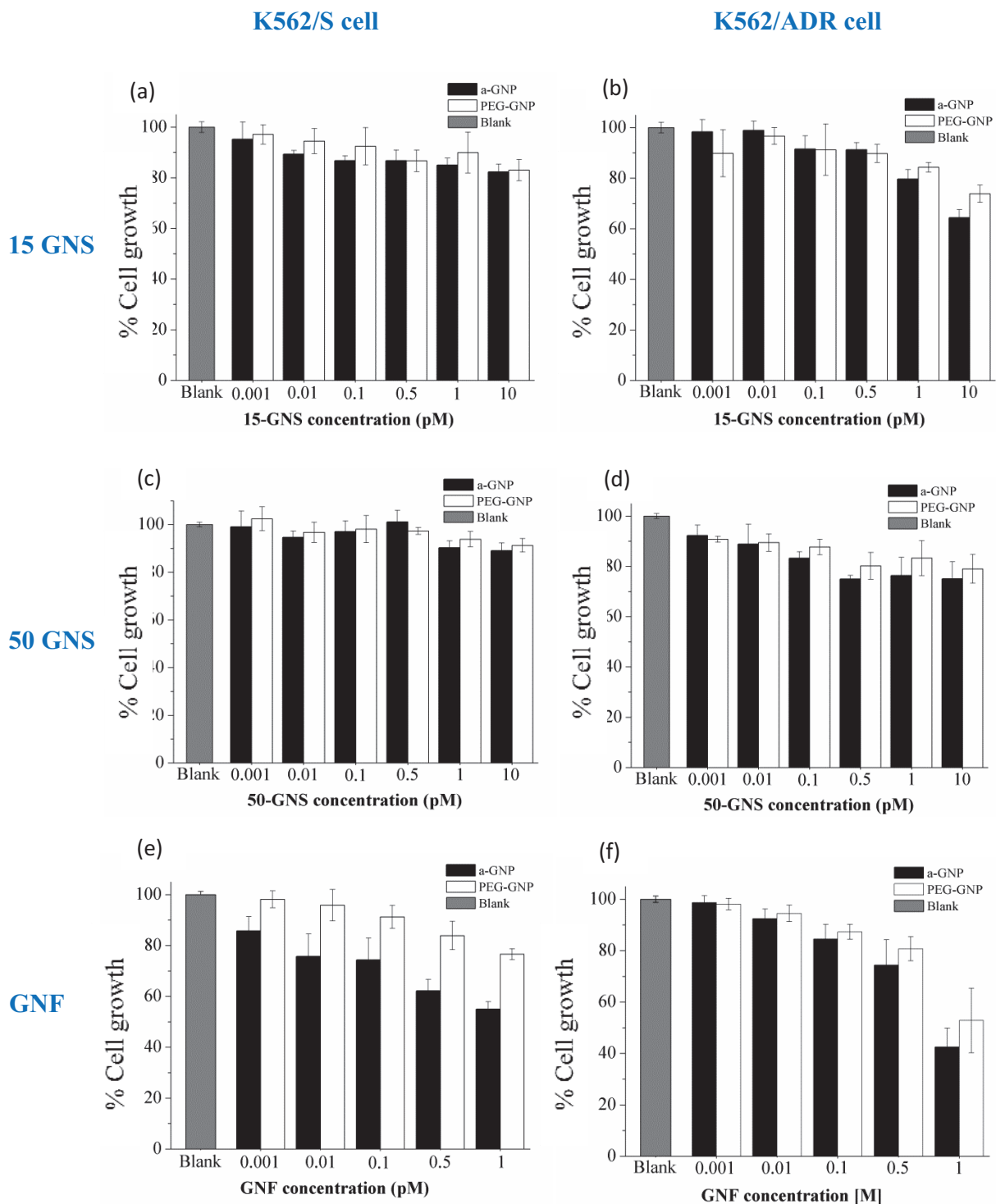


Figure 34. Toxicity of GNPs in K562 cells (left column) and K562/ADR cells (right column) incubated for 24 h with different concentrations of a-GNPs, PEG-GNPs and GNF: (a-b) 15-GNS, (c-d) 50-GNS and (e-f) GNF. Data are expressed as mean \pm standard deviation ($n = 9$).

One can notice that the GNPs have a largely higher growth inhibition effect than the GNSs. The PEGylation of the surface of each type of GNPs enhances the biocompatibility up to 30%. GNSs size also shows comparative toxic effect where 15 nm GNSs are little more

deleterious than 50 nm GNSs on K562 cells, especially when used without PEGylation. The GNPs used in this study were washed and centrifuged several times in order to remove any trace of contaminants that may arrive during sample preparation and handling or remaining reductant agent from the reaction that may interfere with the assay, thus there is no possibility of induction of toxicity due to remaining surfactant or gold salts in the solution (see Method section).

Now if we compare the GNPs toxicity between HUVEC cells (mentioned in the article in this chapter) and K562 cells, we observe that at 10 pM 15-a-GNS have the same effect on K562/S and HUVEC, however K562/ADR have 10% more cell death. 50-a-GNS showed no effect on K562/S cells while on K562/ADR cells there was 10% more cell death than HUVEC cells (75% and 85% cell growth). Both 15 and 50 nm PEG-GNS had no toxic effect on HUVEC cells at 10 pM concentration. a-GNFs started to show toxicity on K562/S from 1 fM (82% cell growth) and exponentially decreased until 1 pM where the cell growth is around 58% though PEG-GNFs always had at least 20% more cells at all experimental concentrations. On both K562/S and HUVEC cells, GNPs have similar effects. Until 0.5 pM, significant cell death was not observed (80% cells), but at 1 pM the decrease was until 50%-60% for HUVEC cells and 40%-50% for K562/ADR cells. Finally it can be concluded that GNPs seem to be more toxic for K562 cells than HUVEC cells. GNSs don't show more toxicity to K562 cells than HUVEC cells. This proves the potentiality of flower shaped GNPs on cancer therapy. This result is interesting and points out that the surface chemistry is a critical parameter in the biocompatibility of the GNPs. One can also conclude that during future therapeutic applications of GNPs, PEG-GNSs can be used at 100 times more concentrated dose than the GNPs. However, the differences obtained in both cell types could be due to the experimental methods used for each cell line.

4.4 Journal article attached: GNPs toxicity on HUVEC cells

All the results concerning the cytotoxicity of GNPs on HUVEC cells are described in the following manuscript:

Comparative toxicity evaluation of flower-shaped and spherical gold nanoparticles on human endothelial cells

Sadequa Sultana¹, Nadia Djaker¹, Sanda Boca-Farcau², Milena Salerno¹,
Nathalie Charnaux³, Simion Astilean², Hanna Hlawaty³ and
Marc Lamy de la Chapelle¹

¹ Université Paris 13, Sorbonne Paris Cité, UFR SMBH, Laboratoire CSPBAT, CNRS (UMR 7244), 74 rue Marcel Cachin, F-93017 Bobigny, France

² Babes-Bolyai University, Institute for Interdisciplinary Research in Bio-Nanosciences and Faculty of Physics, Nanobiophotonics and Laser Microspectroscopy Center, 1 Str. M Kogalniceanu, RO-400084 Cluj-Napoca, Romania

³ Université Paris 13, Sorbonne Paris Cité, UFR SMBH, INSERM U1148, Laboratory for Vascular Translational Science, Bio-ingénierie cardio-vasculaire, 74 rue Marcel Cachin, F-93017 Bobigny, France

E-mail: nadia.djaker@univ-paris13.fr

Received 26 September 2014, revised 18 November 2014

Accepted for publication 8 December 2014

Published 9 January 2015



CrossMark

Abstract

In this paper, we propose a multi-parametric *in vitro* study of the cytotoxicity of gold nanoparticles (GNPs) on human endothelial cell (HUVEC). The cytotoxicity is evaluated by incubating cells with six different GNP types which have two different morphologies: spherical and flower-shaped, two sizes (~15 and ~50 nm diameter) and two surface chemistries (as prepared form and PEGylated form). Our results showed that by increasing the concentration of GNPs the cell viability decreases with a toxic concentration threshold of 10 pM for spherical GNPs and of 1 pM for flower-shaped GNPs. Dark field images, flow cytometry and spreading test revealed that flower-shaped GNPs have more deleterious effects on the cell mechanisms than spherical GNPs. We demonstrated that the main parameter in the evaluation of the GNPs toxicity is the GNPs roughness and that this effect is independent on the surface chemistry. We assume that this behavior is highly related to the efficiency of the GNPs internalization within the cells and that this effect is enhanced due to the specific geometry of the flower-shaped GNPs.

Keywords: nanoparticles, biocompatibility, nanotoxicology, surface chemistry, cell proliferation, actin cytoskeleton, cell spreading

(Some figures may appear in colour only in the online journal)

1. Introduction

Gold nanoparticles (GNPs) are of great interest for several applications in nanomedicine, especially in imaging and sensing [1], drug delivery [2, 3] and photothermal therapy [4, 5] because of their unique physical and chemical properties, and high biocompatibility. Among different morphologies of GNPs, gold nanospheres (GNSs) are widely used for biomedical applications [6, 7]. In recent years, gold nano flowers (GNFs) (also termed as urchin like, branched particles or stars) have been proposed to improve the light-matter

interaction and thus the optical properties of such nanostructures which is essential for photothermal therapeutics [8, 9] or optical cellular imaging [10–12]; thanks to their tips which are responsible to a higher local electromagnetic field enhancement [13]. For all these applications, a better understanding of the interaction and uptake of GNPs into cells is of great importance and currently under intense investigation [14–17], especially for GNFs who exhibit improved optical properties. In this latter case, it is then of first importance to determine if this higher efficiency is suitable with an acceptable biocompatibility.

Several groups have identified the size of GNPs as the first variable in their interaction with cells [18–20]. Chithrani *et al* reported the effect of GNP size on the cellular uptake with sizes varying between 14 and 100 nm [21]. GNPs larger than 10 nm in diameter internalized inside cells were trapped in vesicles in the cytoplasm and did not enter in the nucleus [18, 21]. Pan *et al* suggested that the uptake of GNPs is mediated by non-specific adsorption of proteins onto the gold surface, which induces internalization into cells via the endocytosis mechanism [19, 20].

Many reported works showed that GNPs size and aggregation can affect cell adhesion and proliferation: Cui *et al* showed that small GNSs (2 nm), which are more stable against aggregation, caused less HeLa cytotoxicity than larger GNSs (25 nm) which are liable to form aggregates [22]. Arvizo *et al* studied the effect of GNP size on inhibition of endothelial and fibroblast cell proliferation. It was demonstrated that 20 nm GNSs showed a maximal inhibition of cell proliferation up to 100% whereas 10 nm showed up to 60% and 5 nm up to 25% of inhibition [23]. In the same way, Pernodet *et al* reported that 14 nm GNSs had a significant uptake into dermal fibroblasts [24]. It was suggested that the presence of GNPs is responsible for abnormal actin filaments and extracellular matrix constructs in dermal fibroblasts; which decrease cell proliferation, adhesion, and motility. Jiang *et al* proposed that GNPs can not only passively interact with cells, but also at a specific size actively alter the molecular processes that are essential for regulating the cell functions [25]. GNPs of 40–50 nm are found to be the optimal sizes for receptor-mediated endocytosis. This higher particle uptake is probably due to the direct balance between multivalent cross linking of membrane receptors and the process of membrane wrapping involved in receptor-mediated endocytosis.

Nanoparticle size is not the only relevant parameter in the GNPs–cell interaction. The cell membrane seems to be also very sensitive to the GNP's surface chemistry. By considering only the surface chemistry, Goodman *et al* found that cationic particles are moderately toxic, whereas anionic particles are rather less toxic [18, 26]. Freese *et al* have discussed different polymer coatings and concluded that the positive-charge coated GNPs were internalized to a greater extent than the negative- or neutral-charged GNPs, as would be expected due to interactions with the anionic cell membrane [27]. Arnida *et al* showed that GNPs appeared to be taken up by non-specific adsorptive endocytosis [28]. PEGylation (PEG=poly ethylene glycol) on the surface of GNPs drastically reduced this uptake. In the literature, the most reported chemical modification related to reduction of toxicity, is the addition of PEG on the surface of GNPs (PEG-GNPs) [29]. For example, internalization of GNSs was surface chemistry dependent as CTAB-coated spheres were readily internalized than PEGylated spheres during same incubation experiment [30]. Sironi *et al* showed that the PEGylation of the GNPs hinders their internalization and increases their resistance to aggregation in the culture medium [31]. GNPs were observed very cytotoxic on epithelial cells under a picomolar (pM) concentration

where concentration dependent effect was comprehensible [12].

These results highlighted that the cellular interaction with GNPs have to be analyze with respect to various parameters of GNPs besides size, shape and surface chemistry as well as to GNP concentration and cell culture properties (cell line, incubation time). It is then of first importance to provide multi-parametric study to cover all the possibilities of cell–GNPs interactions and to screen various ways of interactions using standard toxicity assays.

In this study, we have employed such approach to evaluate the cellular uptake and cytotoxicity of GNPs in adherent human endothelial cells (HUVEC). Our study includes in total six different types of GNPs which have two morphologies: spherical (~15 and ~50 nm diameter termed as: 15-a-GNS and 50-a-GNS) and flower-shaped (only ~50 nm diameter termed as: a-GNF); and two surface chemistries- as prepared form and after polymer stabilization by polyethylene glycol which were termed as: 15-PEG-GNP, 50-PEG-GNP, PEG-GNF.

The choice of nanoparticles is all the more favored since no study has already been reported comparing the cytotoxicity of GNSs and GNPs of same size in the same experimental conditions. Moreover, to answer the question of cytotoxicity, a detailed approach is analyzed through the following points: cell viability, morphology and proliferation rate. With such approach, we are able to provide a complete study of the influence of the size, shape and surface chemistry effect on the GNPs interaction with cells and on their potential toxicity. We will also be able to propose a cellular mechanism to explain the effect of the GNPs on the cell viability and on the cell behavior.

The choice of HUVEC as cell model system for this study is based on the cell's physiological function and priority during theranostics involving GNPs because of their adherent phenotype. Principal function of adherent endothelial cells is to construct the vascular wall in presence of smooth muscle cells and fibroblasts. Endothelial cells form the continuous monolayer which is in permanent contact with the blood flow. For the purpose of diagnosis and therapeutic applications, GNPs are frequently administered by intravascular injection and distributed by the vascular circulation in whole body. Endothelial cells are one of the first cell-types which interact directly with the GNPs after their intravascular administration *in vivo* [15] and can be rapidly affected because of cytotoxicity of injected GNPs.

2. Materials and methods

2.1. Synthesis, surface modification and characterization of GNPs

GNPs were prepared by the rapid mixture of 20 mL solution of 19.8×10^{-3} M of ascorbic acid with 200 μ l of 10^{-2} M of HAuCl₄ at ice temperature [12]. Colloidal GNSs of 15 nm were synthesized by the aqueous reduction of HAuCl₄ with trisodium citrate according to the Turkevich–Frens method.

Briefly, an amount of 100 mL of 10^{-3} M $\text{HAuCl}_4 \cdot 3\text{H}_2\text{O}$ was boiled. A solution of 38.8×10^{-3} M sodium citrate (10 mL) was quickly added under vigorous stirring until a red burgundy colloidal solution was formed [32]. Colloidal GNSs of 50 nm were produced by stirring 10 mL of a solution of 0.5×10^{-3} M HAuCl_4 at room temperature for several minutes, followed by the addition of a proper volume of a freshly prepared ascorbic acid (7.5×10^{-3} M) solution. Herein, $\text{HAuCl}_4 \cdot 3\text{H}_2\text{O}$ has a role of nanoparticle initiator while L-ascorbic acid is used as reducer of the gold salt.

One batch of each type of GNPs was modified using mPEG-SH polymer of 5 kDa molecular weight, that provided more stability to the particles. Depending on the nanoparticle type and hence on its surface area, various amounts of 10^{-3} M polymeric solution were added to the colloidal solution by dripping. The polymer-nanoparticle mixtures were subjected to vigorous stirring after which let to sit for 24 h at 4°C to afford a complete binding of the polymer. Both as-prepared and polymer stabilized GNPs (a-GNPs and PEG-GNPs, respectively) were purified by centrifugation at high speed and resuspended in ultrapure water until the incubation with cells. For each *in vitro* assay, GNPs stock solution was dissolved in the corresponding cellular medium containing serum protein.

To determine GNPs concentration in colloidal solution, optical extinction spectra were measured using a UV-vis spectrometer (Kontron Instr. France) on a spectral range from 400 to 900 nm. The wavelength of extinction maxima was used to calculate stock concentration using extinction coefficient. The size and the zeta potential measurements of the colloidal GNPs were performed using a Zetasizer Nano-ZS90 instrument from Malvern.

2.2. Cell culture

Human umbilical vein endothelial cells (HUVEC, N CRL-1730, ATCC, LGC Molsheim, France) were cultured in endothelial cell basal media 2 (ECBM2, PromoCell, Germany) supplemented with 10% fetal bovine serum, epidermal growth factor (EGF, 5.0 ng mL^{-1}), hydrocortisone ($0.2 \mu\text{g mL}^{-1}$), VEGF (0.5 ng mL^{-1}), basic fibroblast factor (bFF, 10 ng mL^{-1}), insulin like growth factor (R3IGF-1, 20 ng mL^{-1}), ascorbic acid ($1 \mu\text{g mL}^{-1}$), heparin ($22.5 \mu\text{g mL}^{-1}$), antibiotics (penicillin-streptomycin, 1, Invitrogen, France) and L-glutamine (1, Invitrogen, France) at 37°C . in 5% CO_2 . The media was changed twice a week. The cell line was purchased as passage number 20 and characterized by ATCC before selling. The homogeneity is guaranteed until 50–60 population doublings (life expectancy).

2.3. MTT assay

Actively growing cells were seeded at a density of 10 000 cells/well of a 96-well tissue culture plate using ECBM2 media containing 10% fetal bovine serum and incubated 24 h to have adherent and proliferating cells. GNPs with both surface chemistries were diluted by cell culture medium

containing fetal bovine serum to have different treatment concentrations (10^{-15} – 10^{-10} M). The cells were treated and incubated with varying concentrations of all six types of GNPs at culture condition for 24 h. Control cells were used without GNPs treatment. At the end of each exposure, the toxicity level of GNPs was assessed by MTT assay where MTT dye ((3-(4,5-dimethylthiazol-2-yl)-2,5-diphenyl tetrazolium bromide), Daco, France) reduces only metabolically active cells to insoluble purple formazan dye crystals. The intensity of the purple formazan was measured directly in the wells at 595 nm using microplate reader. Each experiment was performed in triplets for each concentration of every sample and repeated three times on different passage number on different days ($n=3$) occupying the same duration for incubation. The average of all of the experiments has been shown as cell-viability percentage in comparison with the control experiment, while gold untreated controls were considered as 100% viable.

2.4. Flow cytometry analysis to determine cell proliferation rate

HUVEC were seeded at a density of 75 000 cells/well in the 12 well plate using ECBM2 media containing 10% fetal bovine serum for 24 h to make the cells adherent and proliferating. Then the media was replaced with serum free ECBM2 media and the cells were synchronized for another 24 h. Then the cells were incubated with 10 pM of 15 and 50 nm GNSs whereas 0.5 pM for GNPs for 24 and 48 h in ECBM2 media containing 10% fetal bovine serum. The labeling of the cells was done by CellTrace Violet Cell Proliferation Kit (Invitrogen, Molecular Probes, France; fluorescence excitation/emission maxima 405/450 nm) and quantified by immune fluorescence on a FACSCalibur flow cytometer (BD Biosciences).

2.5. Dark field imaging

The dark field imaging of HUVEC was done using an inverted Microscope (Axio Observer.Z1-Zeiss, Germany) after incubation with 0.5 pM of each type of GNPs which were diluted in cell culture media containing serum. Cells were grown in the LabTek at 75 000 cells/well concentration and grown overnight in presence of ECBM2 media supplemented with 10% fetal bovine serum. Following morning, cells were inoculated in presence of GNPs. After 3 h of incubation at cell growth condition, cells were washed by PBS (1X), fixed with PFA 1% for 30 min and imaged by a dark field condenser where a 20 \times objective collects the scattered light from the internalized particles.

2.6. Spreading test

Spreading of HUVEC was carried out in respective supplemented basal cell culture media. 6500 cells/well seeded were allowed to spread overnight on fibronectin (BD Bioscience Pharmingen, France) coated glass LabTek as a sub-confluent culture in order to analyze changes in individual cell shape and size. After one wash with PBS (1X); 0.5 pM of each type of GNPs dissolved in serum containing culture media were

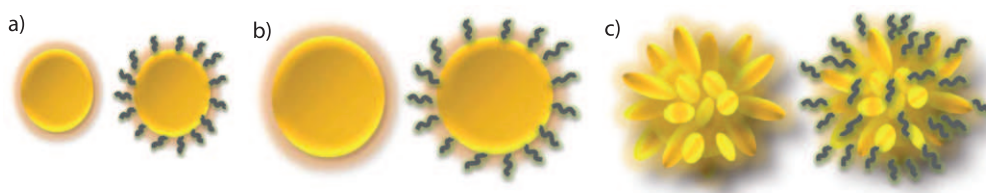


Figure 1. Schematic illustration of GNPs with as prepared and PEG coated surfaces, (a) 15-a-GNS (left) and 15-PEG-GNS (right), (b) 50-a-GNS (left) and 50-PEG-GNS (right) and (c) a-GNF (left) and PEG-GNF (right).

added to the cell culture and incubated for 3 h at 37 °C in 5% CO₂. Cells were fixed using PFA 1% and washed by PBS (1X); followed by permeabilization using 0.05% of Triton X-100 solution (Sigma-Aldrich, France). Cytoskeleton (F-actin) and nucleus were stained subsequently with Alexa Fluor 546 phalloidin (dilution 1/200, Invitrogen, France) and DAPI (dilution 1/1000, Invitrogen, France); and observed with a fluorescence microscope (Zeiss Axiophot, Carl Zeiss France). Cells were photographed using digital camera fixed on top of the microscope (Nikon COOL PIX 8400, Japan) and images were treated by Adobe Photoshop software to trace the edge of individual cell. Then the area enclosed by each trace was measured using Scion Image software (Scion Corporation). Each data point represents an average of at least 100 individual measurements of the cell surface area.

2.7. Statistical analysis

All data are expressed as mean \pm standard deviation (SD) unless indicated otherwise and analyzed using one-way analysis of variance (ANOVA). In all cases, the degree of significance is indicated when appropriate (* $p < 0.05$; ** $p < 0.01$; *** $p < 0.001$).

3. Results and discussion

3.1. GNP characterization

In the present work, we synthesized a series of GNPs: GNSs with mean diameters of 15 and 50 nm (15-GNS and 50-GNS respectively) and GNPs with mean diameters of 50 nm (figure 1). The aim of our study is to determine the influence of the size and the shape of the GNPs on the particle toxicity by comparing the results of their interaction with cell. Thus, these two shapes were chosen to observe the effect of the GNPs surface roughness since the surface area and curvatures can play a significant role in their interaction with the cells [12]. To compare GNPs size effect, both 15 and 50 nm GNSs were used. In addition, all GNPs were utilized with two surface chemistries: the ‘as prepared one’ (citrate for 15-a-GNS, ascorbate for 50-a-GNS and a-GNF) and the PEG one (15-PEG-GNS, 50-PEG-GNS and PEG-GNF). The schematic diagram showing shape and size of the synthesized six GNPs is given in figure 1. The primary shape and size for all the nanoparticles were determined by transmission electron microscopy (TEM; JEOL 100 U, 100 kV accelerating voltage) (figures 2(A) and (B)). The TEM images show that the

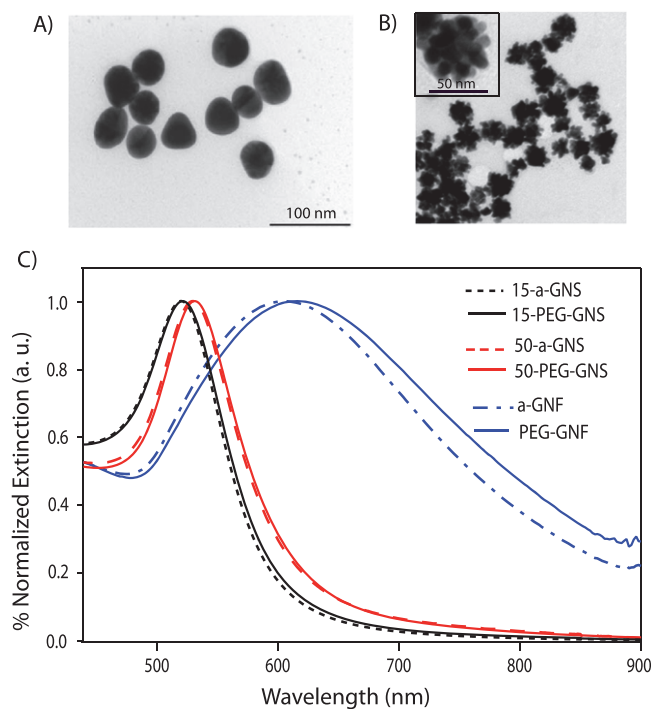


Figure 2. TEM images of (A) 50-a-GNS and (B) a-GNF. (C) Extinction spectra of a-GNPs (dotted lines) and PEG-GNPs (solid lines).

GNSs have a round shape, a smooth surface and a narrow size distribution whereas the GNPs have a large number of tips at the surface (see inset of figure 2(B)). These parameters are confirmed by the Zetasizer measurements that are summarized in table 1. All the prepared a-GNPs have the expected size with a size distribution around 10%. The PEG-GNPs have a larger size due to the PEG layer that enlarges the particle size. These results are consistent with the extinction spectra that give the localized surface plasmon resonance (LSPR, table 1). Indeed, for the 15-a-GNS and the 50-a-GNS, the LSPR positions are 520 and 530 nm respectively which is in agreement with the GNP diameter. In the case of the GNPs, the LSPR is red shifted at 604 nm and is very broad compared to GNSs. This is the result of the particle anisotropy since the GNPs exhibit a large number of tips at the particle surface [12]. For all GNPs, we also observe a red-shift (2 nm for GNSs and 14 nm for GNPs) when the PEG is added. This confirms the exchange of the as prepared surface chemistry by the PEG and that the thickness of the PEG layer is around 5 nm, which is consistent with the size difference measured

Table 1. Physico-chemical characteristics of gold nanoparticles measured by the Zetasizer..

GNP samples	Morphology	Surface chemistry	GNP size (nm) \pm SD	LSPR (nm)	ζ Potential (mV) \pm SD
15-a-GNS	Spherical	Citrate	14.7 \pm 1.9	520	-44.3 \pm 1.9
15-PEG-GNS	Spherical	PEG	20.7 \pm 1.9	522	-3.58 \pm 0.19
50-a-GNS	Spherical	Ascorbate	47.6 \pm 5.2	530	-13.5 \pm 0
50-PEG-GNS	Spherical	PEG	57.5 \pm 5.2	532	-5.1 \pm 0
a-GNF	Flower-shaped	Ascorbate	46.7 \pm 6.5	604	-9.08 \pm 0.8
PEG-GNF	Flower-shaped	PEG	58.1 \pm 6.5	618	-4.65 \pm 0

Note: SD: standard deviation.

with the Zetasizer. The surface ligand exchange was further confirmed by a shift of ζ potential of colloidal nanoparticle measured with the Zetasizer (table 1). We observed ζ potential shift from -44 to -3 mV (93% decrease) in case of 15 GNSs, -13 to -5 mV (62% decrease) for 50 GNSs and from -9 to -4 mV (49% decrease) in case of GNFs. Moreover, in the case of the as prepared GNPs, they are stabilized by their negatively charged surface via electrostatic repulsion, except for the GNFs since the potential is lower than for the GNSs. For all three types of PEG-GNPs, the surface charge was decreased near to neutral zeta potential. This neutrally charged surface is known to provide more stable GNPs with an improved biocompatibility as well as a good distribution of GNPs in biological fluids, a decrease of the non-specific binding of bio molecules to GNPs surfaces, and consequently a decrease of the cellular uptake of PEG-GNPs compared to a-GNPs [33].

Before each experiment, concentration of colloidal solution was calculated based on the surface plasmon resonance band of each material derived from the extinction spectra (see method section). The normalized extinction spectra of the gold colloidal solutions are illustrated in figure 2(C).

This characterization of the colloidal nanoparticles is relevant to the literature of the nanoparticles fabricated using same methods [12, 32].

Furthermore, the colloidal particles were found to be highly stable, as no aggregates could be observed even after three months of storage at room temperature in ultra pure water. Additionally, stability of the GNPs was determined by dissolving the washed pellet in cell culture media with and without serum and in high ionic buffer solution. All GNPs were stable in all those mentioned solutions even until 24 h and did not form large aggregates, except the 15- and 50-a-GNSs which fast aggregated in both solutions due to their highly negative ζ potential. The particle's physicochemical parameters are similar to those commonly used for cell-labeling and therapeutic purposes which make it more interesting to study from toxicological point of view [10, 12].

3.2. Effects of GNPs on cell viability

In this work as a model system for our *in vitro* study, we choose a human endothelial cell (HUVEC) to perform the comparative cytotoxicity study of six different GNPs. The aim of this study is to evaluate the undesirable interactions

of GNPs with normal cells that can occur in the body after their intravascular injection. This endothelial cell line is a good cellular model system to perform the comparative cytotoxicity study of GNPs because of their presence in the vascular artery and permanent contact with blood flow. This is important for the choice of cell line since the therapeutic applications of GNPs are performed usually by intravascular injection.

Viability assays are performed as the starting point in any cytotoxicity assessment and thus the cellular responses to a toxicant can be explained. For the cell viability assessment, a standard colorimetric cellular viability MTT assay was performed to determine the threshold toxic concentration for each type of GNP samples used here. This starting point of toxic concentration is vital to precede with further GNPs interaction studies with cells. The GNPs used in this study have been purified extensively through repeated washing and centrifugation to remove any trace of contaminants or remaining reductant agent from the reaction that may interfere with the assay (see method section).

We limited the testing to 100 pM concentration for four GNS samples and 1 pM concentration for GNf samples as these concentrations are found to be the lowest toxic concentrations. HUVEC were incubated in presence of GNPs for 24 h, and then cellular viability was measured. Figure 3 shows the result of cellular viability plotted against exposure concentrations of both a-GNPs and PEG-GNPs.

The cytotoxicity of 15-a-GNS occurs fast starting from 10 pM concentration and remains consistent from 20 pM until 100 pM. In the case of 50-a-GNS, the cytotoxicity appears only at the highest experimental concentration (100 pM). It is clear that 15-a-GNS induce more cytotoxicity than 50-a-GNS. The dependence of this effect on concentration is highly mediated by the surface chemistry. Low cytotoxicity was observed for the PEG-GNS even at the highest concentration of 100 pM, while 15-a-GNS show only 50% of viability at the highest concentration and 70% of viability is observed with 50-a-GNS (figures 3(A) and (B)). This enhanced cell viability in the case of the PEGylated surface can be due to a lower cellular internalization efficiency for both sizes [33]. Note also that below 1 pM, 100% of cell viability was measured for a-GNS and PEG-GNS (data not shown).

The size effect on cell viability could be assigned to the fact that particles with diameter below 30 nm can be endocytosed easily by the cells [18, 26]. Moreover, smaller NPs have higher possibility to interact with the cell organelles due

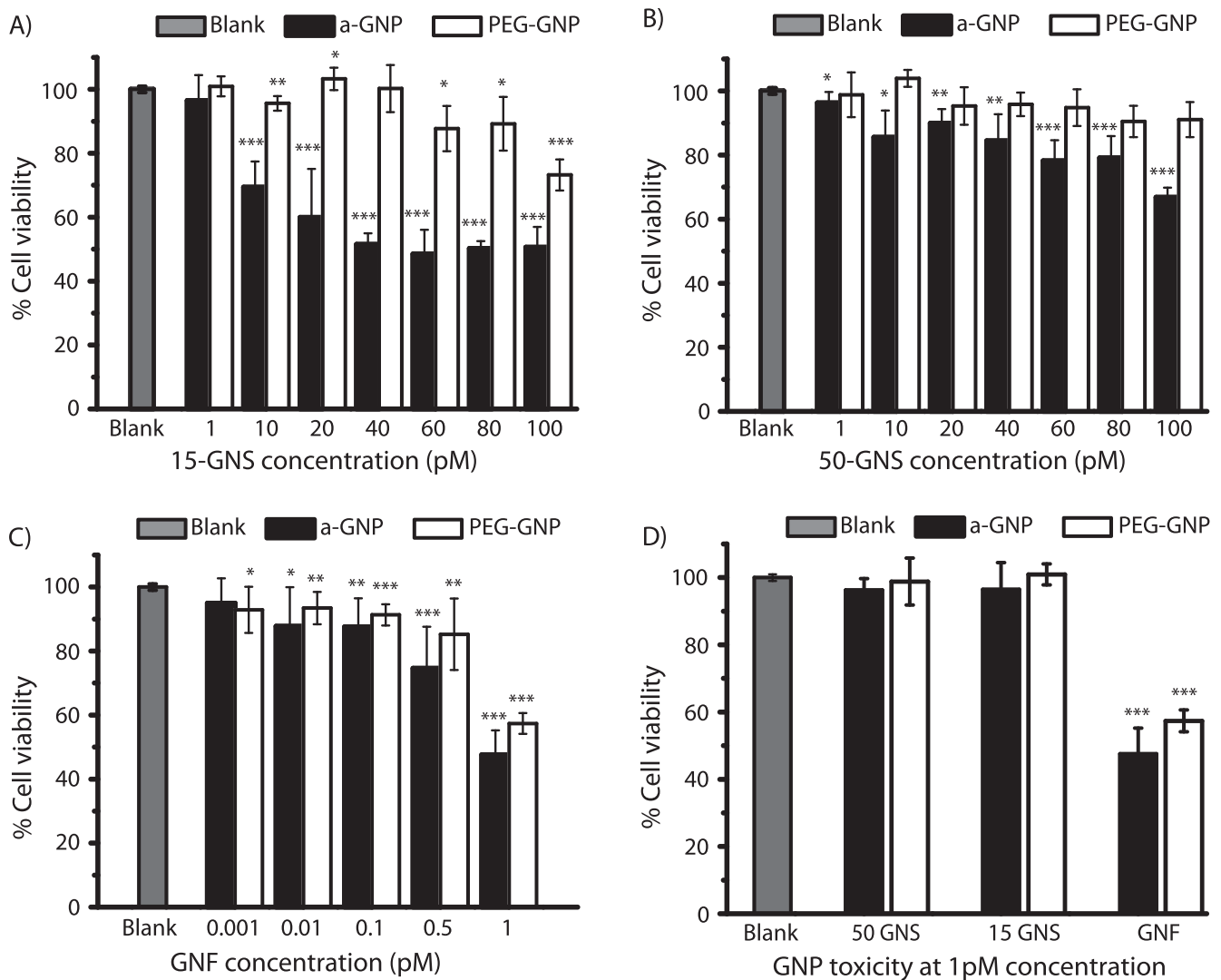


Figure 3. MTT assay results of HUVEC incubated for 24 h with different concentrations of a-GNPs, PEG-GNPs and GNF: (A) 15-GNS, (B) 50-GNS and (C) GNF. (D) A comparative cell viability of different GNPs at the concentration of 1 pM. Data are expressed as mean \pm SD ($n=9$); where * $p<0.05$; ** $p<0.01$; *** $p<0.001$ (ANOVA).

to an increase of their surface to volume ratio [34]. After PEG coating, an improved biocompatibility of all GNSs is observed as expected since surface charges close to 0 (-3 to -5 mV) is reached.

Roughness effect on cell viability was evaluated using GNPs comparing with GNSs of same diameter. The toxic concentration range for GNPs was found to be widely below the ones observed for GNSs (figure 3(C)). It is clear that GNPs show 50% of viability at 1 pM concentration, while a weak cytotoxicity is noticed below this concentration. This viability threshold is two orders of magnitude lower than the one observed for GNSs having the same size. One can notice that the GNPs have a largely higher toxicity than the GNSs. This is confirmed on figure 3(D) that plots the data from figures 3(A), (B) and (C) in terms of cell viability at 1 pM concentration for all GNPs. 1 pM concentration is the common point for all the GNPs, so this was chosen for comparing their cell viability. Moreover, this

toxic effect is independent of the GNPs surface chemistry since the PEG-GNPs also show 50% of viability at 1 pM. It seems that the PEG slightly improves the cell viability but not with the same efficiency than for GNSs. In this latter case, the PEGylated surface improves the GNSs biocompatibility by one or two orders of magnitude in concentration. It clearly demonstrates that flower shape considerably increase the GNPs cytotoxicity. The reason of this shape-dependant toxicity supports the assumption that the GNP's roughness is responsible of the cell membrane disruption. Moreover, GNPs have higher surface than GNSs and have higher probability of membrane interaction due to relatively large spiky surface [30]. This result is interesting and points out that the surface roughness is a critical parameter in the biocompatibility of the GNPs. One can also conclude that during future therapeutic applications of GNPs, PEG-GNSs can be used at 100 times more concentrated dose than the GNPs.

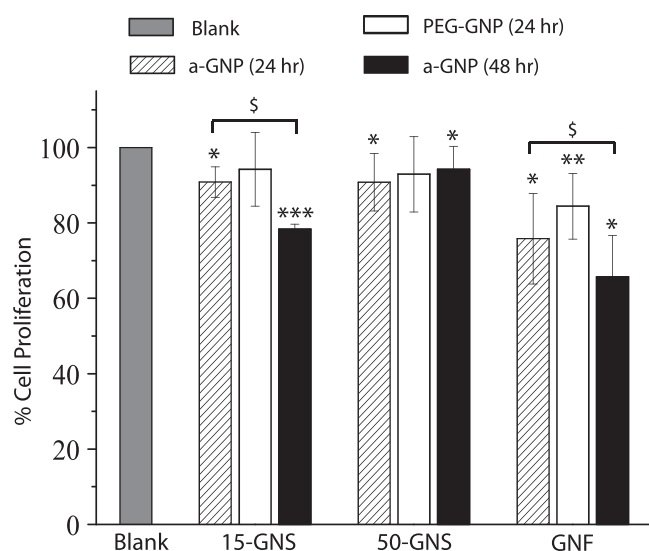


Figure 4. Relative cell proliferation of HUVEC exposed for 24 h and 48 h to both a-GNPs and PEG-GNPs. Concentrations used are 10 pM for 15- and 50-GNS whereas 0.5 pM for GNF. The values are represented as the mean value \pm SD ($n=9$) where * denotes significant changes between blank and GNPs treated cells; and § denotes significant changes between 24 h and 48 h time incubation of a-GNPs incubated cells. Here * $p < 0.05$; ** $p < 0.01$; *** $p < 0.001$ and § $p < 0.05$ (ANOVA).

3.3. Flow cytometric and dark field analysis of HUVEC/GNP interactions

3.3.1. HUVEC proliferation after GNP treatment. To further compare the influence of both shapes of GNPs, their specific interaction with HUVEC was evaluated *in vitro* using fluorescence activated cell sorting (FACS) assay. Upon determination of the toxic concentration range of each of the GNP samples, which is the start point of cytotoxicity, the corresponding threshold concentrations (10 pM for both GNSs and 0.5 pM for GNPs) have been considered to perform cell proliferation rate analysis by FACS. A course of time incubations was performed for 24 and 48 h (for all six particles) and have been chosen based on the cell's own proliferation rate. The time point of 24 h incubation has been chosen to compare with MTT assay and 48 h for having another cell doubling period for this cell line in presence of GNPs.

Thus comparative results with blank become prominent after the FACS of 24–48 h of cell-GNP incubation times (illustrated in figure 4). The relative value of cell proliferation is plotted for both a-GNP and PEG-GNP at their corresponding threshold toxic concentrations (10 pM for all GNSs and 0.5 pM for GNPs) corresponding up to 70% of cell viability.

The data shows that the cell proliferation is not affected by the 50-GNSs whereas the 15-GNSs and the GNPs induce a significant decrease of the cell proliferation after 48 h. One can also notice that GNPs have a higher effect compared to GNSs. After 24 h, the proliferation is weakly affected by the change of the surface chemistry since we get the same rate for both a-GNPs and PEG-GNPs. Thus, the relative proliferation rate seems to be highly influenced by both size and shape of

GNPs. The GNPs effect on the proliferation is coherent with the one observed on the cell mortality rate and confirms the results on viability tests.

3.3.2. Cellular uptake and distribution of GNP. To have a better insight on the interaction mechanism between the GNPs and the cells, we have performed cells imaging which allows determining the cellular uptake of the GNPs inside the cells. As from the viability assay we have already found that PEG-GNPs are less toxic to the cellular environment than a-GNPs, we only show the uptake results for the a-GNPs to show the maximal effect induced by the uptake.

Plasmonic properties of GNPs show interesting effects allowing optical imaging through dark field microscopy. Figure 5 represents the dark field images of HUVEC after incubation with GNPs for 3 h. Due to their strong light scattering, which is a consequence of their plasmonic characteristics, the GNPs are clearly visible as bright spot inside the cells or at the cell surface. Thus, in the dark field images, the GNPs can be easily localized [35]. Moreover, the intensity of the bright spots depends on the number of GNPs observed within the collection volume.

Thus the blank image (figure 5(A)) is nearly black since no GNPs are present in the cells environment. Figure 5(B) shows that 15-a-GNSs are internalized inside the cells. They are homogeneously distributed on the whole cell cytoplasm but not inside the cell nucleus (the nucleus remains dark in the figure 5(B)). Our observation proves the existence of 15-a-GNS in the intra-cellular area and supports the aforementioned investigations that GNSs with diameter greater than 10 nm in size cannot internalize inside the cell nucleus [21]. On the figure 5(C), the bright spots are highly intense compared to the figure 5(B). This suggests that the 50-a-GNSs are aggregated on specific localizations. These localizations seem to be at the exterior part of the cell membrane since the brightest spots are located at the border of the cells and as a consequence a few numbers of 50-a-GNS are internalized inside the cells. This means that smaller spheres are more internalized than the larger ones.

Moreover, since the 50-GNSs aggregate at the membrane surface, it should limit their internalization inside the cell due to a too large size of the aggregates. In case of GNPs, the number of spots is larger and brighter than for the 15-a-GNSs which indicate that the internalization occurred at higher density than GNSs. The bright spots for GNPs are observed from the entire cellular region meaning that the GNPs spread in the entire intra-cellular region of the cells including the cytoplasm as well as the nucleus. Thus, the roughened surface of GNPs formed by tips can have two main effects. First, the tips at the GNPs surface could facilitate the penetration of the nanoparticle inside the cell membrane due to the application of a higher pressure on the membrane compared to a GNS with a smooth surface. Second, the roughness increases also the particle total surface area, therefore determining their higher chances to attach on the cells. There is also higher probability of attachments of membrane receptor proteins on large surface area of GNPs. In both cases, the consequence is

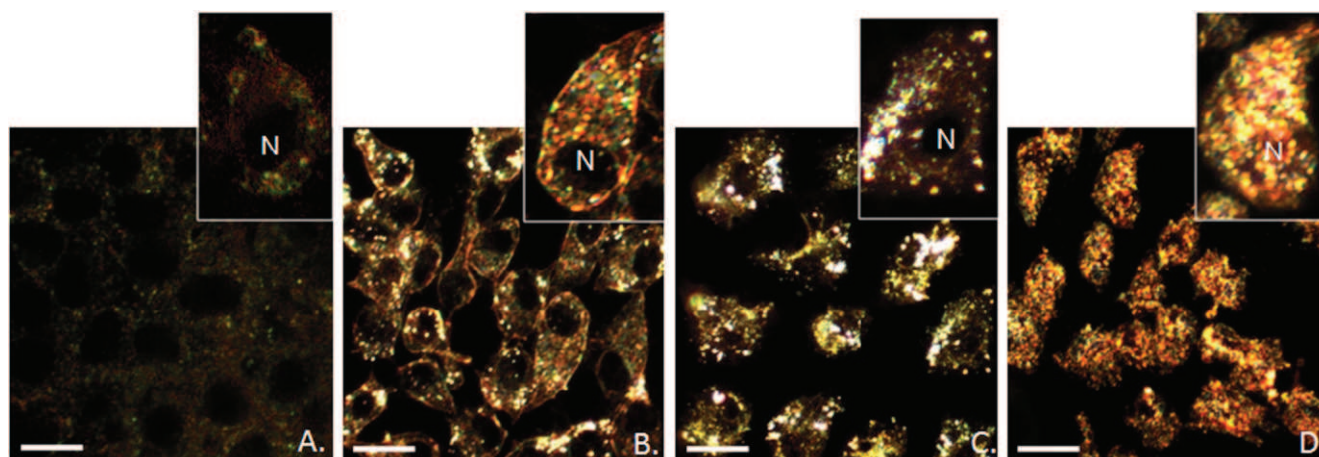


Figure 5. Dark field images of HUVEC incubated for 3 h. (A) Blank with no GNPs. Images of HUVEC incubated with 0.5 pM of (B) 15-a-GNS, (C) 50-a-GNS and (D) a-GNF. Here, N denotes to nucleus. Scale bar of the enlarged cell images: 10 μm .

a higher internalization of the GNPs inside the cells compared to GNSs as observed on figure 5(D), but also internalization inside the nucleus of the cell. As a consequence, the GNPs will induce higher disruption within the cell and thus the cell mechanisms will be more affected than in the case of GNSs. This effect is more enhanced since the GNPs are also internalized inside the cell nucleus. Moreover, the GNPs could also contribute to the plasma membrane damage by decreasing lipid bilayer stability. Thus it may compromise the uniform barrier function of the plasma membrane [36]. These effects due to the GNP internalization will have strong influence on the cell and will induce its early death as observed with the viability and proliferation tests.

3.4. Effects of GNPs on cell cytoskeleton and cell spreading

To confirm the influence of the GNP internalization on the cell mechanisms, we have evaluated the changes in cell physiological phenomena like cell morphology and cytoskeletal organization in adherent endothelial cells [37] in the presence of GNPs. Since cytoskeleton compose the cortex of endothelial cells, it is a crucial cellular zone that determines endothelial function [38] like- spreading, cell migration, vascular tube formation. Moreover, it is also important to differentiate between cytotoxicity and cellular damage. Indeed, GNPs that show little or no cytotoxicity via several standard assays may be still able to cause serious cellular damage by altering cell physiological phenomena. In this study, we focused on comparative effect of GNPs [39] on the cell spreading, which is important to cell survival after cell attachment. Especially we report GNPs effect on actin cytoskeleton modification, cell morphology and surface area. For the spreading test, HUVEC were incubated in presence of 0.5 pM of each of the GNP samples for 3 h. This concentration was chosen since it is the one for which the GNPs started to show significant toxicity.

Figure 6 illustrates the results of cell morphology, actin cytoskeleton structure and histograms of measured cell surface area of blank and treated cells with GNPs. In control condition (figure 6(A)) of non-treated HUVEC, fluorescence

microscopy images showed F-actin fibers (with rhodamine-labeled phalloidin) in whole cell body and in adhesion focal contacts. The cells had well spread form showing cell-to-cell or cell-to-extracellular matrix focal adhesion complex (FAC). F-actin fibers had continuous thread-like structure which seemed nicely distributed along the cell body giving to the endothelial cell an appropriate regular morphology (not deform, not compact cell shape, well spread shape).

In the case of treated cells with GNSs, coexistence of both deformed and few spread cells with healthy structure are observed (figures 6(B1) and (C1)); whereas, treated cells with GNPs showed more deformed and compact cells with a highly concentrated actin fibers in cell peripheries (figure 6(D1)). In general, we observe that F-actin cytoskeleton of all GNPs treated cells has been alternated compared to blank, well spread cells showing the stress fibers formation.

After 3 h incubation with GNPs, the cell surface areas were measured for 100 cells from both GNPs treated and non-treated (blank) cells and represented as histograms to elaborate quantitatively the extent of changes in cell morphology. Thus it fully represents the stress caused by the presence of GNPs.

The mean cell surface area of 50-PEG-GNSs treated cells is around 540 μm^2 whereas for 50-a-GNSs, the cell surface area is about 420 μm^2 (figure 6(B2)). In the case of 15-PEG-GNSs, the mean surface area of treated cells was around 440 μm^2 , while for 15-a-GNSs it was close to 340 μm^2 (figure 6(C2)). GNPs exhibited a prominent shape effect on the cell surface area (figure 6(D2)). For both surface chemistries the surface area was reduced to 350 μm^2 for PEG-GNFs and to 260 μm^2 for a-GNFs. Therefore, comparing to control (650 μm^2), the loss in cell surface area was in order of a-GNFs (60%) > 15-a-GNSs (48%) > 50-a-GNSs (35%). This observation can also be done for all PEG-GNPs such as the loss in cell surface is estimated to be PEG-GNFs (46%) > 15-PEG-GNSs (32%) > 50-PEG-GNSs (17%). Thus, a decrease of the surface area of the cells is observed for all the GNPs and all surface chemistry. This indicate that whatever the GNPs used, the cells are stressed even if this effect is reduced by the used of PEGylated surface chemistry and by the use of

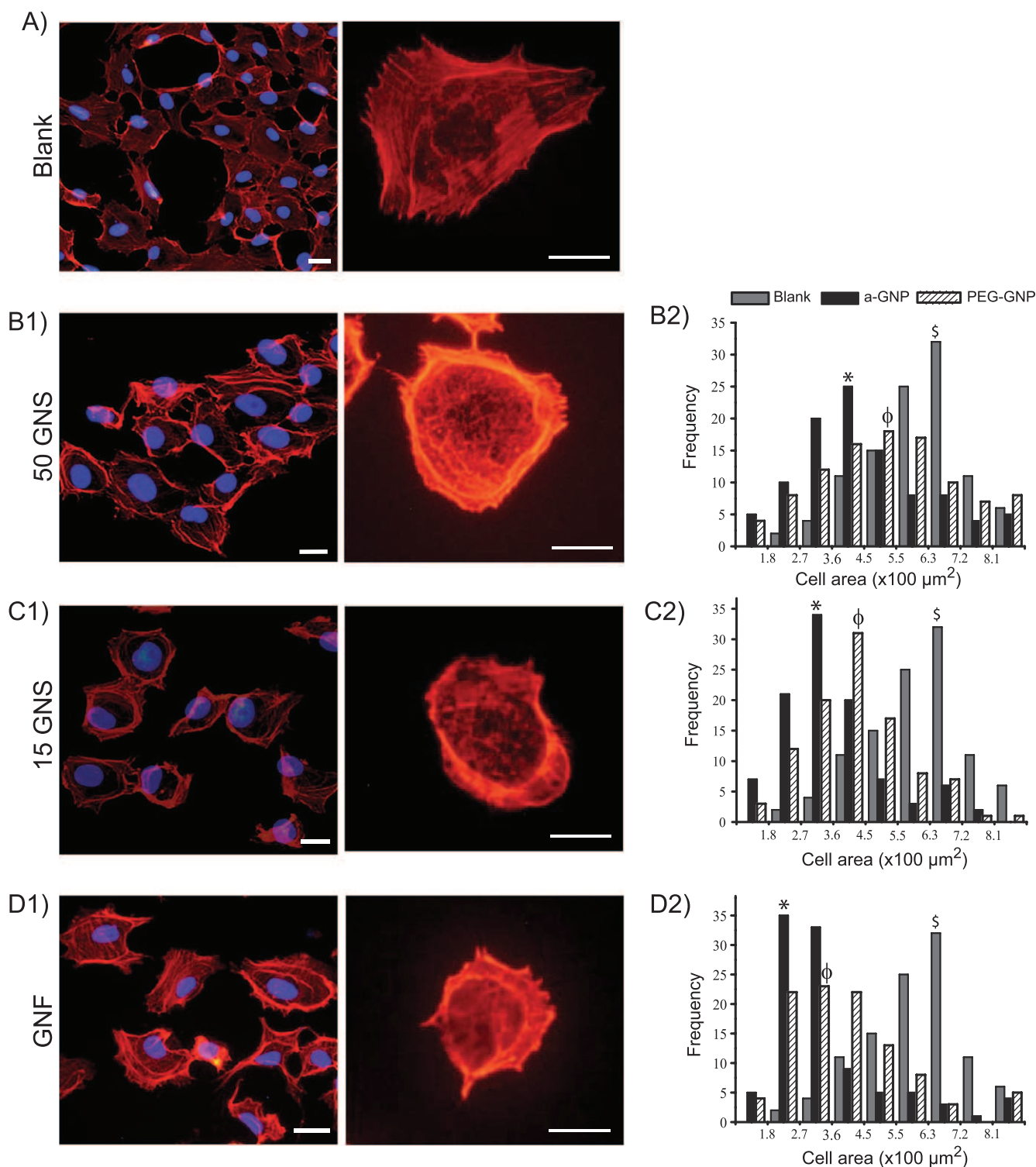


Figure 6. Fluorescence images of HUVEC incubated with 0.5 pM of GNPs for 3 h (A: blank, B1: 50-a-GNS, C1: 15-a-GNS and D1: GNF) (scale bar: 7 μm). Nuclei are labeled with DAPI (blue) and actin cytoskeleton with Alexa Fluor 546-phalloidin (orange-red). Histograms represent the cell surface areas of control cells (gray) and cells incubated with (B2) 50-GNS, (C2) 15-GNS and (D2) GNF. In histograms, black and striped bars demonstrate consecutively as prepared and PEG surface chemistries of the GNPs. Moreover, § denotes average cell area of cells in blank, * and ϕ denote the average surface area of as prepared and PEG-GNPs treated cells respectively.

50-GNS. Furthermore, we observe the same hierarchical organization of the effects as for the previous experiments meaning the highest effect for the a-GNF and the lowest one for the 50-PEG-GNS.

The mechanism of cytoskeleton changes is still not clear, but reported to be a consequence of a decrease in focal contact with the culture plate in presence of GNPs. There are several reasons or hypothesis to explain the F-actin alteration and

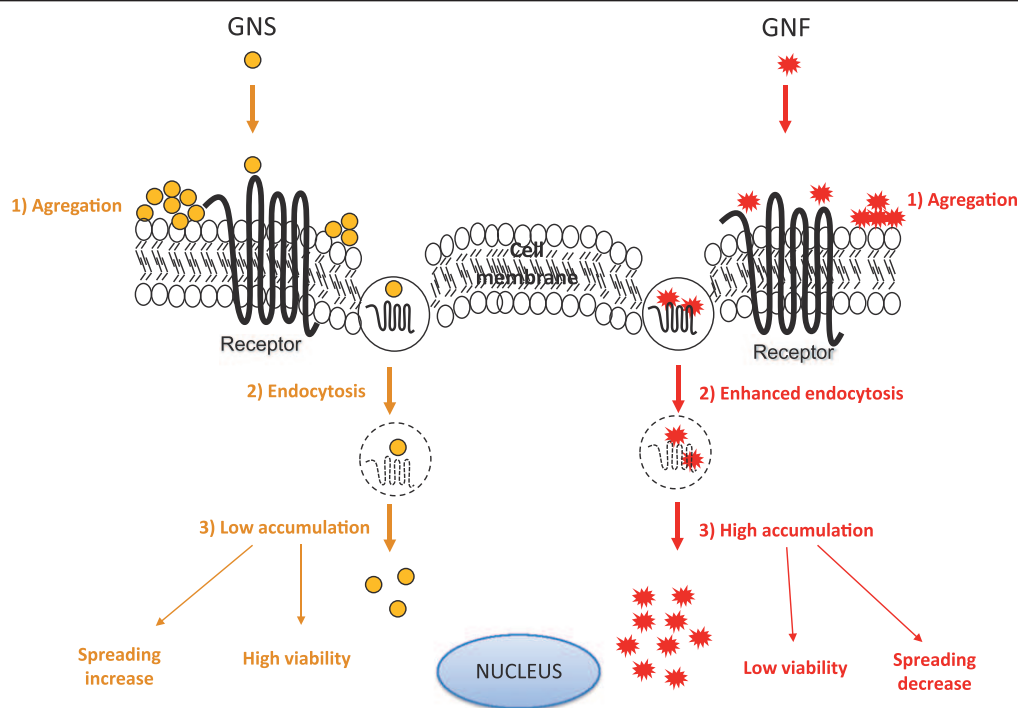


Figure 7. Schematic representation of comparative effects of GNSs and GNPs on HUVEC cells after administration in the cellular media.

stress fibers formation. Any external nanoscale roughness in contact with cell membrane affects cell membrane conformity (tension). It alters the stresses exerted on the cell membrane through FAC and results in enhanced F-actin fiber alignment [40]. Reduced focal contacts and reduced cell area causing a change in the cell morphology [41], from well-spread to mushroom-shaped cells. More the cells are retracted, more compact cell shape is observed, less is the cell surface area.

On the other hand, the presence of GNPs inside cells can create steric hindrance with cell's own existing or newly formed cytoskeletal network enabling them to disorganize, disrupt or remodel [16]. It has been supported by Soenen *et al* that GNPs-loaded endolysosomal structures enlarge in size and lose their functionality, leading to reorganization of the actin cytoskeleton (which also involves its polymerization) and giving rise to structures called stress fibers [42].

However, the reorganization of actin microfilaments and the observation of a deformation of the cell shape are the characteristics of the stressed cells due to GNPs incubation [43]. Cell shape deformation and rounding up is proportional to the decrease in surface of interaction between the cell and culture substrate. This is why cell surface area was measured for 100 cells for both blank and treated cells and histograms which fully represent the stress caused by the presence of GNPs. Physical dimensions of GNPs though being at nanoscale are not negligible compared to micrometer sized cells. Thus, GNP can have impacts on cellular morphology and cytoskeleton network just by occupying intracellular volume [44].

The present work demonstrates that the GNPs have a strong impact on the HUVEC causing early cell death even for concentration lower than the pM. We also demonstrate

that although at low 0.5 pM concentration, GNSs did not show any effect on HUVEC viability or proliferation, this does not mean they are innocuous to cells at such concentration. However, our study showed that the incubation of 0.5 pM GNPs with cells caused the alterations on the cytoskeleton network, cell spreading and lead to changes in cell morphology even at this low concentration and for incubation time as short as 3 h. Though cell viability assays (result not shown here) performed at 3 h incubation time did not show any cell death but this time is sufficient for GNPs internalization inside cells and to cause stress to the cell organelles, such as to actin cytoskeleton.

Based on above results, we can propose a mechanism of GNSs and GNPs action on the cells starting from the GNP-cell interactions until cell apoptosis.

After addition of GNPs into the cell culture they will have different behavior within the biological media and in contact with the cell membrane. This will induce various interaction processes with the cells. The GNPs are internalized into the cells by receptor-mediated endocytosis processes (1); and our hypothesis is that this endocytosis is not similar for the GNPs and GNSs (and even different depending on the GNPs size) and that the cells are affected depending on the GNPs internalization. As summarized on the figure 7, the internalized GNPs can be entrapped and transported inside endosomes, then endosomes are transformed into lysosomes by maturation [26]. Finally upon degradation of the lysosomes, GNPs can be liberated in to the cytoplasm (2), leading to their local accumulation (3) and alteration of cells' physiological phenomena (decrease in cell proliferation rate, disorganization of the cytoskeletal structure, decrease in cell spreading; and finally lead to low viability and cell death). We

assume that GNPs induced cell killing supports apoptotic cell death. As we have noticed deformation of F-actin structure (as mentioned in figure 6), this proves the apoptosis effect because F-actin deformation due to nanoparticle treatment is the first sign associated with apoptotic cell death [45]. Our results showed that GNFs were more accumulated in the cell cytoplasm of human endothelial cells than GNSs; thus the alteration in cells' phenomena has higher effect than in case of GNSs. Higher is the internalization, lower is the cell viability and higher is the cell mechanism disruption.

4. Conclusion

In this paper, we demonstrate that the cytotoxicity of the GNPs depends on the size and the shape of the GNPs as well as on the surface chemistry. We showed that increasing concentration of nanoparticles decreased cell viability; and thus we determined the threshold toxic concentration of around 100 pM, 10 pM and 0.5 pM consecutively for 50-a-GNSs, 15-a-GNSs and a-GNFs. Flow cytometry analysis also demonstrated the more deleterious effect of GNFs over GNSs. We noticed more affinity of GNFs on HUVEC than 15-GNSs, where 50-GNSs had the least affinity. We were able to compare the degree of cytotoxic effect and demonstrated that it is largely higher for GNFs than for GNSs. Even if we showed an enhanced biocompatibility of the GNSs due to the PEG coating, we demonstrated that the surface chemistry has no effect for the GNFs. This latter point indicates that the main parameter in the evaluation of the GNPs toxicity is the GNPs roughness. Thus, even if the GNFs have optical properties that imply a better efficiency in application as photothermal therapy, they could have more deleterious effects on the biological media.

Moreover, our complete study suggests that looking into viability and proliferation rate do not give the global picture of toxicity, so detailed multi-parametric *in vitro* study is essential by focusing on the effect on cell organelles (in this case cytoskeleton).

Acknowledgments

This work has been supported by the Region Ile-de-France in the framework of DIM C'Nano IdF and 'Nanosciences in Ile-de-France'.

Conflict of interest

None declared.

References

- [1] Ricketts K, Castoldi A, Guazzoni C, Ozkan C, Christodoulou C, Gibson A P and Royle G J 2012 *Phys. Med. Biol.* **57** 5543
- [2] Paciotti G F, Myer L, Weinreich D, Goia D, Pavel N, McLaughlin R E and Tamarkin L 2004 *Drug Deliv.* **11** 169–83
- [3] Amitava D, Priyabrata M, Sumit K S, Praveen G, Megan C F, Debabrata M, Vijay H S and Chitta Ranjan P 2010 *Nanotechnology* **21** 305102
- [4] De Freitas L F et al 2013 *Laser Phys.* **23** 066003
- [5] Boris K, Vladimir Z, Andrei M, Valery T and Nikolai K 2006 *Nanotechnology* **17** 5167
- [6] Huang X, Jain P K, El-Sayed I H and El-Sayed M A 2007 *Nanomedicine* **2** 681–93
- [7] Jain P K, Lee K S, El-Sayed I H and El-Sayed M A 2006 *J. Phys. Chem. B* **110** 7238–48
- [8] Yuan H, Khoury C G, Wilson C M, Grant G A, Bennett A J and Vo-Dinh T 2012 *Nanomedicine: NBM* **8** 1355–63
- [9] De Broek B V, Frederix F, Bonroy K, Jans H, Jans K, Borghs G and Maes G 2011 *Nanotechnology* **22** 015601
- [10] Rodríguez-Lorenzo L, Krpetic Z, Barbosa S, Alvarez-Puebla R A, Liz-Marzán L M, Priore I A and Brust M 2011 *Integr. Biol.* **3** 922–6
- [11] Yuan H, Fales A M, Khoury C G, Liu J and Vo-Dinh T 2013 *J. Raman Spectrosc.* **44** 234–9
- [12] Boca S, Rugina D, Pintea A, Barbu-Tudoran L and Astilean S 2011 *Nanotechnology* **22** 1–7
- [13] Sau T K, Rogach A L, Jäckel F, Klar T A and Feldmann J 2010 *Adv. Mater.* **22** 1805–25
- [14] Alkilany A M, Nalaria P K, Hexel C R, Shaw T J, Murphy C J and Wyatt M D 2009 *Small* **5** 701–8
- [15] Bartczak D, Muskens O L, Nitti S, Sanchez-Elsner T, Millar T M and Kanaras A G 2012 *Small* **8** 122–30
- [16] Soenen S J, Rivera-Gil P, Montenegro J-M, Parak W J, De Smedt S C and Braeckmans K 2011 *Nano Today* **6** 446–65
- [17] Raja G R, Wilma P, Liesbeth H, Patrick C, Hans J, Fijs W B V L, Cees O, Srirang M and Ton G V L 2010 *Nanotechnology* **21** 145101
- [18] Connor E E, Mwamuka J, Gole A, Murphy C J and Wyatt M D 2005 *Small* **1** 325–7
- [19] Díaz B et al 2008 *Small* **4** 2025–34
- [20] Pan Y, Neuss S, Leifert A, Fischler M, Wen F, Simon U, Schmid G, Brandau W and Jahnen-Dechent W 2007 *Small* **3** 1941–9
- [21] Chithrani B D, Ghazani A A and Chan W C W 2006 *Nano Lett.* **6** 662–8
- [22] Cui W, Li J, Zhang Y, Rong H, Lu W and Jiang L 2012 *Nanomedicine: NBM* **8** 46–53
- [23] Arvizo R R, Rana S, Miranda O R, Bhattacharya R, Rotello V M and Mukherjee P 2011 *Nanomedicine: NBM* **7** 580–7
- [24] Permodet N, Fang X, Sun Y, Bakhtina A, Ramakrishnan A, Sokolov J, Ulman A and Rafailovich M 2006 *Small* **2** 766–73
- [25] Jiang W, Kim B Y S, Rutka J T and Chan W C W 2008 *Nat. Nanotechnology* **3** 145–50
- [26] Shukla R, Bansal V, Chaudhary M, Basu A, Bhone R R and Sastry M 2005 *Langmuir* **21** 10644–54
- [27] Freese C, Gibson M I, Klok H-A, Unger R E and Kirkpatrick C J 2012 *Biomacromolecules* **13** 1533–43
- [28] Arnida, Malugin A and Ghandehari H 2009 *J. Appl. Toxicol.* **30** 212–7
- [29] Niidome T, Yamagata M, Okamoto Y, Akiyama Y, Takahashi H, Kawano T, Katayama Y and Niidome Y 2006 *J. Control. Release* **114** 343–7
- [30] Hutter E, Boridy S, Labrecque S, Lalancette-Hébert M, Kriz J, Winnik F M and Maysinger D 2010 *ACS Nano* **4** 2595–606
- [31] Sironi L et al 2012 *J. Phys. Chem. C* **116** 18407–18
- [32] Boca S C, Farcau C and Astilean S 2009 *Nucl. Instrum. Methods B* **267** 406–10

- [33] Brandenberger C, Mühlfeld C, Ali Z, Lenz A-G, Schmid O, Parak W J, Gehr P and Rothen-Rutishauser B 2010 *Small* **6** 1669–78
- [34] Horisberger M and Clerc M F 1985 *Histochemistry* **82** 219–23
- [35] Boca S C, Potara M, Toderas F, Stephan O, Baldeck P L and Astilean S 2011 *Mater. Sci. Eng. C* **31** 184–9
- [36] De Planque M R R, Aghdaei S, Roose T and Morgan H 2011 *ACS Nano* **5** 3599–606
- [37] Wu X, Tan Y, Mao H and Zhang M 2010 *Int. J. Nanomed.* **5** 385–99
- [38] Kai Bodo G, Hans O and Johannes F 2014 *Nanotechnology* **25** 215101
- [39] Mironava T, Hadjiargyrou M, Simon M, Jurukovski V and Rafailovich M H 2010 *Nanotoxicology* **4** 120–37
- [40] Curtis A S G, Gadegaard N, Dalby M J, Riehle M O, Wilkinson C D and Aitchison G 2004 *IEEE Trans. NanoBiosci.* **3** 61–5
- [41] Lipski A M, Pino C J, Haselton F R, Chen I W and Shastri V P 2008 *Biomaterials* **29** 3836–46
- [42] Huot J, Houle F, Rousseau S, Deschesnes R G, Shah G M and Landry J 1998 *J. Cell. Biol.* **143** 1361–73
- [43] Patra H K, Banerjee S, Chaudhuri U, Lahiri P and Dasgupta A K 2007 *Nanomed.: Nanotechnology Biol. Med.* **3** 111–9
- [44] Soenen S J H, Nuytten N, De Meyer S F, De Smedt S C and De Cuyper M 2010 *Small* **6** 832–42
- [45] Liu M, Gu X H, Zhang K, Ding Y, Wei X B, Zhang X M and Zhao Y X 2013 *J. Nanopart. Res.* **15** 1745

Chapter 4

FCS Experiments

5. Fluorescent nanoparticle characterization by FCS

Summary:

5.1 Characterization of fluorescent Streptavidin conjugated gold nanoparticles by FCS

5.1.1 Methods and materials

5.1.1.1 Reagents

5.1.1.2 Synthesis and characterization of gold nanoparticles

5.1.1.3 Biotinylation of gold nanoparticles and conjugation of streptavidin-Alexa Fluor 633

5.1.2 Results and discussion

5.1.2.1 Nanoparticles characterization before fluorophore conjugation

5.1.2.2 FCS Characterization of binding of fluorescent Streptavidin to Biotinylated GNSs

5.2 Characterization of fluorescent core-shell gold-silica nanoparticles by FCS

5.2.1 Methods and materials

5.2.1.1 Reagents

5.2.1.2 Synthesis of core-shell gold-silica nanoparticles

5.2.1.3 Synthesis of CS1 GNPs

5.2.1.4 Synthesis of CS2 GNPs

5.2.1.5 Characterization of fluorescent gold nanoparticles by FCS

5.2.2 Results and discussion

5.2.2.1 Nanoparticles characterization before fluorophores conjugation

5.2.2.2 FCS characterization of Alexa fluor conjugated core-shell gold-silica nanoparticles

5.1 FCS characterization of fluorescent Streptavidin conjugated gold nanoparticles

Nanoprobe design and development is a challenging domain, specially optimizing fabrication of fluorescent nanoprobe is more of a challenge. Organic fluorophores attached on noble metal nanoparticles have opened a new era of nanoprobe engineering. Due to Surface-Enhanced Fluorescence (SEF), the fluorescence emission of the fluorophore attached on metal nanoparticle show strong fluorescence enhancement effects. So they have promising applications as nano probe.

A major issue during development of fluorescent nanoparticles is their proper single molecule characterization to tune the size, concentration and fluorophore attachments on metal nanoparticle surface as well as to ensure the brightness and stability of fabricated nanoparticles. Fluorescence Correlation Spectroscopy (FCS) is a powerful technique enabling single fluorescent molecule detection due to extremely small ($<fL$) confocal detection volume and thus allows us to obtain fundamental properties of the fluorescent molecules or nanoparticles; such as diffusion coefficient, hydrodynamic radius, brightness of molecules, and concentration in a single experiment ⁷⁷. Potential applications of FCS are- interaction studies ⁷⁸, growth kinetics of nanoparticles or nanocrystals ⁷⁷.

Zhang *et al.* characterized gold nanoparticle diffusion parameters by eliminating the optical trapping effect and determined GNPs diameters using resonance light scattering correlation spectroscopy (RLSCS); where they have utilized resonance light scattering fluctuations from the gold nanoparticles instead of fluorescence fluctuations used in FCS. Thus GNPs diameters were obtained by RLSCS with the help of their the characteristic diffusion time and obtained result of diameters were in good agreement with that obtained by TEM ⁷⁹. Media *et al.* evidenced adsorption of BSA protein on citrate-stabilized GNPs surface using Scattering correlation spectroscopy technique. Analysis of the diffusion parameters before and after protein adsorption showed an increase in the GNP hydrodynamic radius, which corresponds to the formation of a BSA monolayer on GNP surface ⁵⁴.

Sharma *et al.* demonstrated the kinetic steps of micro emulsion controlled iron oxalate nanorod growth by FCS through monitoring the reaction kinetics of droplet coalescence at the single-droplet level; the process which initiates the reaction and allows the subsequent growth of nanostructures ⁵³. Xu *et al.* innovated a sensitive and direct determination of thrombin in human plasma with the aid of FCS. They used GNPs as probe conjugating two different aptamers and upon mixing aptamer-labeled GNPs in the solution of thrombin; dimers or oligomers were formed due to the affinity reaction. Thus quantitative analysis of thrombin

was performed based on the measurement of the change in the diffusion time of the GNPs before and after the affinity reaction, and the detection limit was determined as 0.5 nM⁸⁰.

Herein, we report fluorescent Streptavidin conjugation on polymer coated GNPs. We first synthesized citrate-reduced 18 nm spherical GNPs (18-GNS). The GNSs surface was modified by enshrouding the colloids with thiolated Poly-Ethylene-Glycol (m-PEG-SH). PEG functionalized GNSs (18-PEG-GNS) were treated chemically to have carboxylated PEG ends which is at the opposite part of the PEG chain bound on the gold surface. Biotin-NHS having NH₂ group with the molecule were easily conjugated with PEG-carboxylate and bound with fluorescent streptavidin (Streptavidin-Alexa 633) due to the innate affinity between biotin-Streptavidin. Here, PEG chain and bound biotin-Streptavidin part is almost 5-6 nm long which is acting as the spacer to reduce competitive quenching as well as to induce metal enhanced fluorescence. FCS is a powerful technique to study the metal-fluorophore interaction at the single molecule level by separating the diffusion time between bound and unbound fluorescent Streptavidin.

5.1.1 Methods and materials

5.1.1.1 Reagents

The chemicals and materials for fabrication of gold nanoparticles (18-GNS) are mentioned elsewhere⁸¹. Reagents for stabilizing and functionalization of 18 GNS are- α -methoxy- ω -mercapto poly (ethylene glycol) (mPEG-SH) of molecular weight 5 kDa was obtained from Iris biotech GmbH (Germany). (+)-Biotin N-hydroxysuccinimide ester, Phosphate buffer saline (PBS) 1X, pH 7.4 and Cystamine dihydrochloride were purchased from Sigma-Aldrich, France. Alexa Fluor 633 NHS ester and Streptavidin-Alexa 633 conjugate were purchased from Molecular Probes, Life technologies, France.

5.1.1.2 Synthesis and characterization of gold nanoparticles

Synthesis of 18 nm tri-sodium citrate reduced spherical gold nanoparticles and the characterization methods were mentioned elsewhere⁸¹. After fabrication of GNPs, thiolated polyethylene glycol (m-PEG-SH) polymer was conjugated on the GNPs to provide more stability to the particles and methods were mentioned elsewhere⁸². To determine 18-PEG-GNSs concentration in colloidal solution, optical extinction spectra were measured with a UV-Vis spectrometer (Kontron Instr. France) at a spectral range from 400 nm to 900 nm. The

wavelength of absorption maxima was used to calculate stock concentration using corresponding extinction coefficient. Zeta potential measurements of the colloidal nanoparticles were performed using a Zetasizer Nano-ZS90 instrument purchased from Malvern.

5.1.1.3 Biotinylation of gold nanoparticles and conjugation of streptavidin-Alexa Fluor 633

0.1 nM of 18-PEG-GNSs was initially modified to form a self-assembled monolayer (SAM) of cystamine by mixing 3.5 μ M cystamine dihydrochloride solution (pH 7.4 in PBS 1X) to 18-PEG-GNSs solution for 2 h to form an amine functional group. After 2 h, unreacted cystamine was washed out by centrifugation at 10,000 rpm for 10 min and the pellet was dissolved in fresh PBS 1X. Then, 14 μ M of biotin-NHS ester solution (pH 7.4 in PBS 1X) was added to the colloidal 18-PEG-GNSs solution in a slow rotating condition for 2 min and then at 4° C for overnight. The amine group of cystamine modified on the 18-PEG-GNSs surface can couple with the activated NHS ester, and finally form an amino bond between cystamine and biotin, making the conjugation reaction successful, as shown in **Erreur ! Source du renvoi introuvable.**

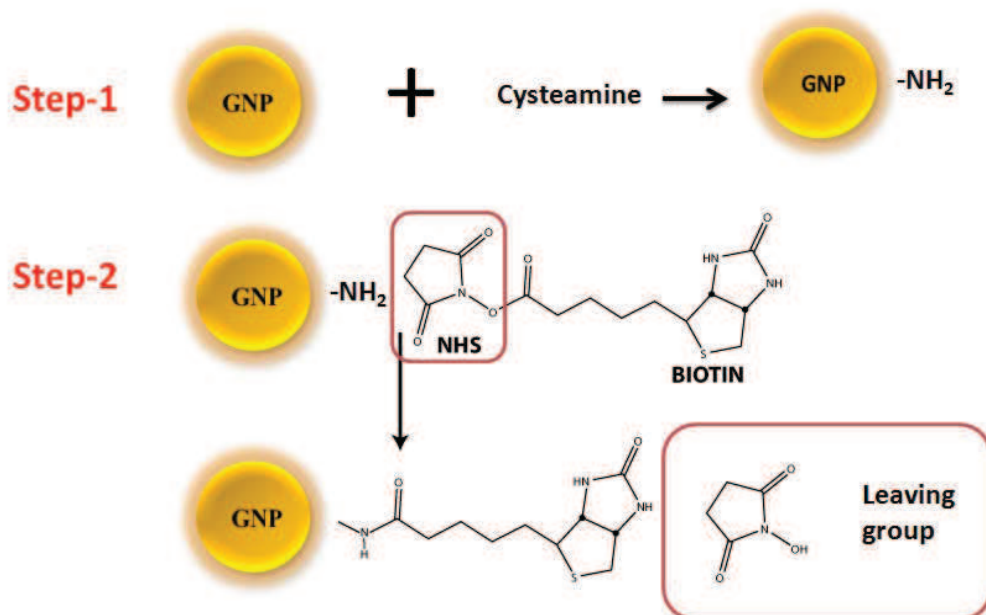


Figure 35. Schematic diagram showing steps of GNPs (here 18-PEG-GNSs) biotinylation

Following morning 3.5 μ M Streptavidin-Alexa633 solution was mixed with 18-PEG-GNS-biotin solution followed by another wash. The protein conjugated GNPs were purified by centrifugation to remove excess Streptavidin-Alexa633 molecules and dispersed in PBS 1X

buffer. In parallel, biotin-NHS and streptavidin-Alexa633 solution were mixed at the same corresponding concentrations and all the biotin-Streptavidin conjugation reactions were performed for 2 h at room temperature. The concentration of cysteamine, biotin-NHS ester and incubation time were varied to find the optimal immobilization conditions.

5.1.2 Results and discussion

5.1.2.1 Nanoparticles characterization before fluorophore conjugation

In the present work, we synthesized gold nanoparticle colloids of 18 nm diameter and of spherical shape (18 GNSs) and further surface modified by coating with PEG molecule (18-PEG-GNSs). The normalized extinction spectra of the gold colloidal solutions along with the electron microscope image (right inset) are illustrated in **Figure 36**.

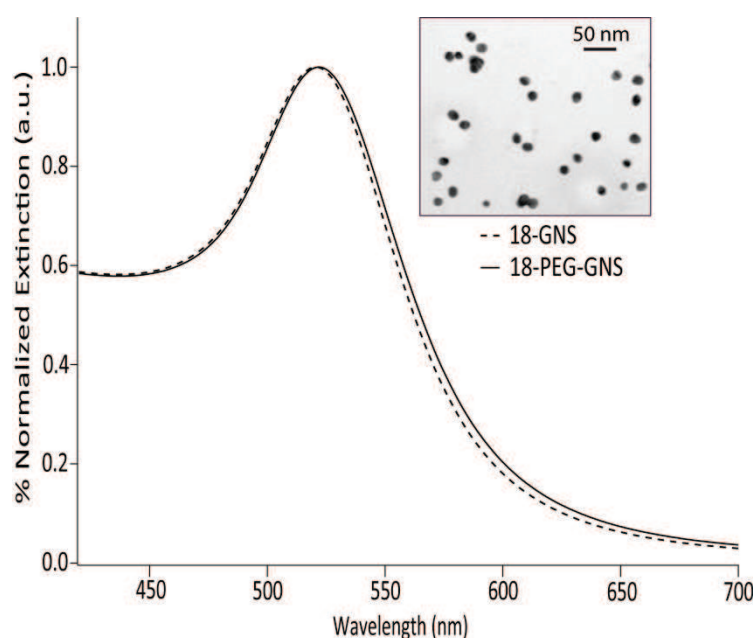


Figure 36. Extinction spectra of 18-GNSs (dotted lines) and 18-PEG-GNSs (solid lines) showing a shift of 2 nm after the PEG modification of the particles. TEM images of 18-GNSs (right inset).

The primary shape and size for as prepared 18-GNSs were determined by Transmission Electron Microscopy (TEM; JEOL 100U, 100 kV accelerating voltage) (inset in **Figure 36**). Before each experiment, concentration of colloidal solution was calculated based on the surface plasmon resonance band of each material derived from the UV-Visible spectroscopy (see Method section). The normalized extinction spectra of the colloidal gold solutions before and after PEG modification are illustrated in **Figure 36**.

18-GNSs exhibited localized surface plasmon resonance (LSPR) bands in the visible region at 520 nm with asymmetry towards the NIR region of the spectrum and 2 nm red-shifted after PEG modification. This characterization of the colloidal nanoparticles is relevant to the literature of the nanoparticles fabricated using same methods⁸¹. The surface ligand exchange was further confirmed by a shift of ζ potential of colloidal nanoparticle measured with a Zetasizer Nano-ZS90 (Malvern Instruments). We observed ζ potential shift from -44 to -3 mV in case of 18-GNSs upon PEGylation.

5.1.2.2 FCS Characterization of binding of fluorescent Streptavidin to Biotinylated GNSs

Binding of Streptavidin-633 with the biotin molecule functionalized on GNSs was successfully verified by FCS based on their corresponding diffusion time τ_D . In the **Figure 37** correlation curves are displayed which are obtained from Alexa-633-NHS ester molecule, Alexa-633 bound Streptavidin (or Streptavidin-Alexa 633), biotin and Streptavidin-Alexa 633 molecule conjugates and finally Streptavidin-Alexa 633 conjugated on biotinylated GNSs.

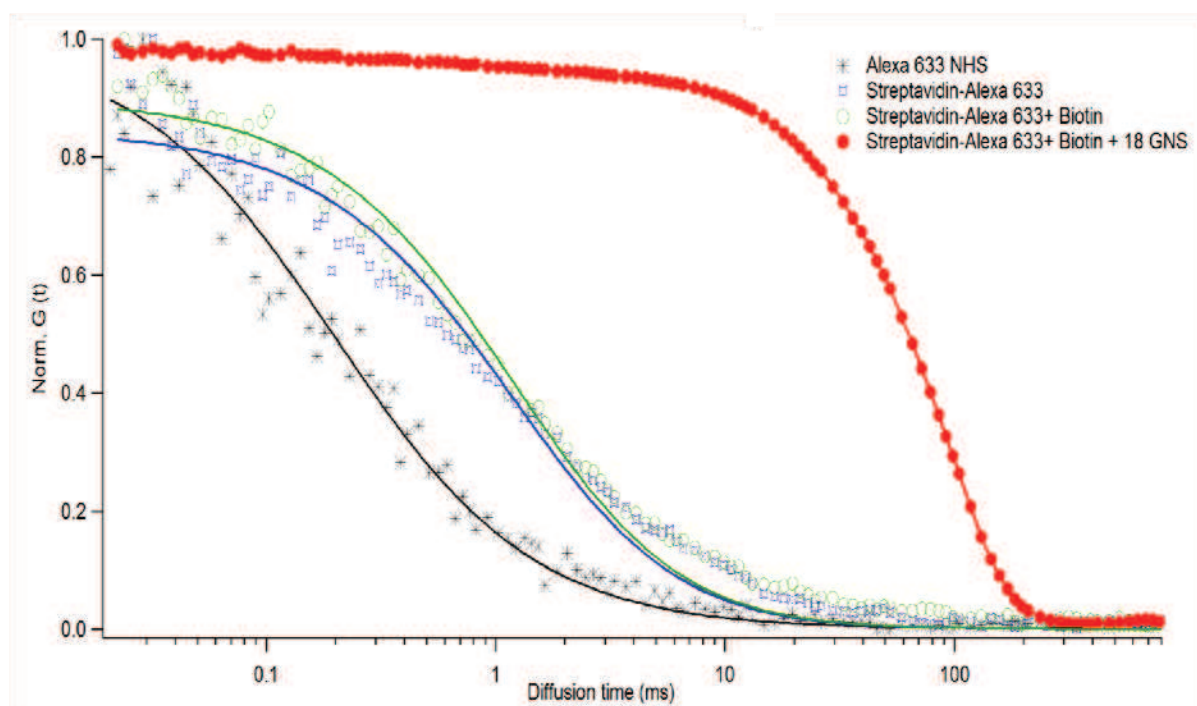


Figure 37. Diffusion time τ_D of (a) Alexa-633-NHS ester molecule, (b) Alexa-633 bound Streptavidin, (c) Biotin and Streptavidin- 633 molecule conjugates and (d) Streptavidin- 633 conjugated on biotinylated GNS.

In **Figure 37**, correlation curves showing diffusion time of molecules and conjugates which are obtained from Alexa-633 NHS ester molecule, Alexa-633 bound Streptavidin, biotin and Streptavidin-633 molecule conjugates and finally Streptavidin-Alexa 633 conjugated on biotinylated GNS. The values of time diffusion and count rate per molecule (CRM) for each of the molecules are also mentioned in the **Table 3**. We know that time diffusion τ_D is dependent on the molecular weight of the molecules and the relationship of this dependability is proportionality. Thus more the molecular weight, the more there is an increase in the value of τ_D . As we can see from the values of Streptavidin-Alexa 633 molecules, is 0.606 ms while only Alexa 633 this value is 0.2 ms. After binding a very small molecule biotin with fluorescent Streptavidin, there was a very little increase in the time diffusion which is 0.95 ms. But interestingly the biggest change in the value of time diffusion is observed after addition of fluorescent Streptavidin with biotinylated GNS. PEG-GNS with 18 nm diameters is clearly with larger molecular weight than a protein molecule itself or a protein attached to a small cofactor like biotin. So the big τ_D value of 94.42 ms proves the successful conjugation of Streptavidin-Alexa 633 with one GNS. Thus we can say that by the aid of FCS we can easily justify any conjugation or binding of fluorescent molecules at a single molecule level.

Table 3. Values of time diffusion and count rate per molecule of free and bound Alexa 633 molecules at different steps of Streptavidin-Alexa 633 conjugation on gold nanoparticles

Fluorescent molecules	Diffusion time, τ (ms)	Count rate per molecule, CRM (kHz)
Alexa 633 NHS	0.20	2.00
Streptavidin-Alexa633	0.60	1.94
Streptavidin 633+Biotin	0.95	2.56
Streptavidin 633+Biotin+GNS	94.42	27.90

The average fluorescence intensity emitted from the Alexa-633 NHS ester and streptavidin-633 molecules have a short range of fluctuation in fluorescence emission traces ranging between 2-3 kHz. But for GNS-Streptavidin 633 conjugates, it varied by few hundred kHz. Moreover, the average intensity (pulse height) for fluorescent Streptavidin 633 was about 25 kHz in PBS where as for GNS-Streptavidin 633 was about 500 to 1000 kHz (figure not shown). Comparison of the count rate clearly indicates that GNP-Streptavidin have a fluorescence intensity which is significantly higher than that of the free dye. Moreover, the

conjugated Streptavidin on GNPs rather gives rise to significant intensity bursts while diffusing via different trajectories through the Gaussian excitation volume. These intensity bursts vary in peak intensity and width reflecting different molecular brightness and size, respectively. The differences in intensity can be due to particles containing more fluorescent molecules on the surface than freely diffusing in the same solution ⁸³.

After fitting the diffusion curves obtained by FCS using appropriate fit program, we can determine different parameters of the molecules diffusion besides time diffusion. One of the important parameters is the count rate per molecule, CRM (in *Table 3*). This is interesting to notice that CRM for Alexa molecule or Alexa bound protein is almost at the same range around 2 kHz. This value was significant for Alexa 633 molecule in this study using the set-up, thus Alexa alone and protein bound Alexa gave almost same result as there is no increase in count rate of Alexa after binding with Streptavidin. But since fluorescent Streptavidin is bound with the gold nanoparticle, we observed a big value of CRM which is 28 kHz. This clearly demonstrates show strong SEF or fluorescence enhancement effects the of Alexa molecules due to the fluorescence emission of this fluorophore attached on metal nanoparticle.

Thus using our FCS set-up we could characterize functionalized gold nanoparticles at molecular level. This possibility encouraged us to characterize other type of gold nanoparticle sample in respect to their molecular weight or radius, based on the effect of different spacers used between the GNP surface and the fluorophore itself. This novel type of gold nanoparticle sample is core-shell silica-gold nanoparticles. Below is the detailed of the sample, fabrication and characterization methods along with the result and discussions are provided at the second part of this chapter.

5.2 Characterization of fluorescent core-shell gold-silica nanoparticles by FCS

One of the most critical steps in designing nanoparticle is the poor stability of as-prepared GNPs (aggregation in ionic solution or biological fluids); that limits their potential applications in many fields such as optics, sensing, therapy and bio-imaging. Therefore, ligand exchange or additional coating on the GNPs surface is essential to improve the colloidal stability. However, many of the stabilizers that are being utilized may affect the solid state properties of the particles ⁸⁴. In order to avoid nanoparticle aggregation and improve the properties for the desirable functionality; compartmentalization in micelles and micro emulsions, while immobilization in glasses or sol gels is the preferred technique⁸⁵.

However, many of the stabilizers employed affect the solid state properties of the particles. To circumvent this problem it is necessary to find a stabilizer which not only prevents particle coalescence but also is chemically inert and optically transparent. These conditions are met by silica, a coating material used in a wide range of industrial colloid products ranging from paints and magnetic fluids, to high-quality paper coatings. To date, silica coating has not been applied to stabilize nano-sized metal particles or to modulate their optical properties⁸⁵. Thus a thin silica coating around the GNPs can not only not only stabilize metal nanoparticles and provides chemical inertness but also allows subsequent fictionalization and biocompatibility by chemically tailoring the surface of silica shells⁸⁶; and modulate optical properties. Fluorescent molecules attached o this silica layer not only gives stability but also behave as a spacer between the GNP surface and fluorescent Alexa molecules to avoid molecular quenching. Thus we can expect strong fluorescence enhancement effect the fluorescence emission of the fluorophore attached on metal nanoparticle due to Surface-Enhanced Fluorescence (SEF) or metal-enhanced fluorescence (MEF) effects.

However, metal-enhanced fluorescence can also lead to photobleaching and quenching⁸⁷, which decrease the enhancement factor. Photobleaching is an irreversible photochemical reaction. The quenching effect is mainly due to the energy absorption at the metal nanoparticle surface of the emitted light coming from the fluorophores⁸⁸. Plasmonic quenching losses critically depend on metal-molecule distance and its effect on fluorescence enhancement can be reduced by including for example a silica shell or a polymer layer as a spacer between the metal core and the fluorescent molecules⁸⁹⁻⁹². One of the powerful techniques to investigate photophysic and dynamic properties of fluorescent nanoparticles is fluorescence correlation spectroscopy (FCS)^{93, 94}. Diffusion coefficients, hydrodynamic radii, concentration and fluorescence enhancement per particle can be determined by analyzing fluorescence intensity fluctuations in a well-defined confocal volume (less than 1 fl)⁹⁵. At sufficiently low concentration (sub-nanomolar), only one molecule or less are detected within this confocal volume. Therefore, the recorded fluorescence intensity shows strong fluctuations (bursts) generated by the diffusing molecules in and out of the observation volume⁹⁶. In this work, we characterize two types of fluorescent core-shell gold-silica nanoparticles. Both are based on gold core of 20 nm diameter covered by 10 nm thickness of silica shell as a spacer layer to prevent the dye quenching. We use near infrared dye, Alexa Fluor647 (AF647) for its relatively high quantum efficiency, good stability and good compatibility for biosensing⁹⁷. For the first type CS1 GNPs, we grafted the fluorophores on the silica surface. While, for the

second type CS2, an external silica shell including the dye was added as a protective layer for the fluorophore.

The characterization of CS GNPs was achieved by SEM, UV-Visible absorption spectroscopy and above all fluorescence correlation spectroscopy (FCS). FCS has been used to determine hydrodynamic diameters and diffusion coefficients of CS GNPs and quantify the fluorescence enhancement for each structure. We investigated the effect of excitation laser intensity on fluorescence enhancement and diffusion properties with CS1 GNPs and we demonstrated the protective role of the silica layer in the case of CS2 GNPs on increasing the fluorescence enhancement factor.

5.2.1 Methods and materials

5.2.1.1 Reagents

Gold (III) chloride hydrate ($\text{HAuCl}_4 \cdot x\text{H}_2\text{O}$) 99.999%, tetraethylorthosilicate (TEOS, 99.999%), 3-aminopropyltrimethoxysilane (APTMS, 97%), ammonia solution (30% wt), sodium silicate solution (Na_2O (SiO_2) wt% SiO_2), ethanol, dimethylsulfoxide (DMSO), phosphate buffer saline (PBS) and trisodium citrate (99%) were purchased from Sigma-Aldrich. 3-aminopropyltriethoxysilane (APTES, 97%) was obtained from ABCR. Alexa Fluor647 succinimidyl ester (AF647) was provided by Life Technologies. Milli-Q water (18.2 M Ω) was used in all the preparations.

5.2.1.2 Synthesis of core-shell gold-silica nanoparticles

Initial gold nanoparticles (GNPs) were prepared using Frens protocol.⁴⁸ To produce 20 nm GNPs, 50 mL of an aqueous 0.25 mM HAuCl_4 solution was heated to reflux under stirring. Then 1 mL of a 34 mM sodium citrate solution was added quickly. Reaction was continued at reflux during 20 min. After cooling, nanoparticles were used without any purification. The synthesis of silica shell was performed using the protocol of Liz-Marzan.⁴² 663 μL of a 0.1 mM solution of APTMS in water was added drop wise and under stirring to 25 mL of the as prepared GNPs solution. The reaction was allowed to continue during 20 min. Then 724 μL of a 0.54%wt sodium silicate solution was added drop wise and under stirring. The reaction was continued during 24 h. Nanoparticles were purified by centrifugation at 960g during 30 min and reconcentrated in 1.4 mL of water. Then 25 mL of ethanol and 625 μL of ammonia

30%wt were added drop wise and under stirring. Finally, two additions of a 44.8 mM TEOS solution in ethanol (2x137.5 μ L) were performed with 1 h spacing between the two additions. The reaction was continued overnight. Finally, nanoparticles were purified by 3 centrifugation cycles at 7700g during 30 min in ethanol and they were finally redispersed in 2 mL of ethanol. The final concentration of nanoparticles was estimated to 1.04×10^{12} NPs/mL by UV-visible absorption measurement.

5.2.1.3 Synthesis of CS1 GNPs

In a first step, gold-silica nanoparticles were treated to obtain amino groups onto silica surface. 1 mL of the previously prepared gold-silica nanoparticles dispersion (1.04×10^{12} NPs/mL) was mixed with 0.5 mL of water and 3.5 mL of ethanol. Then 37 μ L of a 10 mM APTES solution in ethanol was added drop wise and under stirring. The APTES amount was chosen with a 15-fold excess compared to the amount necessary to coat one monolayer of this molecule onto silica surface (the area occupied by one APTES molecule onto silica was estimated to 0.5 nm^2)⁹⁸. Reaction was continued during 24 h under stirring at room temperature and then the solution was heated to reflux at 80°C during 1 h. Nanoparticles were purified by 5 centrifugation cycles at 4900g during 15 min and finally redispersed in 1 mL of ethanol. In a second step, AF647 succinimidyl ester molecules were grafted to gold-silica nanoparticles thanks to their amino reactive functions as follow. Nanoparticles were centrifuged at 4900g during 15 min. The supernatant was discarded and nanoparticles were redispersed in 1 mL of DMSO. The nanoparticles were again centrifuged at 4900g during 15 min. The supernatant was discarded and nanoparticles were finally redispersed in 1 mL of a 95/5 (v/v) bicarbonate buffer 0.1M (pH = 8.5) / DMSO mixture. This pH condition was used to ensure the amine functions were sufficiently deprotonated during the reaction with AF647. Then 16.8 μ L of a 1g/L AF647 solution in DMSO was added drop wise and in the dark to the nanoparticles dispersion. Reaction was continued under stirring and in the dark overnight. Nanoparticles were purified by 3 centrifugation cycles at 20,900g during 30 min and they were finally redispersed in 1 mL of PBS 1X (pH = 7.4).

5.2.1.4 Synthesis of CS2 GNPs

In a first step, 500 μ L of the previously prepared gold-silica nanoparticles were centrifuged at 7700g during 30 min. The supernatant was discarded and nanoparticles were dispersed in 500 μ L of DMSO using sonication. Then 500 μ L of sodium tetraborate buffer (pH = 8.5) was added drop wise under stirring. Nanoparticles were then centrifuged twice during 10 s at

20900g. The colorless supernatant was discarded and the precipitate was redispersed in 500 μL of DMSO. 0.5 μL of a 1g/L AF647 solution was added drop wise under stirring. The reaction was continued overnight in the dark. Nanoparticles were purified by centrifugation at 15000g during 15 min. The colorless supernatant was discarded. Then 942 μL of ethanol and 58 μL of ammonia solution (30%wt) were added. Four successive additions (4x1.1 μL) of a 4.5 mM TEOS solution in ethanol were done under stirring. The reaction was then continued during 4 h. Finally, nanoparticles were purified by 3 centrifugations at 15,000g during 15 min in PBS 1X (pH = 7.4).

5.2.1.5 Characterization of fluorescent gold nanoparticles by FCS

Scanning Electron Microscopy

SEM images were obtained with a MIRA3 Tescan microscope. For SEM, samples were prepared by deposition of 1 μL of the nanoparticles dispersion on a silicon wafer substrate. ImageJ 1.40 g software was used for image analysis. UV–visible absorption spectra were recorded on a SAFAS UV mc2 double beam spectrophotometer.

Fluorescence Correlation Spectroscopy

Our experimental set-up, is based on an inverted microscope with a NA= 1.2 water- immersion objective. For FCS measurements, the excitation is set to a CW HeNe laser operating at 633 nm. After a 50 μm confocal pinhole conjugated to the sample plane, the detection was performed by two avalanche photodiodes (Perkin-Elmer SPCM-AQR-14, Canada) with 670 \pm 20 nm fluorescence bandpass filters (Chroma filters). The fluorescence intensity fluctuations were analyzed by cross-correlating the signal of each photodiode with a hardware correlator (ALV7004, ALV-Laser Vertriebsgesellschaft m.b.H. Germany). Each individual FCS measurement was obtained by averaging 5 runs of 10 s duration.

5.2.2 Results and discussion

5.2.2.1 Nanoparticles characterization before fluorophores conjugation

A first silica layer was formed onto 20 nm gold nanoparticles using Liz-Marzan process⁹⁹. This first layer was aimed at obtaining a controlled distance between gold core and AF647 molecules for optimal MEF effect. As shown in **Figure 38 a**, the obtained gold-silica nanoparticles exhibit a core-shell structure with a well-control diameter. Size histogram presented in **Figure 38 b**, was obtained on 100 nanoparticles. It showed a very narrow size

distribution, with a mean diameter of 41 ± 3 nm so the size dispersion was lower than 10%. Thus the thickness of this first silica layer was estimated around 10 nm. The zeta potential of gold-silica nanoparticles was measured at -22.6 mV.

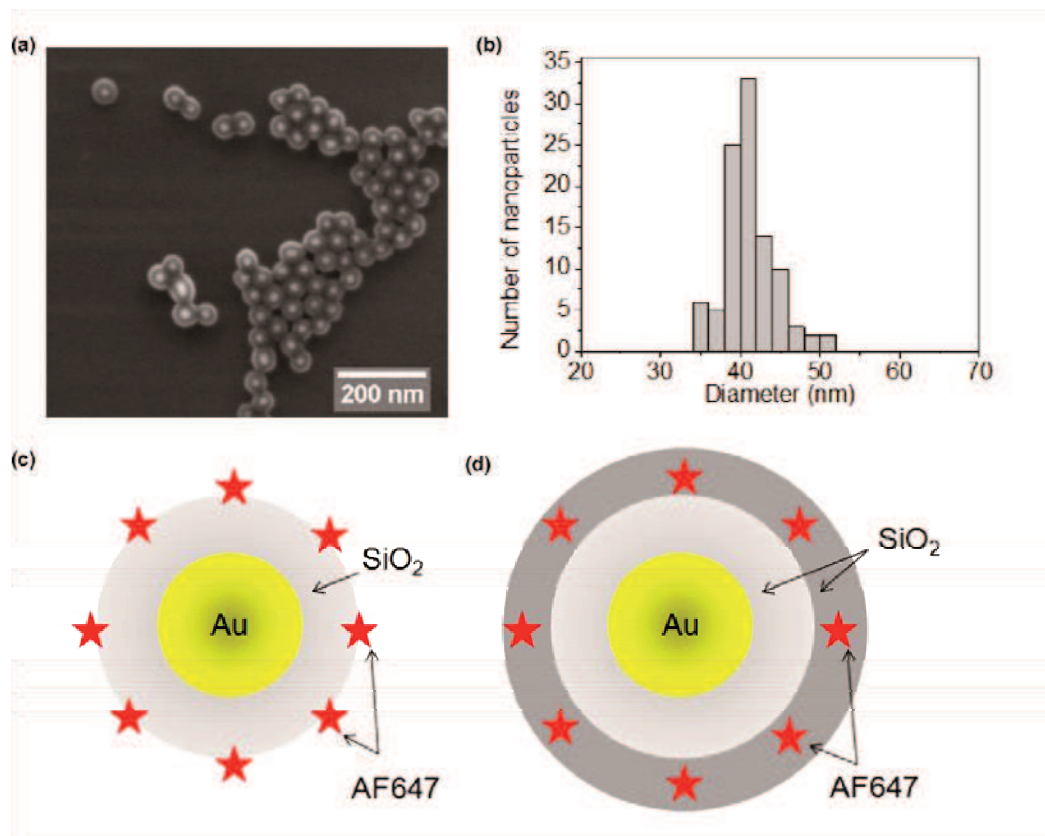


Figure 38. (a) SEM image and (b) corresponding size histogram of gold-silica core-shell nanoparticles. Scheme of the structure of (c) CS1 and (d) CS2 GNPs.

After amino functionalization, the value became +20.1 mV, which proves that silica surface was chemically modified. For CS1 GNPs, the fluorophore was directly grafted onto amino groups through the NHS-ester functions of AF647 molecules (**Figure 38 c**). Concerning CS2 GNPs, AF647 was incorporated during the second silica shell synthesis (**Figure 38 d**). Unfortunately, the SEM resolution was too poor to measure any significant increase in the nanoparticles diameter. However, the success of the second silica shell growth can be checked by following the evolution of the nanoparticles dispersion on UV-visible absorption spectra (**Figure 39**). The maximum extinction of as-synthesized GNPs was at 524 nm (**Figure 39**, black solid curve). After the growth of the first silica shell, the maximum was shifted to 531 nm (**Figure 39**, grey dash curve). This red-shift with respect to bare GNPs was due to the increase in local refractive index around the gold core induced by the coated silica shell ⁸⁵.

The subsequent synthesis of CS2 GNPs involved the formation of an AF647-doped silica layer over gold-silica nanoparticles.

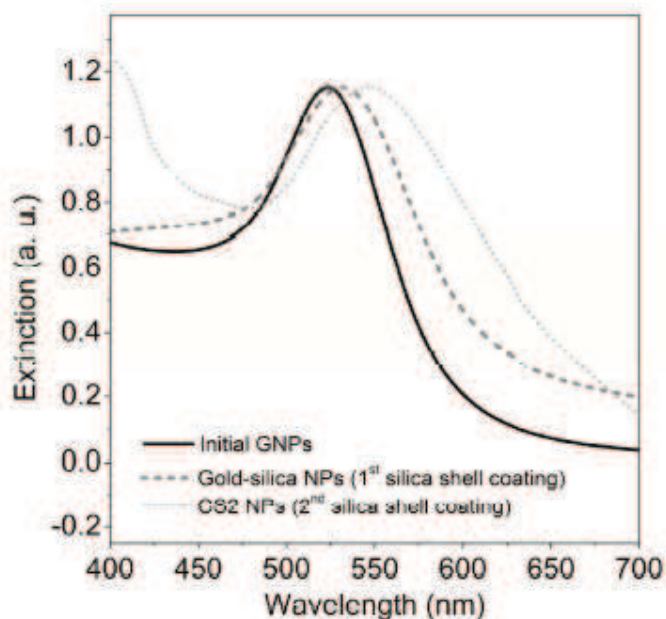


Figure 39. Normalized extinction spectra of initial 20 nm GNPs (black solid line), after first silica shell coating (grey dash line) and after second silica shell coating (grey dot line).

This induced a new red-shift of the maximum to 547 nm associated to an enlargement of the plasmon band (**Figure 39**, grey dot curve). This effect could be attributed both to the growth of a new silica shell and to the presence of AF647 molecules, whose absorption band contributes to the enlargement of the Plasmon band in the high wavelength range.

5.2.2.2 FCS characterization of Alexa fluor conjugated core-shell gold-silica nanoparticles

FCS spectroscopy was performed on a home-built confocal sample-scanning microscope as shown in **Figure 40 a**. The analysis of this FCS data relies on a numerical fit based on a three dimensional Brownian diffusion model:¹⁰⁰

$$G(\tau) = 1 + \frac{1}{N} \left[1 + n_T \exp\left(-\frac{\tau}{\tau_T}\right) \right] \frac{1}{1 + \frac{\tau}{\tau_D}} \frac{1}{\sqrt{1 + s^2 \frac{\tau}{\tau_D}}}$$

where N is the total number of molecules, n_T the amplitude of the dark state population, τ_T the dark state blinking time and s the ratio of transversal to axial dimensions of the analysis volume ($s = 0.2$ in our experiments). Numerical fit of the FCS data following Equation 1 provides the average number of molecules N in the observation volume and the lateral diffusion time τ_D that corresponds to the time a molecule stays in the focal volume. This latter

parameter is related to both the diffusion constant (D) and the hydrodynamic radius (R_h) of the molecules that are obtained with the following Equations:^{57, 101}

$$\tau_D = \frac{\omega_{xy}^2}{4D}$$

$$D = \frac{kT}{6\pi\eta R_h}$$

Where ω_{xy} is the radius of the observation volume considered generally as a three dimensional Gaussian intensity profile, in this system ω_{xy} is 370 nm (calibrated from **Figure 40 c**). η is the solvent viscosity, k the Boltzmann constant and T is the temperature (all measurements were done at room temperature 25 °C). **Figure 40 c** presents typical correlogram $G(\tau)$ recorded in a 10 nM AF647 in water solution at 200 μ W excitation power.

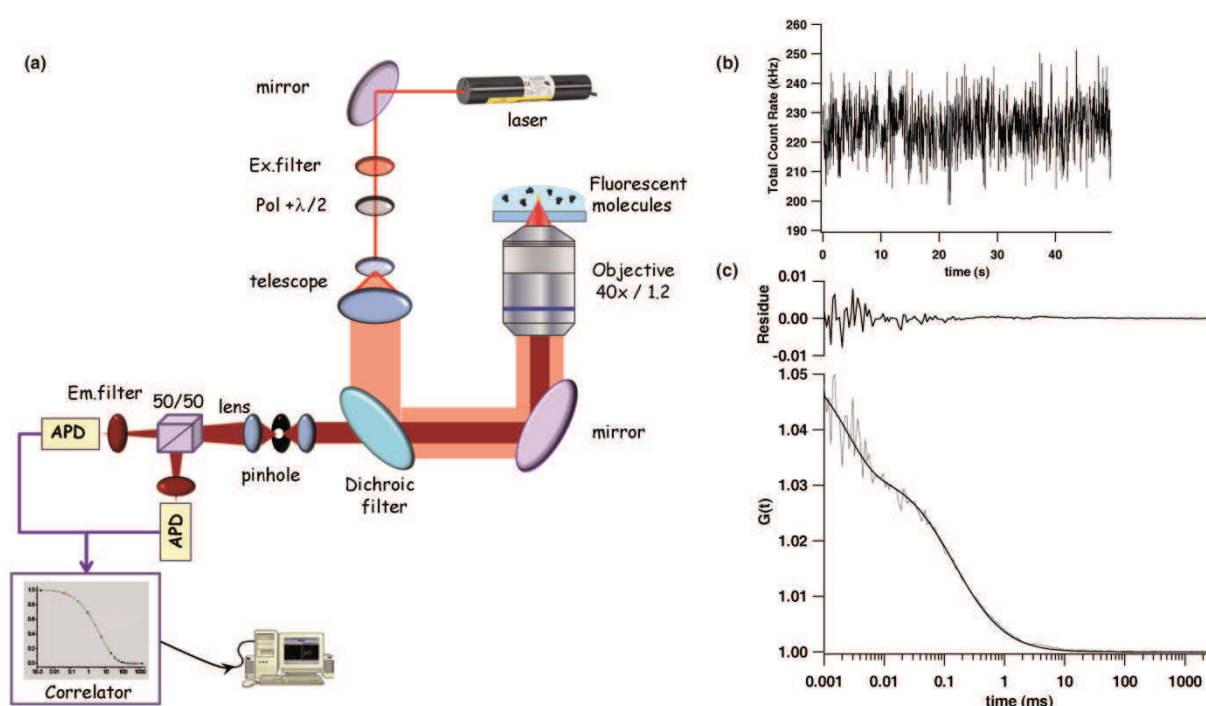


Figure 40. (a) Schematic view of the FCS experimental setup. (b) Time dependent fluorescence intensity of free AF647 molecules measured in water at 10 nM concentration and excited at 200 μ W laser power. (c) Typical fluorescence autocorrelation of free AF647 molecules. The fitting curve using equation (1) gives a typical time diffusion $\tau_D = 140 \mu$ s and $N \sim 30$ of free AF647 molecules in the observation volume.

Figure 41 shows fluorescence cross-correlation trace collected for 50 s of CS1 GNPs. This cross-correlation reveals the three dimensional diffusion of CS1 and measures its diffusion times (τ_D), in optically defined focal volume. Conventional single component fitting of cross-correlation data leads to a diffusion time of 3 ms which corresponds to a calculated diffusion coefficient of CS1 around $11.4 \times 10^{-12} \text{ m}^2\text{s}^{-1}$. Hence, a hydrodynamic diameter of $\sim 39 \pm 9 \text{ nm}$ was calculated from 2nd and 3rd equations, which is in agreement with the value obtained from SEM analysis ($\sim 41 \pm 3 \text{ nm}$). Thus, the hydrodynamic radius obtained from FCS paves the important utility of FCS for the determination of the exact size of this kind of core-shell colloidal nanoparticles which is consistent with other studies.^{102, 103}

Figure 41 b shows fluorescence time trace recorded on CS1 GNPs. Bursts of fluorescence can be observed. These bursts were neither observed for gold-silica nanoparticles in the absence of AF647 molecules nor in the fluorescence time traces of free AF647 molecules (see **Figure 40 b**). The bursts arrived most probably due to the aggregated fluorescent GNPs through the confocal volume.

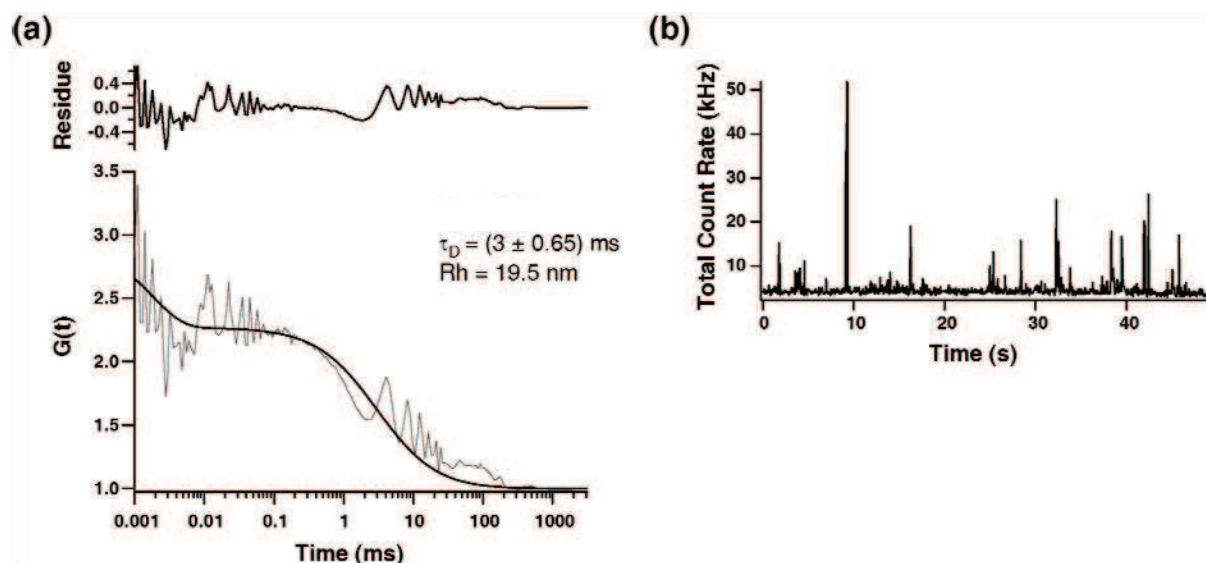


Figure 41. (a) Cross-correlation curve obtained by measuring CS1 GNPs in water and resultant fitting (upper panel shows the residual plot). (b) Total count rate of fluorescence intensity of CS1 recorded by the detectors at $200 \mu\text{W}$ excitation power.

The addition of silica layer on the CS GNPs improves strongly the photo stability of the dye molecules⁹³. From cross-correlation fitting (**Figure 42 a**), we obtain a diffusion time of 3.87 ms which corresponds to the hydrodynamic radius $\sim 51 \pm 5 \text{ nm}$ of CS2 GNP, which is in agreement with the growth of a second silica shell, as shown in **Figure 39**. The calculated

diffusion coefficient of CS2 GNPs is $\sim 8.85 \times 10^{-12} \text{ m}^2\text{s}^{-1}$ which is consistent with other works¹⁰². The count rate showing bursts (in *Figure 42 b*) have the same explanation as the CS1 GNPs.

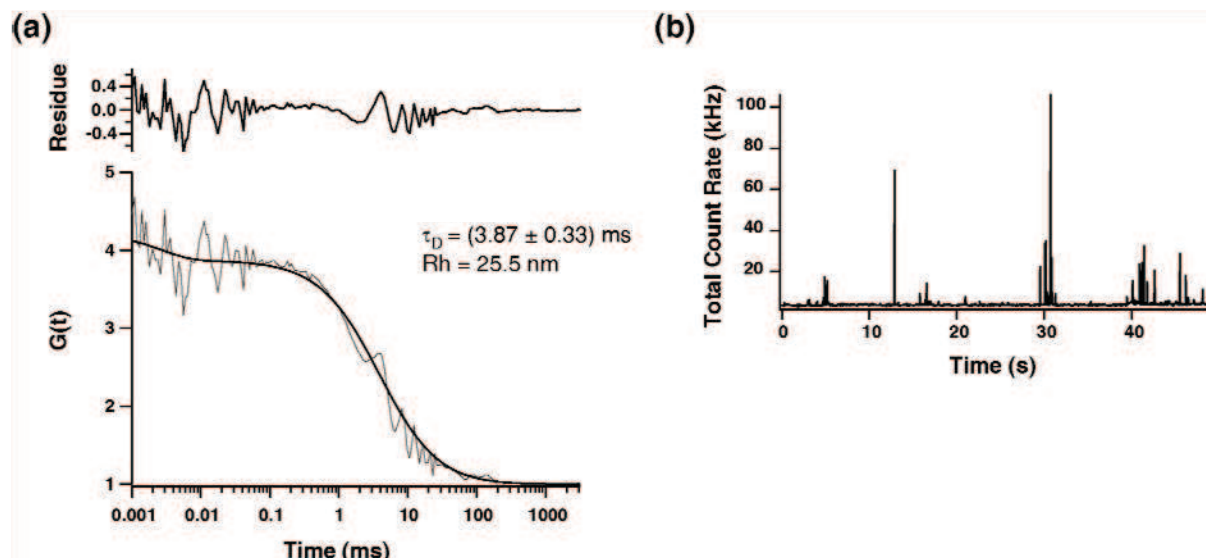


Figure 42. (a) Cross-correlation curve obtained by measuring CS2 GNPs in water and resultant fitting (upper panel shows the residual plot). (b) Total count rate of fluorescence intensity of CS2 recorded by the detectors at 200 μW excitation power.

The diameters of both CS1 and CS2 samples were determined by both electron microscopy imaging (SEM) and further compared by the results determined using FCS in *Table 4*.

Table 4. A comparison of CS GNPs sizes obtained by SEM and FCS study.

GNPs	Diffusion time, τ_D (ms)	Diffusion coefficient, D (m^2s^{-1})	CS GNPs sizes (nm)	
			Average diameter obtained from FCS, R_h (nm)	Average diameter obtained from SEM (nm)
CS1	3 ± 0.65	11.4×10^{-12}	39 ± 9	41 ± 3
CS2	3.87 ± 0.33	8.85×10^{-12}	51 ± 5	X

We further characterized CS1 GNP samples by illuminating these particles at different excitation powers. The fitted cross-correlation curves recorded from CS1 GNPs at different

excitation powers reveals a decrease of the diffusion time (τ_D) when the excitation power is increased (see **Figure 43 a**). This time corresponds to the average width of the fluorescence burst and hence the average time that individual CS1 GNPs spend in the focal volume before fluorescence quenching.

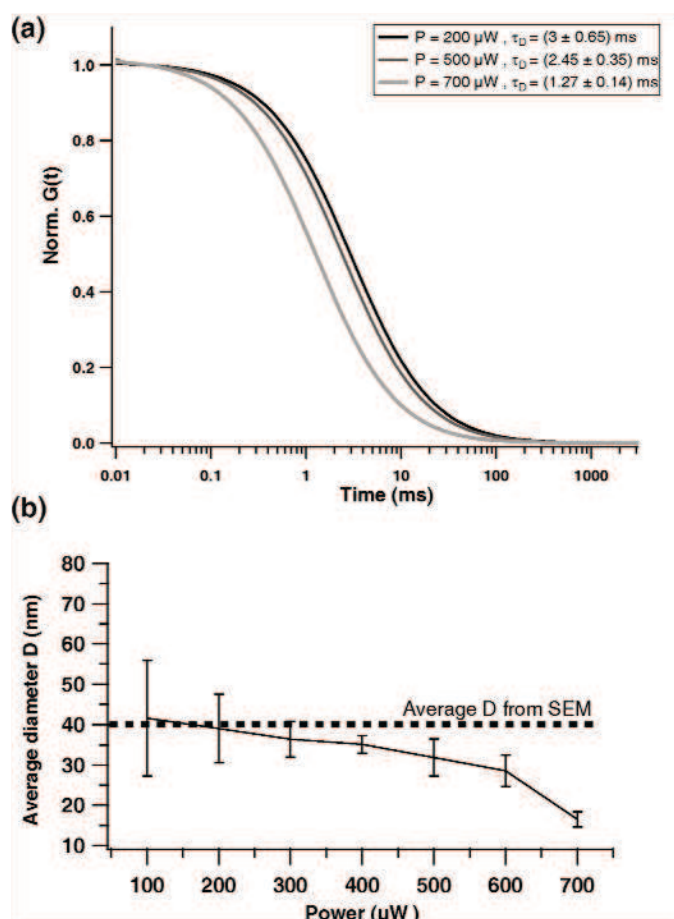


Figure 43. (a) Normalized Cross-correlation fitting curves obtained by measuring CS1 GNPs in water at three different excitation powers: 200 μW (before high bleaching), 500 μW (at the optimal excitation value) and 700 μW (at high bleaching level). (b) The hydrodynamic diameters calculated from FCS (τ_D) for CS1 GNPs at different excitation powers.

This quenching mechanism results in fluorescence bursts which depend on the excitation laser power and GNP structure⁹⁶. In this case, the calculated hydrodynamic radius is progressively distorted by the increased excitation power due to the bleaching effect (**Figure 43. b**).

FCS characterization of nanoparticle based on their size or diameter were performed successfully for both CS1 and CS2 core-shell gold-silica nanoparticles. These results were in agreement with the electron microscopic characterization just after their fictionalization. Fluorophores conjugated nanoparticles thus can be used as probe in medical therapy and/or imaging

6. Fluorescence diffusion dynamics in the context of GNP nanotoxicity

Summary:

6.1 Mitochondrial fluorophores diffusion and membrane potential in the context of cytotoxicity

6.2 Study of the mitochondrial diffusion by FCS

6.3 Preliminary results in nanotoxicity

In the previous chapter, the analysis of the single fluorescent nanoparticle by FCS along with the sensitivity of the set-up was verified. According to the work plan of this thesis work, the next manipulation should involve analysis of the effect of fluorescent GNPs in the cellular environment. Here, we first aimed to analyse the diffusion of mitochondrial fluorophores when cells are incubated with GNPs. The reason of the choice of these cell organelles and the possible consequences of GNP incubation on mitochondria are described in detail below:

6.1 Mitochondrial fluorophore diffusion and membrane potential in the context of cytotoxicity

Cell cytoplasm is highly structured with micrometer and nanometer scale organelles. Molecular interactions, like binding or influence of obstacles can modify the function of cellular organelles¹⁰⁴, especially mitochondria. Nanoparticles with a radius >25–30 nm can diffuse inside cytoplasm but this diffusion is limited since the diffusional mobility in the cytoplasm strongly decreases with an increasing radius¹⁰⁵. On the other hand, GNPs smaller than this diameter have a possibility of entering inside cell cytoplasm and can show several effects on the cells. GNPs cause plasma membrane depolarization, allowing Ca²⁺ influx into the cells. In healthy cells, elevated Ca²⁺ level is normally buffered by mitochondria and regulated by MICU1 (regulator of mitochondrial calcium uniporter), which also has an anti-apoptotic role¹⁰⁶.

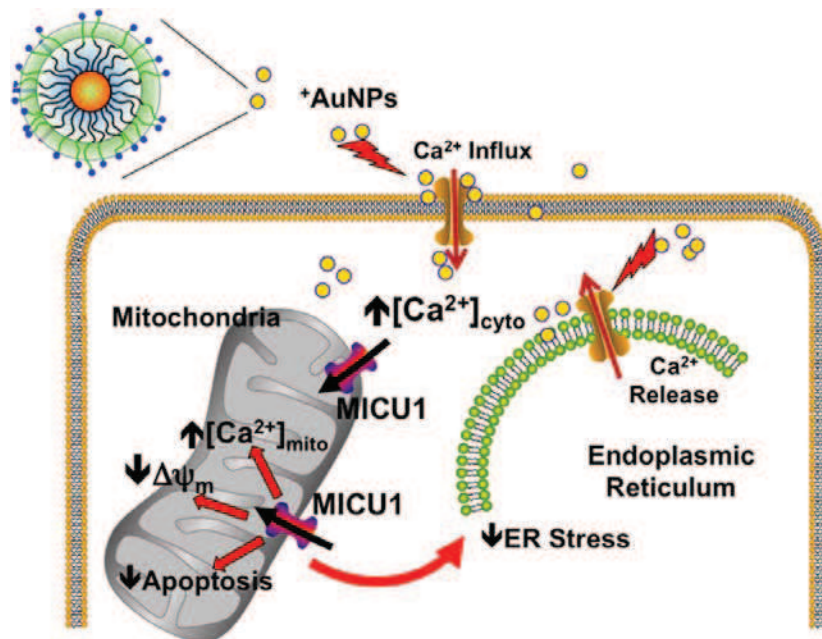


Figure 44. Role of the mitochondrial uniporter regulator in buffering Ca^{2+} influx induced by GNPs due to plasma membrane depolarization and cytotoxic stress¹⁰⁶.

Separately, MICU1 protein may normally prevent endoplasmic reticulum (ER) stress such as that induced by GNPs. It interacts with the mitochondrial calcium uniporter, a mitochondrial inner membrane Ca^{2+} channel which is essential in preventing mitochondrial Ca^{2+} overload. Mitochondrial Ca^{2+} overload can cause excessive production of reactive oxygen species, and as a consequence induces causes alterations in the expression or dysfunction of mitochondrial Ca^{2+} regulatory mechanisms. This can have profound cellular effects causing mitochondrial and ER stress leading to apoptic cell death. Here, the link between high levels of $[\text{Ca}^{2+}]_{\text{mito}}$ and apoptosis are well established¹⁰⁶. GNPs elevate $[\text{Ca}^{2+}]$ by stimulating plasma membrane Ca^{2+} influx and ER Ca^{2+} release. On the other hand, enhanced ionic state inside cells can induce H_2O_2 production in mitochondria, which upon reaction release free radicals (**Figure 44**).

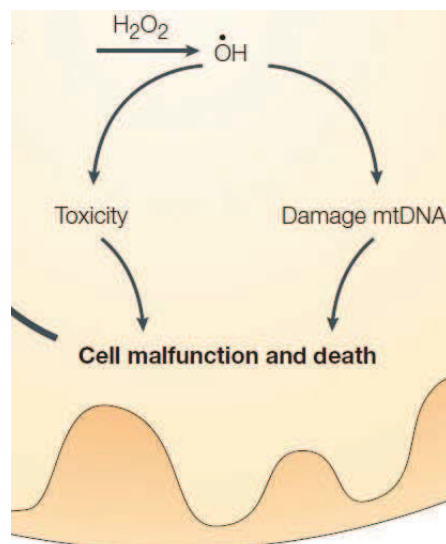


Figure 45. Effect of increased free radicals on mitochondria and cell death¹⁰⁶.

This free radicals of OH[•] causes toxicity to the mitochondria inducing mitochondrial DNA damage and the final result is cell malfunction and/or cell death (**Figure 45**)¹⁰⁷. So, the mitochondrion is a very important cell organelle determining apoptosis in cells induced by GNPs, thus the study of GNPs effect on this cellular organelle is very interesting in disclosing cytotoxicity phenomena.

6.2 Study of the mitochondrial diffusion by FCS

Mitochondrion is well known to be highly mobile inside cell cytoplasm in spite of their complex structure. Their dynamics is essential for functional integrity of the cell organelles and thus for the cell viability¹⁰⁸. For example, in order to share all the components within a chondriome, mitochondrion performs fusion and fission or either of the two events¹⁰⁹. Thus in healthy cells, they are diffusing their components through organelle dynamics at a short temporal time range. In this context, FCS can be a promising tool in determining GNPs effect on mitochondrial dynamics. The biggest advantage of FCS is its high temporal resolution. It can easily capture millisecond range phenomena, in particular transient confinements, which are difficult to study with other techniques.

Yasutomo Nomura *et al.* have discussed the evaluation of mitochondrial DNA dynamics using FCS¹¹⁰. They focused on the estimation of vulnerability of mitochondrial DNA (mtDNA) due to external toxic stress. In order to estimate the vulnerability of mtDNA to oxidative stress using FCS, the complete mtDNA genome isolated from the cells exposed to H₂O₂ was amplified by long PCR and the product (~17 kbp) was fluorescently labeled with an

intercalating dye YOYO-1. As shown in **Figure 46 A**, normalized autocorrelation function of long PCR for mtDNA product was shifted to the left with the increment of H_2O_2 concentration and a decrease in the slow component due to mtDNA damage was revealed. In further study, they quantified size distribution of restriction fragments in long PCR product for mtDNA with Hga I and Hae III restriction enzymes in **Figure 46 B**, which indicated changes in molecular number due to fragmentation. The amplitude measured by FCS would be a very useful index for primary screening for alterations in the entire mitochondrial genome using restriction enzymes that have several polymorphic restriction sites.

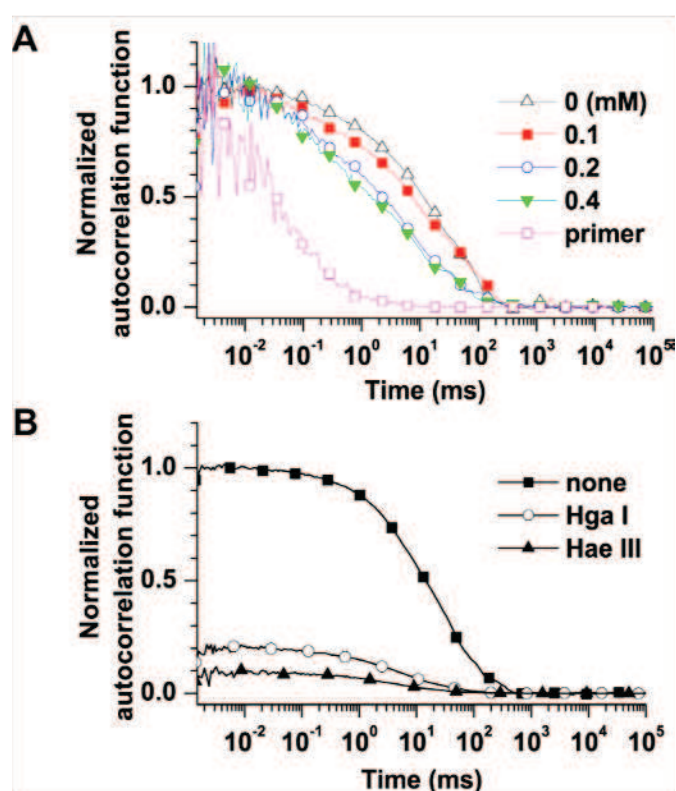


Figure 46: Fluorescence correlation analysis of mtDNA damage in vitro. (A) Changes in normalized autocorrelation functions of long PCR products (~17 kbp) for mtDNA isolated from the cells and exposed to H_2O_2 (from 0 to 0.4 mM). For comparison, normalized autocorrelation function of primer is also shown. A decrease in fraction of slow-moving components (long PCR products) shifted the normalized autocorrelation function to the left hand side. (B) Effect of the restriction digestion on the normalized autocorrelation function of long PCR products for mtDNA. An increase in fluorescent molecules due to the fragmentation resulted in the decrease in amplitude of the autocorrelation function¹¹⁰.

This study proves that any external toxicity exerts stress on mitochondria and it can be detected using the technique FCS through the mtDNA diffusion. There is another way to detect the stress on mitochondria besides their DNA breakage, which is alteration in mitochondrial spontaneous diffusion inside cells. Any toxic stress can cause anomaly in the phenomenal fusion or fission of mitochondria thus, the diffusion behaviour may have been changed. In my thesis study we decided to focus on the anomaly in mitochondrial function due to the stress induced by GNPs incubated with the cells. In order to do this, it is important to study mitochondrial function by FCS in the control cells, which means without incubation

with GNPs. Then after the incubation with GNPs, the comparative mitochondrial diffusion would be conclusive in the context of cytotoxicity.

6.3 Preliminary results in nanotoxicity

For observation of mitochondria with FCS, the organelles were labeled using MitoTracker Deep Red FM dye (Molecular Probes, Invitrogen, France). To label mitochondria, cells were simply incubated with MitoTracker probes, which passively diffuse across the plasma membrane and accumulate in functional mitochondria. In detail, cells were grown on round cover slips (25 mm diameter) inside a Petri dish filled with the appropriate culture medium and at cells growth condition. When cells reached the desired confluency, the media was removed from the dish and pre-warmed (37°C) staining solution containing MitoTracker probe (30 nM) were added. After incubation for 45 minutes under cells growth conditions, the staining solution was replaced with fresh pre-warmed PBS buffer followed by 3 wash with warm PBS buffer. Fixing the cover slips inside appropriate sample holder, observation was done in FCS. The MitoTracker dye has excitation/emission at 644/665 nm. Thus we have used laser wavelength of 633 nm.

After laying the sample including the sample holder over the microscope objective on a piezo stage, the sample was illuminated with 80 μ W laser coming through the objective. The initial step is to locate the mitochondrial position before performing the study. With the help of the piezo stage, the sample was moved along the laser probe and thus, part of the sample (cells) was raster scanned to take image. **Figure 47** is an example of an image of a mitochondrion of 2.5 μ m long and 2 μ m wide. After focusing on the appropriate part on the mitochondrial body (membrane or inside the organelle), diffusion study were performed at several minutes intervals. Each measurement is the average of 5 runs on a specific place at a certain moment (**Figure 48**). We follow the diffusion of the Mitotracker dye when incorporated inside the mitochondria. Thus to compare the diffusion time with free MitoTracker dye, a separate study was done with the dye dissolved in PBS buffer (**Figure 48 a**).

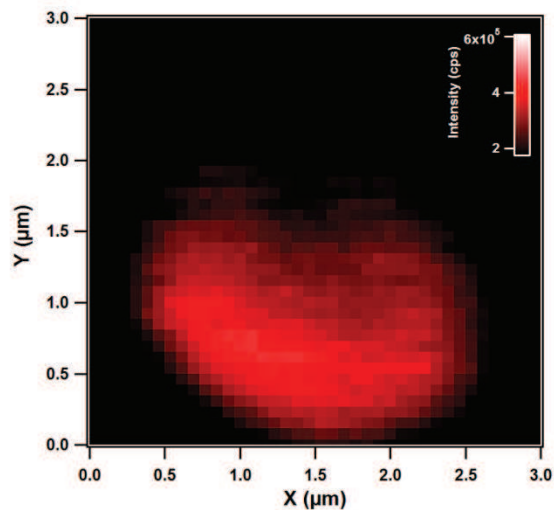


Figure 47. Fluorescent image of a mitochondrion by scanning the sample over laser probe over a surface area of $3 \mu\text{m} \times 3 \mu\text{m}$

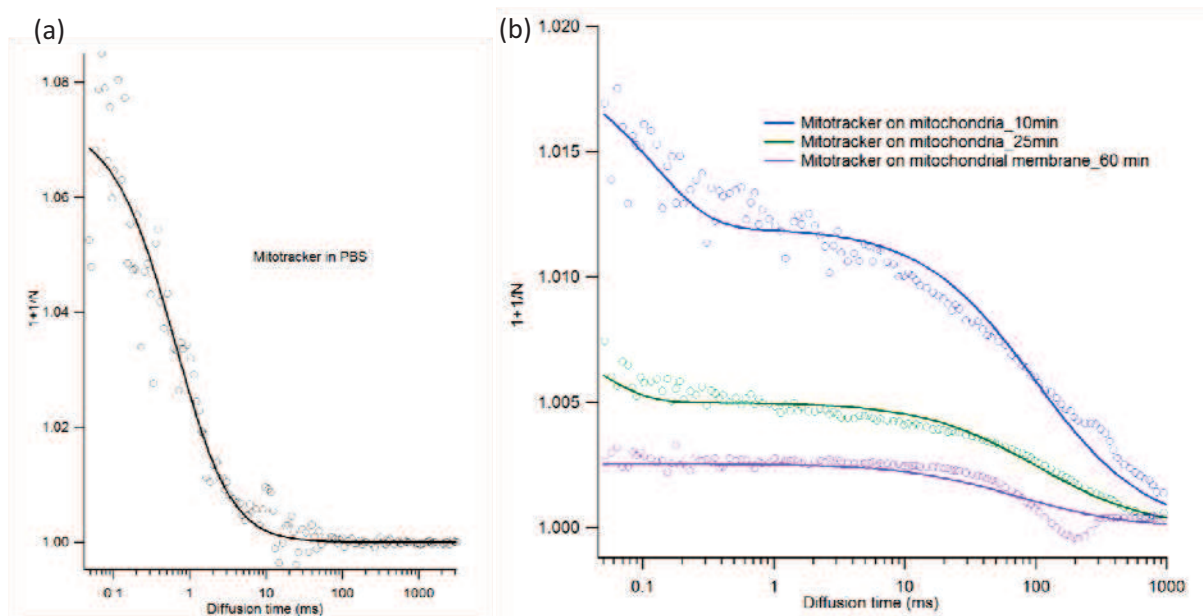


Figure 48. Diffusion of MitoTracker Deep Red FM dye in PBS solution (a) and of fluorescent mitochondria after incubation of mitochondria with MitoTracker Deep Red FM dye (b).

We used fluorescence correlation spectroscopy to determine the diffusion characteristics of a fluorescent dye of the mitochondria in the absence of the GNPs (**Figure 48 b**). The FCS diffusion times were obtained by fitting the cross-correlation curves and are shown in **Table 5**.

Table 5. Parameters of mitochondrial diffusion determined using FCS

	Number of molecules, N	Diffusion time, τ (ms)
MitoTracker in PBS	11	0.37
Mitochondrial matrix at 10 min	83	89.26
Mitochondrial matrix at 25 min	200	102
Mitochondrial membrane at 60 min	405	75.5

From the correlation curves, it is easily deductible that MitoTracker in mitochondria have largely higher diffusion time compared to the dye itself diffusing freely in PBS solution (0.37 ms). At the same concentration of 30 nM, the free solution contained 11 molecules, while with the increase of the incubation time, the number of molecules inside the mitochondria increased. Thus after incubation time of 10, 25 and 60 min, values of N increased from 83 to 405. At the point of 10 and 25 min of incubation, since measurement was done on mitochondrial body where more dye was accumulated with the enhancement in the diffusion time from 89 to 102 ms. At 60 min, though the number of molecules N figured the highest value among all, the diffusion time was lower than the ones performed on the mitochondrial body. The difference can be linked to the position in mitochondria. Our hypothesis is that the dye molecules can diffuse easily and rapidly by the pores in the membrane of the mitochondria until saturation up to high concentration. Once inside the mitochondria, the dye molecules cannot move easily because of its higher saturated concentration compared to the outer membrane of the mitochondria where it has free passage of entry (*Figure 49*).

Through membrane, mitotracker diffuses
in: faster movement, τ_D decrease



Mitotracker saturated inside:
slower movement, τ_D increase

Figure 49. A schematic representation of MitoTracker diffusion in the body and along the membrane of the mitochondrion

Now the question that arise are why MitoTracker diffuses in and/or out of the mitochondria and what are the possible phenomena occurring if external toxicant may exert stress on the mitochondria. The mechanism behind the labeling of mitochondria with the fluorescent dye lies behind the ionic states of both mitochondria and the dye. This MitoTracker dye is cationic in nature. Mitochondrial inner membrane matrix has negative potential though inter-membrane space is positively charged. As a consequence of the high charge difference (Mitochondrial membrane potential, $\Delta\psi_m$) between the mitochondrial matrix and the cytosol or inter-membrane space of mitochondria, the cationic dye molecules are facilitated to diffuse fast inside the mitochondrial matrix (scheme in **Figure 50**).

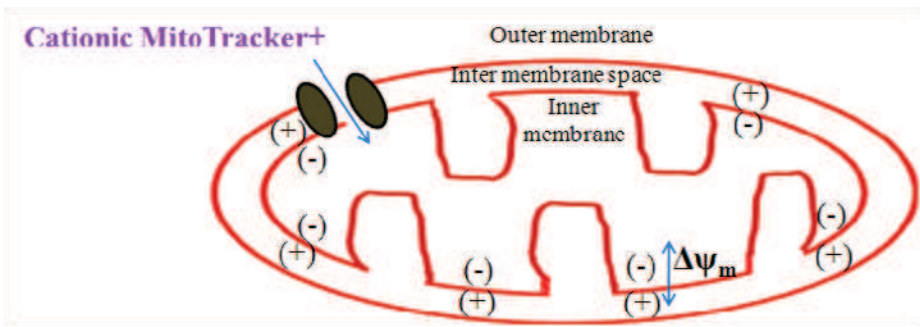


Figure 50. The ionic states of the dye molecule and mitochondria potential demonstrating schematically the diffusion of the dye in and out of mitochondria.

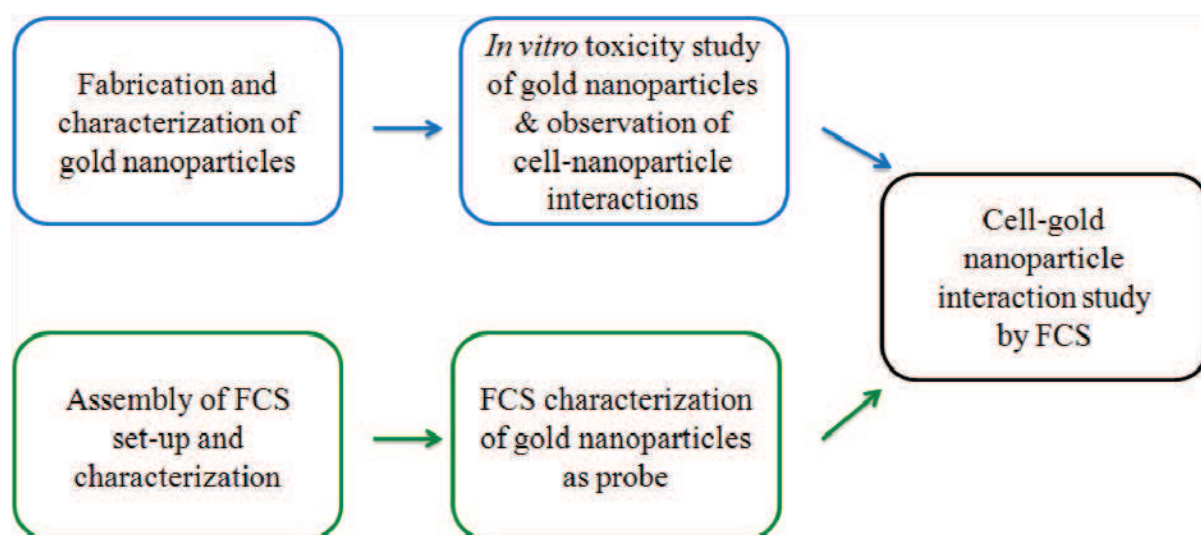
As explained in the section 6.2 in this chapter, GNPs toxicity may induce positive Ca^{2+} ion efflux in mitochondrial matrix causing the value of $\Delta\psi_m$ tends to zero whereas in healthy cells

for active mitochondria this value is 120 mV¹¹¹. Since the mitochondrial Ca²⁺ overload and reactive oxygen species have been known to highly dissipate $\Delta\psi_m$ ¹¹². Thus these cationic stains are easily washed out of cells once the mitochondria loss membrane potential. This characteristic can be exploited in experiments of cytotoxicity since it is correlated with the affect of the energetic state of the mitochondria. We can assume that, due to the loss of mitochondrial membrane potential when the dye molecules will be diffuse out of the mitochondria very fast, in the early stage of GNPs incubation we will be able to see lower diffusion hence and lower values of diffusion time for GNPs treated cells.

It can be assumed further that, unlike the control cells where the number of molecules increase with the higher incubation times, in GNPs treated cells we may see the opposite incidence due to the stains diffusing out of mitochondria. Though in this thesis work, only healthy cells were treated to draw a conclusion for fluorophore diffusion properties through/inside healthy mitochondria but cytotoxic effects due to GNPs treatments were not observed, we would like to keep this part for the future work of this group. The mechanism of apoptotic effects on mitochondrial membrane potential and the diffusion properties of the cationic dye molecules observed until now will give the basis of the future studies of GNPs toxicity on cells using FCS.

Conclusion

The objective of this thesis was to exploit the radiative properties of metal nanoparticles (here gold nanoparticles, GNPs) in order to study their toxicity at various scales and at sub-nano molar concentration. This thesis work has not only provided an assessment of the toxicity of the GNPs depending on the different parameters, but also demonstrated a comprehensive study of their interaction with biological media (here cellular environment). The thesis work aimed to understand how properties in GNPs influence bio-accumulation / cytotoxicity and thus required to provide a predictive model to assess the toxicity of GNPs according to their nature, size, concentration and surface chemistry.



From the above scheme, we can make the work summary of this thesis, which is:

1. the multiparametric assessments of *in vitro* cytotoxicity of different GNP samples
2. the installation of the assembly of Fluorescence Correlation Spectroscopy (FCS) and the system characterization
3. the study of the dynamics of fluorescence based metal nanoparticles by FCS technique
4. dynamic measurement of interaction of nanoparticle /cell organelles by FCS which is the melting point of the above works and is discussed in the final chapter.

According to the plan and organization of the work of this thesis work, the beginning was to diagnose the cytotoxicity of the nanoparticles *in vitro* in cellular environment. Cytotoxicity study was performed in detail on human endothelial cell HUVEC starting from viability assay and changes in cell proliferation rate until effects on cell organelles. In order to compare the viability behaviour of these nanoparticles *in vitro* with another cell line other than HUVEC, a human leukemia cell K562 has been chosen. Thus the toxicity of GNPs was compared between healthy or normal cell HUVEC and cancerous cell K562. It has been found that cancer cell is more resistant to the toxic effects of the gold nanoparticle samples than normal cell HUVEC.

After determining cell viability, cell proliferation rate, nanoparticle internalization inside cell cytoplasm by dark field microscopy and spreading test were performed by incubating 6 different GNPs (mentioned in chapter 4) with HUVEC. We showed that increasing concentration of nanoparticles decreased cell viability; and thus we determined the threshold of toxic concentration to be around 100 pM, 10 pM and 0.5 pM consecutively for 50-a-GNSs, 15-a-GNSs and a-GNFs (a-GNP is as prepared GNPs). We calculated the cell proliferation rate from the result of Flow Cytometry analysis which demonstrated the more deleterious effect of GNPs over GNSs. We noticed more affinity of GNPs on HUVEC than 15-GNSs, where 50-GNSs had the least affinity. We were able to compare the degree of cytotoxic effect and demonstrated that it is largely higher for GNPs than for GNSs.

The next work was to make optical assembly and set-up of the Fluorescence Correlation Spectroscopy (FCS). This set-up was built-up by my co-supervisor Nadia Djaker and me. Followed by the set-up of the system, I performed detailed characterization of the system under her supervision. The sensitivity, resolution and important parameters were determined during the characterization procedure. Then FCS was used to characterize fluorescent molecule-conjugated nanoparticles. We have conjugated Streptavidin-Alexa 633 fluorescent protein with GNPs and then characterize the fluorescent GNPs to ensure successful conjugation of fluorescent protein. This experiment gave detailed information on the diffusion property, hydrodynamic diameter and count rate per molecule CRM signifying fluorescence enhancement factor of the metal nanoparticles. Based on the comparative diffusion time of each species passing through the confocal volume, it was assumed the size distribution of those fluorescent species. After addition of each molecule along with the alexa 633 NHS, there was an increase in diffusion time from 0.2 ms until 94 ms when Streptavidin-Alexa 633

was conjugated to gold nanoparticle surface. Count rate per molecule CRM gave the idea of fluorescent emission from each molecule and finally in a comparable manner we could also make a conclusion that upon addition of Alexa 633 on GNP surface, there was an enhancement of 13 time of fluorescence emission which proves the successful probe design based on metal enhanced fluorescence (MEF) effects. Thus the successful characterization of functionalized gold nanoparticles was done by FCS.

Bibliography:

1. Académie des Sciences and Académie des Technologies, Science and technology (patent). 2004.
2. Hansen, S. F.; Larsen, B. H.; Olsen, S. I.; Baun, A., Categorization framework to aid hazard identification of nanomaterials. *Nanotoxicology* 2007, 1, 243-250.
3. Nanoscale Science Engineering and Technology Subcommittee, The national nanotechnology initiative: strategic plan (patent). 2004.
4. Horikashi, S.; Serpone, N., Introduction to Nanoparticles. Wiley-VCH: pp 1-24.
5. Alkilany, A. M.; Lohse, S. E.; Murphy, C. J., The Gold Standard: Gold Nanoparticle Libraries To Understand the Nano–Bio Interface. *Accounts of Chemical Research* 2012, 46, 650-661.
6. Cai, W.; Gao, T.; Hong, H.; Sun, J., Applications of gold nanoparticles in cancer nanotechnology. *Nanotechnol Sci Appl* 2008, 1.
7. Azzazy, H. M. E.; Mansour, M. M. H., In vitro diagnostic prospects of nanoparticles. *Clinica Chimica Acta* 2009, 403, 1-8.
8. Huang, X.; Jain, P. K.; El-Sayed, I. H.; El-Sayed, M. A., Gold nanoparticles: interesting optical properties and recent applications in cancer diagnostics and therapy. *Nanomedicine* 2007, 2, 681-693.
9. Choi, J.; Yang, J.; Bang, D.; Park, J.; Suh, J. S.; Huh, Y. M.; Haam, S., Targetable Gold Nanorods for Epithelial Cancer Therapy Guided by Near-IR Absorption Imaging. *Small* 2012, 8, 746-753.
10. Yong, K.-T.; Swihart, M.; Ding, H.; Prasad, P., Preparation of Gold Nanoparticles and their Applications in Anisotropic Nanoparticle Synthesis and Bioimaging. *Plasmonics* 2009, 4, 79-93.
11. Wang, J.; Zhang, G.; Li, Q.; Jiang, H.; Liu, C.; Amatore, C.; Wang, X., In vivo self-bio-imaging of tumors through in situ biosynthesized fluorescent gold nanoclusters. *Sci Rep* 2013, 3, 1-6.
12. Paciotti, G. F.; Myer, L.; Weinreich, D.; Goia, D.; Pavel, N.; McLaughlin, R. E.; Tamarkin, L., Colloidal gold: A novel nanoparticle vector for tumor directed drug delivery. *Drug Delivery* 2004, 11, 169-183.
13. Salomeh, J.; Devika, B. C., Gold Nanostructures as a Platform for Combinational Therapy in Future Cancer Therapeutics. *Cancers* 2011, 3.
14. Jain, P. K.; Lee, K. S.; El-Sayed, I. H.; El-Sayed, M. A., Calculated Absorption and Scattering Properties of Gold Nanoparticles of Different Size, Shape, and Composition: Applications in Biological Imaging and Biomedicine. *J Phys Chem B* 2006, 110, 7238-7248.
15. Van de Broek, B.; Devoogdt, N.; D'Hollander, A.; Gijs, H.-L.; Jans, K.; Lagae, L.; Muyldermans, S.; Maes, G.; Borghs, G., Specific Cell Targeting with Nanobody Conjugated Branched Gold Nanoparticles for Photothermal Therapy. *ACS Nano* 2011, 5, 4319-4328.
16. Yuan, H.; Khoury, C. G.; Wilson, C. M.; Grant, G. A.; Bennett, A. J.; Vo-Dinh, T., In vivo particle tracking and photothermal ablation using plasmon-resonant gold nanostars. *Nanomedicine: NBM* 2012, 8, 1355-1363.

17. Rodríguez-Lorenzo, L.; Krpetic, Z.; Barbosa, S.; Alvarez-Puebla, R. A.; Liz-Marzán, L. M.; Priore, I. A.; Brustb, M., Intracellular mapping with SERS-encoded gold nanostars. *Integr Biol* 2011, 3, 922-926.
18. Yuan, H.; Fales, A. M.; Khoury, C. G.; Liu, J.; Vo-Dinh, T., Spectral characterization and intracellular detection of Surface-Enhanced Raman Scattering (SERS)-encoded plasmonic gold nanostars. *J Raman Spectrosc* 2013, 44, 234-239.
19. Boca, S.; Rugina, D.; Pinte, A.; Barbu-Tudoran, L.; Astilean, S., Flower-shaped gold nanoparticles: synthesis, characterization and their application as SERS-active tags inside living cells. *Nanotechnology* 2011, 22, 1-7.
20. Sau, T. K.; Rogach, A. L.; Jäckel, F.; Klar, T. A.; Feldmann, J., Properties and Applications of Colloidal Nonspherical Noble Metal Nanoparticles. *Adv Mater* 2010, 22, 1805-1825.
21. Alkilany, A. M.; Nagaria, P. K.; Hexel, C. R.; Shaw, T. J.; Murphy, C. J.; Wyatt, M. D., Cellular Uptake and Cytotoxicity of Gold Nanorods: Molecular Origin of Cytotoxicity and Surface Effects. *Small* 2009, 5, 701-708.
22. Bartczak, D.; Muskens, O. L.; Nitti, S.; Sanchez-Elsner, T.; Millar, T. M.; Kanaras, A. G., Interactions of Human Endothelial Cells with Gold Nanoparticles of Different Morphologies. *Small* 2012, 8, 122-130.
23. Soenen, S. J.; Rivera-Gil, P.; Montenegro, J.-M.; Parak, W. J.; De Smedt, S. C.; Braeckmans, K., Cellular toxicity of inorganic nanoparticles: Common aspects and guidelines for improved nanotoxicity evaluation. *Nano Today* 2011, 6, 446-465.
24. G, O., Safety assessment for nanotechnology and nanomedicine: concepts of nanotoxicology. *Journal of Internal Medicine* 2010, 267, 89-105.
25. Sadik, O. A.; Zhou, A. L.; Kikandi, S.; Du, N.; Wang, Q.; Varner, K., Sensors as tools for quantitation, nanotoxicity and nanomonitoring assessment of engineered nanomaterials. *J Environ Monit* 2009, 11, 1782-800.
26. Connor, E. E.; Mwamuka, J.; Gole, A.; Murphy, C. J.; Wyatt, M. D., Gold nanoparticles are taken up by human cells but do not cause acute cytotoxicity. *Small* 2005, 1, 325-327.
27. Díaz, B.; Sánchez-Espinel, C.; Arruebo, M.; Faro, J.; Miguel, E. d.; Magadán, S.; Yagüe, C.; Fernández-Pacheco, R.; Ibarra, M. R.; Santamaría, J.; González-Fernández, Á., Assessing Methods for Blood Cell Cytotoxic Responses to Inorganic Nanoparticles and Nanoparticle Aggregates. *Small* 2008, 4, 2025-2034.
28. Pan, Y.; Neuss, S.; Leifert, A.; Fischler, M.; Wen, F.; Simon, U.; Schmid, G.; Brandau, W.; Jahnen-Dechent, W., Size-dependent cytotoxicity of gold nanoparticles. *Small* 2007, 3, 1941-1949.
29. Chithrani, B. D.; Ghazani, A. A.; Chan, W. C. W., Determining the Size and Shape Dependence of Gold Nanoparticle Uptake into Mammalian Cells. *Nano Lett* 2006, 6, 662-668.
30. Cui, W. a. L., J. and Zhang, Y. and Rong, H. and Lu, W. and Jiang, L., Effects of aggregation and the surface properties of gold nanoparticles on cytotoxicity and cell growth. *Nanomedicine-nanotechnology Biology And Medicine* 2012, 8, 46-53.
31. Arvizo, R. R.; Rana, S.; Miranda, O. R.; Bhattacharya, R.; Rotello, V. M.; Mukherjee, P., Mechanism of anti-angiogenic property of gold nanoparticles: role of nanoparticle size and surface charge. *Nanomedicine: NBM* 2011, 7, 580-587.

32. Pernodet, N. a. F., X. H. and Sun, Y. and Bakhtina, A. and Ramakrishnan, A. and Sokolov, J. and Ulman, A. and Rafailovich, M., Adverse effects of citrate/gold nanoparticles on human dermal fibroblasts. *Small* 2006, 2, 766-773.
33. Jiang, W.; Kim, B. Y. S.; Rutka, J. T.; Chan, W. C. W., Nanoparticle-mediated cellular response is size-dependent. *Nat. Nanotechnol.* 2008, 3, 145-150.
34. Shukla, R.; Bansal, V.; Chaudhary, M.; Basu, A.; Bhonde, R. R.; Sastry, M., Biocompatibility of Gold Nanoparticles and Their Endocytotic Fate Inside the Cellular Compartment: A Microscopic Overview. *Langmuir* 2005, 21, 10644-10654.
35. Freese, C.; Gibson, M. I.; Klok, H.-A.; Unger, R. E.; Kirkpatrick, C. J., Size- and Coating-Dependent Uptake of Polymer-Coated Gold Nanoparticles in Primary Human Dermal Microvascular Endothelial Cells. *Biomacromolecules* 2012, 13, 1533-1543.
36. Arnida; Malugin, A.; Ghandehari, H., Cellular uptake and toxicity of gold nanoparticles in prostate cancer cells: a comparative study of rods and spheres. *J Appl Toxicol* 2009, 30, 212-217.
37. Niidome, T.; Yamagata, M.; Okamoto, Y.; Akiyama, Y.; Takahashi, H.; Kawano, T.; Katayama, Y.; Niidome, Y., PEG-modified gold nanorods with a stealth character for in vivo applications. *J Controlled Release* 2006, 114, 343-347.
38. Hutter, E. a. B., S. and Labrecque, S. and Lalancette-Hebert, M. and Kriz, J. and Winnik, F. M. and Maysinger, D.; Hutter, E.; Boridy, S.; Labrecque, S.; Lalancette-Hébert, M.; Kriz, J.; Winnik, F. M.; Maysinger, D., Microglial Response to Gold Nanoparticles. *ACS Nano* 2010, 4, 2595-2606.
39. Sironi, L.; Freddi, S.; Caccia, M.; Pozzi, P.; Rossetti, L.; Pallavicini, P.; Donà, A.; Cabrini, E.; Gualtieri, M.; Rivolta, I.; Panariti, A.; D'Alfonso, L.; Collini, M.; Chirico, G., Gold Branched Nanoparticles for Cellular Treatments. *The Journal of Physical Chemistry C* 2012, 116, 18407-18418.
40. Patra, H. K.; Banerjee, S.; Chaudhuri, U.; Lahiri, P.; Dasgupta, A. K., Cell selective response to gold nanoparticles. *Nanomedicine: Nanotechnology, Biology and Medicine* 2007, 3, 111-119.
41. Soenen, S. J.; Demeester, J.; De Smedt, S. C.; Braeckmans, K., The cytotoxic effects of polymer-coated quantum dots and restrictions for live cell applications. *Biomaterials* 2012, 33, 4882-4888.
42. Soenen, S. J.; Manshian, B.; Montenegro, J. M.; Amin, F.; Meermann, B.; Thiron, T.; Cornelissen, M.; Vanhaecke, F.; Doak, S.; Parak, W. J.; Smedt, S. D.; Braeckmans, K., Cytotoxic Effects of Gold Nanoparticles: A Multiparametric Study. *ACS Nano* 2012, 6, 5767-5783.
43. Cui, W.; Li, J.; Zhang, Y.; Rong, H.; Lu, W.; Jiang, L., Effects of aggregation and the surface properties of gold nanoparticles on cytotoxicity and cell growth. *Nanomedicine: Nanotechnology, Biology and Medicine* 2012, 8, 46-53.
44. Nel, A.; Xia, T.; Madler, L.; Li, N., Toxic potential of materials at the nanolevel. *Science* 2006, 311, 622-7.
45. Sanvicens, N.; Marco, M. P., Multifunctional nanoparticles--properties and prospects for their use in human medicine. *Trends Biotechnol* 2008, 26, 425-33.
46. Orrenius, S.; Zhivotovsky, B.; Nicotera, P., Regulation of cell death: the calcium-apoptosis link. *Nat Rev Mol Cell Biol* 2003, 4, 552-65.

47. Choi, S. Y.; Jeong, S.; Jang, S. H.; Park, J.; Park, J. H.; Ock, K. S.; Lee, S. Y.; Joo, S. W., In vitro toxicity of serum protein-adsorbed citrate-reduced gold nanoparticles in human lung adenocarcinoma cells. *Toxicol In Vitro* 2012, 26, 229-37.
48. Bulseco, D. A.; Wolf, D. E., Fluorescence Correlation Spectroscopy: Molecular Complexing in Solution and in Living Cells. In *Methods in Cell Biology*, Greenfield, S.; David, E. W., Eds. Academic Press: 2007; Vol. Volume 81, pp 525-559.
49. Lakowicz, J. R., *Principles of Fluorescence Spectroscopy*. Third ed.; Springer Science & Business Media LLC: 2006.
50. Einstein, A., Eine neue Bestimmung der Moleküldimensionen. *Annalen der Physik* 1906, 324, 289-306.
51. Kim, S. A.; Schwille, P., Intracellular applications of fluorescence correlation spectroscopy: prospects for neuroscience. *Curr Opin Neurobiol* 2003, 13, 583-90.
52. Magde, D.; Webb, W. W.; Elson, E., THERMODYNAMIC FLUCTUATIONS IN A REACTING SYSTEM - MEASUREMENT BY FLUORESCENCE CORRELATION SPECTROSCOPY. *Phys. Rev. Lett.* 1972, 29, 705-&.
53. Sharma, S.; Pal, N.; Chowdhury, P. K.; Sen, S.; Ganguli, A. K., Understanding Growth Kinetics of Nanorods in Microemulsion: A Combined Fluorescence Correlation Spectroscopy, Dynamic Light Scattering, and Electron Microscopy Study. *Journal of the American Chemical Society* 2012, 134, 19677-19684.
54. Dominguez-Medina, S.; McDonough, S.; Swanglap, P.; Landes, C. F.; Link, S., In Situ Measurement of Bovine Serum Albumin Interaction with Gold Nanospheres. *Langmuir* 2012, 28, 9131-9139.
55. Widengren, J.; Mets, U.; Rigler, R., Fluorescence correlation spectroscopy of triplet states in solution: a theoretical and experimental study. *The Journal of Physical Chemistry* 1995, 99, 13368-13379.
56. Hegerfeldt, G. C.; Seidel, D., Blinking molecules: Determination of photophysical parameters from the intensity correlation function. *The Journal of Chemical Physics* 2003, 118, 7741-7746.
57. Elson, E. L.; Magde, D., Fluorescence correlation spectroscopy. I. Conceptual basis and theory. *Biopolymers* 1974, 13, 1-27.
58. Orrenius, S.; Nicotera, P.; Zhivotovsky, B., Cell Death Mechanisms and Their Implications in Toxicology. *Toxicological Sciences* 2011, 119, 3-19.
59. Lakowicz, J. R., Radiative decay engineering: biophysical and biomedical applications. *Analytical Biochemistry* 2001, 298, 1-24.
60. Geddes, C. D.; Aslan, K.; Gryczynski, I.; Lakowicz, J. R., Metal-enhanced fluorescence sensing. In *Fluorescence Sensors and Biosensors*, CRC Press: 2006; pp 121-181.
61. Brouard, D.; Viger, M. L.; Bracamonte, A. G.; Boudreau, D., Label-free biosensing based on multilayer fluorescent nanocomposites and a cationic polymeric transducer. *ACS Nano* 2011, 5, 1888-1896.
62. He, R.-Y.; Su, Y.-D.; Cho, K.-C.; Lin, C.-Y.; Chang, N.-S.; Chang, C.-H.; Chen, S.-J., Surface plasmon-enhanced two-photon fluorescence microscopy for live cell membrane imaging. *Optics Express* 2009, 17, 5987-5997.

63. Aouani, H.; Hostein, R.; Mahboub, O.; Devaux, E.; Rigneault, H.; Ebbesen, T. W.; Wenger, J., Saturated excitation of fluorescence to quantify excitation enhancement in aperture antennas. *Optics Express* 2012, 20, 18085-18090.
64. Asselin, J.; Viger, M. L.; Boudreau, D., Metal-Enhanced Fluorescence and FRET in Multilayer Core-Shell Nanoparticles. *Advances in Chemistry* 2014, 2014, 1-16.
65. Ray, K.; Zhang, J. A.; Lakowicz, J. R., Fluorophore Conjugated Silver Nanoparticles: A Time-resolved Fluorescence Correlation Spectroscopic Study. *Single Molecule Spectroscopy and Imaging II* 2009, 7185.
66. Tang, L.; Dong, C.; Ren, J., Highly sensitive homogenous immunoassay of cancer biomarker using silver nanoparticles enhanced fluorescence correlation spectroscopy. *Talanta* 2010, 81, 1560-1567.
67. Oleg, K.; Grégoire, B., Fluorescence correlation spectroscopy: the technique and its applications. *Reports on Progress in Physics* 2002, 65, 251.
68. Lakowicz, J. R., Principles of Fluorescence Spectroscopy. 3rd ed.; Springer Science & Business Media: USA, 2006.
69. Widengren, J.; Mets, Ü., Conceptual basis of fluorescence correlation spectroscopy and related techniques as tools in bioscience. *Single Molecule Detection in Solution: Methods and Applications* 2002, 69-120.
70. Widengren, J.; Mets, Ü.; Rigler, R., Photodynamic properties of green fluorescent proteins investigated by fluorescence correlation spectroscopy. *Chemical Physics* 1999, 250, 171-186.
71. Lozzio, C. B.; Lozzio, B. B., Human chronic myelogenous leukemia cell-line with positive Philadelphia chromosome. *Blood* 1975, 45, 321-34.
72. Borst, P.; Evers, R.; Kool, M.; Wijnholds, J., A family of drug transporters: the multidrug resistance-associated proteins. *J Natl Cancer Inst* 2000, 92, 1295-302.
73. Ramakrishnan, P., The role of P-glycoprotein in the blood-brain barrier. *Einstein Quart. J. Biol. Med* 2003, 19, 160-165.
74. Borst, P.; Evers, R.; Kool, M.; Wijnholds, J., The multidrug resistance protein family. *Biochim Biophys Acta* 1999, 6, 347-57.
75. Fardel, O.; Lecreur, V.; Guillouzo, A., The P-glycoprotein multidrug transporter. *Gen Pharmacol* 1996, 27, 1283-91.
76. Syvitski, J. P. M., *Principles, Methods and Application of Particle Size Analysis*. Cambridge University Press New York: United States of America, 2007.
77. Bhattacharyya, S.; Prashanthi, S.; Bangal, P. R.; Patra, A., Photophysics and Dynamics of Dye-Doped Conjugated Polymer Nanoparticles by Time-Resolved and Fluorescence Correlation Spectroscopy. *The Journal of Physical Chemistry C* 2013, 117, 26750-26759.
78. Zhao, J. J.; Bae, S. C.; Xie, F.; Granick, S., Diffusion of polymer-coated nanoparticles studied by fluorescence correlation spectroscopy. *Macromolecules* 2001, 34, 3123-3126.
79. Zhang, B.; Lan, T.; Huang, X.; Dong, C.; Ren, J., Optical Trapping Effect and Its Calibration Method in Resonance Light Scattering Correlation Spectroscopy of Gold Nanoparticles in Solution. *The Journal of Physical Chemistry C* 2014, 118, 14495-14501.

80. Xu, Z.; Huang, X.; Dong, C.; Ren, J., Fluorescence correlation spectroscopy of gold nanoparticles, and its application to an aptamer-based homogeneous thrombin assay. *Microchim Acta* 2014, 181, 723-730.
81. Boca, S. C.; Farcau, C.; Astilean, S., The study of Raman enhancement efficiency as function of nanoparticle size and shape. *Nuclear Instruments and Methods in Physics Research Section B: Beam Interactions with Materials and Atoms* 2009, 267, 406-410.
82. Boca, S.; Rugina, D.; Pinteau, A.; Barbu-Tudoran, L.; Astilean, S., Flower-shaped gold nanoparticles: synthesis, characterization and their application as SERS-active tags inside living cells. *Nanotechnology* 2011, 22, 0957-4484.
83. Rigler, P.; Meier, W., Encapsulation of fluorescent molecules by functionalized polymeric nanocontainers: Investigation by confocal fluorescence Imaging and fluorescence correlation Spectroscopy. *Journal of the American Chemical Society* 2006, 128, 367-373.
84. Mulvaney, P., Surface Plasmon Spectroscopy of Nanosized Metal Particles. *Langmuir* 1996, 12, 788-800.
85. Liz-Marzán, L. M.; Giersig, M.; Mulvaney, P., Synthesis of Nanosized Gold-Silica Core-Shell Particles. *Langmuir* 1996, 12, 4329-4335.
86. Liu, W.; Zhu, Z.; Deng, K.; Li, Z.; Zhou, Y.; Qiu, H.; Gao, Y.; Che, S.; Tang, Z., Gold Nanorod@Chiral Mesoporous Silica Core-shell Nanoparticles with Unique Optical Properties. *Journal of the American Chemical Society* 2013, 135, 9659-9664.
87. Bharadwaj, P.; Anger, P.; Novotny, L., Nanoplasmonic enhancement of single-molecule fluorescence. *Nanotechnology* 2007, 18, 044017.
88. Kuhn, H., Classical aspects of energy transfer in molecular systems. *J. Chem. Phys.* 1970, 53, 101-108.
89. Roy, S.; Dixit, C. K.; Woolley, R.; O'Kennedy, R.; McDonagh, C., Synthesis and characterization of model silica-gold core-shell nanohybrid systems to demonstrate plasmonic enhancement of fluorescence. *Nanotechnology* 2012, 23.
90. Martini, M.; Perriat, P.; Montagna, M.; Pansu, R.; Julien, C.; Tillement, O.; Roux, S., How Gold Particles Suppress Concentration Quenching of Fluorophores Encapsulated in Silica Beads. *J. Phys. Chem. C* 2009, 113, 17669-17677.
91. Reineck, P.; Gomez, D.; Ng, S. H.; Karg, M.; Bell, T.; Mulvaney, P.; Bach, U., Distance and Wavelength Dependent Quenching of Molecular Fluorescence by Au@SiO₂ Core-Shell Nanoparticles. *ACS Nano* 2013, 7, 6636-6648.
92. Schneider, G.; Decher, G.; Nerambourg, N.; Praho, R.; Werts, M. H. V.; Blanchard-Desce, M., Distance-dependent fluorescence quenching on gold nanoparticles ensheathed with layer-by-layer assembled polyelectrolytes. *Nano Lett.* 2006, 6, 530-536.
93. Roy, S.; Woolley, R.; MacCraith, B. D.; McDonagh, C., Fluorescence Lifetime Analysis and Fluorescence Correlation Spectroscopy Elucidate the Internal Architecture of Fluorescent Silica Nanoparticles. *Langmuir* 2010, 26, 13741-13746.
94. Murray, R. A.; Qiu, Y.; Chiodo, F.; Marradi, M.; Penades, S.; Moya, S. E., A Quantitative Study of the Intracellular Dynamics of Fluorescently Labelled Glyco-Gold Nanoparticles via Fluorescence Correlation Spectroscopy. *Small* 2014, 10, 2602-2610.
95. Doose, S.; Tsay, J. M.; Pinaud, F.; Weiss, S., Comparison of photophysical and colloidal properties of biocompatible semiconductor nanocrystals using fluorescence correlation spectroscopy. *Anal. Chem.* 2005, 77, 2235-2242.

96. Khatua, S.; Paulo, P. M. R.; Yuan, H. F.; Gupta, A.; Zijlstra, P.; Orrit, M., Resonant Plasmonic Enhancement of Single-Molecule Fluorescence by Individual Gold Nanorods. *ACS Nano* 2014, 8, 4440-4449.
97. Berlier, J. E.; Rothe, A.; Buller, G.; Bradford, J.; Gray, D. R.; Filanoski, B. J.; Telford, W. G.; Yue, S.; Liu, J. X.; Cheung, C. Y.; Chang, W.; Hirsch, J. D.; Beechem, J. M.; Haugland, R. P., Quantitative comparison of long-wavelength Alexa Fluor dyes to Cy dyes: Fluorescence of the dyes and their bioconjugates. *J. Histochem. Cytochem.* 2003, 51, 1699-1712.
98. Waddell, T. G.; Leyden, D. E.; Debello, M. T., THE NATURE OF ORGANOSILANE TO SILICA-SURFACE BONDING. *J. Am. Chem. Soc.* 1981, 103, 5303-5307.
99. Liz-Marzan, L. M.; Giersig, M.; Mulvaney, P., Synthesis of nanosized gold-silica core-shell particles. *Langmuir* 1996, 12, 4329-4335.
100. Zander, C.; Enderlein, J.; Keller, R. A., Single-Molecule Detection in Solution. In *Methods and Applications*, VCH-Wiley: Berlin/New York, 2002.
101. Haustein, E.; Schwille, P., Fluorescence correlation spectroscopy: Novel variations of an established technique. *Annu. Rev. Biophys. Biomol. Struct.* 2007, 36, 151-169.
102. Bhattacharyya, S.; Prashanthi, S.; Bangal, P. R.; Patra, A., Photophysics and Dynamics of Dye-Doped Conjugated Polymer Nanoparticles by Time-Resolved and Fluorescence Correlation Spectroscopy. *J. Phys. Chem. C* 2013, 117, 26750-26759.
103. Balaji, P. S.; Murthy, A. V. R.; Tiwari, N.; Kulkarni, S., Fluorescence Correlation Spectroscopy of Gold Nanoparticles. *Spectroscopy Letters* 2012, 45, 22-28.
104. Weiss, M.; Elsner, M.; Kartberg, F.; Nilsson, T., Anomalous Subdiffusion Is a Measure for Cytoplasmic Crowding in Living Cells. *Biophysical Journal* 2004, 87, 3518-3524.
105. Arrio-Dupont, M.; Foucault, G.; Vacher, M.; Devaux, P. F.; Cribier, S., Translational diffusion of globular proteins in the cytoplasm of cultured muscle cells. *Biophys J* 2000, 78, 901-7.
106. Arvizo, R. R.; Moyano, D. F.; Saha, S.; Thompson, M. A.; Bhattacharya, R.; Rotello, V. M.; Prakash, Y. S.; Mukherjee, P., Probing novel roles of the mitochondrial uniporter in ovarian cancer cells using nanoparticles. *J Biol Chem* 2013, 288, 17610-8.
107. Lewis, W.; Day, B. J.; Copeland, W. C., Mitochondrial toxicity of NRTI antiviral drugs: an integrated cellular perspective. *Nat Rev Drug Discov* 2003, 2, 812-22.
108. Sukhorukov, V. M.; Bereiter-Hahn, J., Anomalous Diffusion Induced by Cristae Geometry in the Inner Mitochondrial Membrane. *PLoS ONE* 2009, 4, e4604.
109. Bereiterhahn, J.; Voth, M., DYNAMICS OF MITOCHONDRIA IN LIVING CELLS - SHAPE CHANGES, DISLOCATIONS, FUSION, AND FISSION OF MITOCHONDRIA. *Microsc. Res. Tech.* 1994, 27, 198-219.
110. Nomura, Y., Evaluation of Mitochondrial DNA Dynamics Using Fluorescence Correlation Analysis. In *Current Frontiers and Perspectives in Cell Biology*, InTech: 2012; pp 525-535.
111. Hüttemann, M.; Helling, S.; Sanderson, T. H.; Sinkler, C.; Samavati, L.; Mahapatra, G.; Varughese, A.; Lu, G.; Liu, J.; Ramzan, R.; Vogt, S.; Grossman, L. I.; Doan, J. W.; Marcus, K.; Lee, I., Regulation of mitochondrial respiration and apoptosis through cell signaling: Cytochrome c oxidase and cytochrome c in ischemia/reperfusion injury and inflammation. *Biochimica et Biophysica Acta (BBA) - Bioenergetics* 2012, 1817, 598-609.

112. Ly, J. D.; Grubb, D. R.; Lawen, A., The mitochondrial membrane potential ($\Delta\psi_m$) in apoptosis; an update. *Apoptosis* 2003, 8, 115-128.

Study of Toxicity of Nanoparticles in Biological Media

Abstract: Gold nanoparticles (GNPs) are of great interest for several applications in nanomedicine; especially in imaging and sensing, drug delivery or photothermal therapy because of their unique physical and chemical properties. For all these applications, a better understanding of the interaction of GNPs with biomolecules and their uptake into cells is of great importance. Thus the main objective of this thesis was to study the toxicity of GNPs in biological media based on their sizes, shapes and surface chemistries. Cytotoxicity studies on human cells were done *in vitro* in presence of six GNP samples having spherical and flower shapes. We compared the cytotoxic effects and showed that it was largely higher for flower-shaped GNPs than spherical ones. Further we built-up the optical assembly and the set-up of the Fluorescence Correlation Spectroscopy (FCS). Followed by the set-up, the sensitivity, the resolution and other parameters were determined during the characterization of the FCS system. Then FCS was used to characterize fluorescent molecule-conjugated GNP, which were fabricated in the interest of biomedical applications. In the next step, we characterized the diffusion behavior of MitoTracker dye labeled mitochondria by FCS in order to be able to compare in future the mitochondrial diffusion after incubating with GNPs, which is described as the perspectives.

Étude de la toxicité des nanoparticules dans les milieux biologiques

Résumé: Les nanoparticules d'or (NPO) sont d'un grand intérêt pour de nombreuses applications en nanomédecine (en particulier pour l'imagerie, la détection de pathologies, la délivrance de médicaments ou la thérapie photothermique) en raison de leurs propriétés physiques et chimiques. Pour toutes ces applications, une meilleure compréhension de l'interaction des NPO avec les biomolécules et de leur absorption dans les cellules est d'une importance primordiale. Ainsi, l'objectif principal de cette thèse était d'étudier la toxicité des NPO dans les milieux biologiques en fonction de leurs tailles, leurs formes et leurs chimies de surface. Des études de cytotoxicité sur des cellules humaines ont été réalisées *in vitro*, en présence de six types différents de NPO de forme sphérique et de nano-fleur. Nous avons comparé les effets cytotoxiques et montré qu'ils étaient largement supérieurs pour les NPO en forme de nanofleur par rapport aux NPO sphériques. En outre, nous avons mis en place un système de corrélation de spectroscopie de fluorescence (CSF). La sensibilité, la résolution et les principaux paramètres du système ont été déterminés lors de sa caractérisation. La CSF a ensuite été utilisée pour caractériser des NPO fluorescentes fabriquées pour des applications biomédicales. Nous avons également caractérisé la diffusion de Mitotracker, un marqueur des mitochondries par CSF afin d'être en mesure de comparer la diffusion mitochondriale après incubation de NPO.

Discipline: Physique mention Génie Biologique et Médical

Mots clés: cytotoxicité, nanoparticules, *in vitro*, nanoparticules d'or, spectroscopie de corrélation de fluorescence, bio-imagerie, chimie de surface, cytosquelette de la cellule

Intitulé et adresse des laboratoires: CSPBAT (Chimie, Structures et Propriétés de Biomatériaux et d'Agents Thérapeutiques), UFR SMBH, 74 rue Marcel Cachin, 93017 Bobigny.